A Computational Framework for Long-Term Atomistic Analysis of Solute Diffusion in Nanomaterials

Xingsheng Sun

Dissertation submitted to the Faculty of the

Virginia Polytechnic Institute and State University

in partial fulfillment of the requirements for the degree of

Doctor of Philosophy

in

Aerospace Engineering

Kevin G. Wang, Chair

Pilar Ariza

Rakesh K. Kapania

Gary D. Seidel

September 05, 2018

Blacksburg, Virginia

Keywords: Diffusive Molecular Dynamics, Long-term process, Atomic resolution, Palladium nanoparticles, Hydrogen absorption, Phase transformation, Stacking faults

A Computational Framework for Long-Term Atomistic Analysis of Solute Diffusion in Nanomaterials

Xingsheng Sun

ABSTRACT

Diffusive Molecular Dynamics (DMD) is a class of recently developed computational methods for the simulation of long-term mass transport with a full atomic fidelity. Its basic idea is to couple a discrete kinetic model for the evolution of mass transport process with a non-equilibrium thermodynamics model that governs lattice deformation and supplies the requisite driving forces for kinetics. Compared to previous atomistic models, e.g., accelerated Molecular Dynamics and on-the-fly kinetic Monte Carlo, DMD allows the use of larger time-step sizes and hence has a larger simulation time window for mass transport problems. This dissertation focuses on the development, assessment and application of a DMD computational framework for the long-term, three-dimensional, deformation-diffusion coupled analysis of solute mass transport in nanomaterials. First, a computational framework is presented, which consists mainly of: (1) a computational model for interstitial solute diffusion, which couples a nonlinear optimization problem with a first-order nonlinear ordinary differential equation; (2) two numerical methods, i.e., mean field approximation and subcycling time

integration, for accelerating DMD simulations; and (3) a high-performance computational solver, which is parallelized based on Message Passing Interface (MPI) and the PETSc/TAO library for large-scale simulations. Next, the computational framework is validated and assessed in two groups of numerical experiments that simulate hydrogen mass transport in palladium. Specifically, the framework is validated against a classical lattice random walk model. Its capability to capture the atomic details in nanomaterials over a long diffusive time scale is also demonstrated. In these experiments, the effects of the proposed numerical methods on solution accuracy and computation time are assessed quantitatively. Finally, the computational framework is employed to investigate the long-term hydrogen absorption into palladium nanoparticles with different sizes and shapes. Several significant findings are shown, including the propagation of an atomistically sharp phase boundary, the dynamics of solute-induced lattice deformation and stacking faults, and the effect of lattice crystallinity on absorption rate. Specifically, the two-way interaction between phase boundary propagation and stacking fault dynamics is noteworthy. The effects of particle size and shape on both hydrogen absorption and lattice deformation are also discussed in detail.

A Computational Framework for Long-Term Atomistic Analysis of Solute Diffusion in Nanomaterials

Xingsheng Sun

GENERAL AUDIENCE ABSTRACT

Interstitial diffusion in crystalline solids describes a phenomenon in which the solute constituents (e.g., atoms) move from an interstitial space of the host lattice to a neighboring one that is empty. It is a dominating feature in many important engineering applications, such as metal hydrides, lithium-ion batteries and hydrogen-induced material failures. These applications involve some key problems that might take place over long time periods (e.g., longer than 1 s), while the nanoscale behaviors and mechanisms become significant. The time scale of these problems is beyond the capability of established atomistic models, e.g., accelerated Molecular Dynamics and on-the-fly kinetic Monte Carlo. To this end, this dissertation presents the development and application of a new computational framework, referred to as Diffusive Molecular Dynamics (DMD), for the simulation of long-term interstitial solute diffusion in advanced nanomaterials. The framework includes three key components. Firstly, a DMD computational model is proposed, which accounts for three-dimensional, deformation-diffusion coupled analysis of interstitial solute mass transport. Secondly, nu-

merical methods are employed to accelerate the DMD simulations while maintaining a high solution accuracy. Thirdly, a high-performance computational solver is developed to implement the DMD model and the numerical methods. Moreover, regarding its application, the DMD framework is first validated and assessed in the numerical experiments pertaining to hydrogen mass transport in palladium crystals. Then, it is employed to investigate the atomic behaviors and mechanisms involved in the long-term hydrogen absorption by palladium nanoparticles with different sizes and shapes. The two-way interaction between hydrogen absorption and lattice deformation is studied in detail.

Acknowledgments

I would like to express my sincere gratitude to my advisor Dr. Kevin Wang, for accepting me into your research group and treating me as a family member through my Ph.D. studies. You have shown me the most important characteristics that a qualified scholar should have: integrity, passion, tenacity, collaboration, communication, etc. Your encouragement, support and guidance have inspired me during all the time of my scientific research.

I would like to give my heartfelt thanks to my collaborators, Dr. Pilar Ariza and Dr. Michael Ortiz. Thanks for providing me with valuable comments and guidance, especially on the application of the computational framework. I still remember the weekly meetings that we had in Fall 2017. It was a wonderful experience to discuss the simulation results with you.

I would like to thank the other members of my dissertation committee, Dr. Rakesh Kapania and Dr. Gary Seidel, for reviewing this dissertation and giving me professional and helpful suggestions.

I am profoundly grateful to my labmates and friends, Mr. Shunxiang Cao, Dr. Jianxun

Wang, Mr. Guangyao Wang, Mr. Yang Song, Mr. Howard Chung, Dr. Jinlong Wu, Dr. Rui Sun, Mr. Colin Glesner, Dr. Petr Cagas, Mr. Robert Masti, Mr. Matthew Roberts, and Mr. Keyu Feng. Thanks for your help and encouragement, especially when I was stuck in the research and daily life. It is also an unforgettable memory to discuss scientific research with you both in the office and while fishing on/by New River.

I am highly indebted to my family, for the unconditional support.

Contents

List of Figures

List of Tables

Chapter 1

Introduction

Diffusion is a phenomenon of the material transport through the motion of atoms or molecules. In crystalline solids, the interstitial diffusion occurs when solute atoms are considerably smaller than host atoms (e.g., hydrogen in palladium, lithium-ion in silicon). The solute atoms migrate from an interstitial site of the host lattice to a neighboring one that is empty. Meanwhile, the host lattice undergoes deformation due to the accommodation of the solute atoms.

The interstitial diffusion of solute atoms in crystalline solids plays a key role in many aerospace and ocean engineering applications. A lot of applications benefit from interstitial diffusion, since the transport of interstitial atoms is able to store, release and convert energy. One example is metal hydrides, a promising way to store hydrogen for some electrically powered vehicles equipped with hydrogen fuel cells, e.g., Boeing Phantom Eye UAV

(unmanned aerial vehicle) [1] and Ifremer IDEF AUV (autonomous underwater vehicle) [2]. The storage of hydrogen in metal hydrides (e.g., MgH_x, $NaAlH_x$) relies on the interstitial diffusion of hydrogen atoms [3, 4, 5]. Similarly, the operation of rechargeable lithium-ion batteries, employed by some planetary rovers such as Mars Curiosity [6], relies on a reversible phase transformation in the anodic and cathodic materials (e.g., Li_xSi, Li_xFePO_4). This process is induced by the interstitial diffusion of lithium ions [7, 8]. For these applications related to energy storage and conversion, there has been a continuous push towards nanostructured systems, as they hold promise to accelerate the charging and discharging process, and increase the energy and power density [7, 9, 10].

At the same time, the interstitial diffusion of solute atoms can also cause large local lattice deformation and hence possibly material failure to the host crystals. Examples include hydrogen embrittlement in steels [11], sensitization effect in aluminium alloys [12], and capacity fading of cathode in lithium-ion batteries [13]. Regarding these problems, understanding the actual nanomechanisms of failure is crucial for material designers, since the answers to mitigating such failure and enhancing the properties of materials (e.g., mechanical, electrical) may be rooted in how solute modifies material behaviors at the nanoscale.

This dissertation focuses on the development of a new computational framework, referred to as Diffusive Molecular Dynamics (DMD), to simulate long-term, interstitial diffusion of solute atoms in advanced nanomaterials, which involves solute-induced phase transformation, local lattice expansion and distortion, and dynamics of stacking faults and dislocations. Due to the long time scale, these problems have not been thoroughly analyzed by the existing atomistic

models, which significantly impedes the advancement of related fields. The remainder of this chapter is organized as follows. Several specific experimental studies, which motivated the work in this dissertation, are described in Section 1.1. Literature reviews on the existing atomistic models and DMD methods are then presented in Sections 1.2 and 1.3, respectively. Finally, the contributions and outline of this dissertation are provided in Section 1.4.

1.1 Motivations

Recent experimental studies have revealed a lot of impressive phenomena that are related to the interstitial diffusion of solute atoms in crystalline solids. In this section, several selected experimental studies are described and their features are summarized.

1.1.1 Hydrogen absorption in palladium nanoparticles

The palladium-hydrogen (Pd-H) system is a prototypical model for studying solute-induced phase transformation, because it allows for relatively fast reaction kinetics at easily accessible temperatures and pressures [14]. The Pd-H system exhibits two distinct phases at room temperature: the α phase at low H concentration (up to $PdH_{0.015}$), and the β phase at high H concentration ($PdH_{0.6}$ and above). Attendant to the α-to-β phase transformation, there is a lattice expansion with approximately 3.5% increase in lattice constant [15] and 10.4% increase in volume, which may result in the formation of misfit dislocations and stacking faults.

Recent experiments have shown significant observations during the hydrogenation process of individual, single-crystal Pd nanoparticles. For example, using scanning transmission electron microscopy, Narayan *et al.* [16] observed the propagation of an atomistically sharp, α/β phase boundary in Pd nanocubes with edge lengths between 20 nm and 43 nm. Notably, the time window of the hydrogenation process is larger than 20 s. They also showed Pd lattice misorientation of 1.5%, caused by the propagation of the phase boundary. In addition, using coherent X-ray diffractive imaging, Ulvestad *et al.* [17] tested Pd nanocubes with edge lengths between 60 nm and 100 nm. They revealed a sharp α-to-β phase transformation and a strain inversion at the corners of the cubes from α to β phase. The time scale of their observations is on the order of minutes. The same research group [18], in 2017, tracked the nucleation and motion of dislocations during the hydriding and dehydriding phase transformation in Pd nanoparticles with sizes of approximately 400 nm. They showed the ability of Pd nanoparticles to "self-heal" crystallographic defects during H loading and unloading processes.

Hydrogen absorption in palladium nanoparticles is a deformation-diffusion coupled problem. It is characterized by the slow motion of a hydride α/β phase boundary and the local lattice deformation due to the misfit of lattice constant between the two phases. The development of a computational framework to simulate this problem is a formidable challenge. It is required not only accounting for the long-term diffusive time scale (usually larger than 1 s) and but also supplying the full atomic details (e.g., local lattice expansion and distortion, crystalline defects).

1.1.2 Lithiation of electrodes in lithium-ion batteries

The lithium-ion (Li-ion) battery is a type of rechargeable batteries in which Li-ions move from the negative electrode (i.e., the anode) to the positive one (i.e., the cathode) and back during discharging and charging processes, respectively. The increasing demand of improving the performance of Li-ion batteries, such as energy density, durability and charging time, has led scholars to focus on understanding the lithiation process of electrodes. Using transmission electron microscopy and electron energy loss spectroscopy, Gu *et al.* [13] revealed the capacity fading mechanism of lithium iron phosphate cathodes, i.e., Li_xFePO_4. They found that, the surface layer of $FePO_4$ nanoparticles gradually lost crystalline structure and became amorphous after 3300 cycles of charging and discharging of Li-ions. As a result, the capacity of the cathodes was reduced by approximately 9%. Moreover, in the lithiation process of crystalline silicon (Si), Chon *et al.* [19] showed the movement of a very sharp crystalline-amorphous phase boundary, with a thickness of the order of 1 nm. The phase boundary advanced into the center of Si specimens starting from their surface, transforming crystalline Si into amorphous Li_xSi. The extension of nanocracks into the crystalline Si was also observed during the lithiation-delithiation cycling.

The effect of Li-ions on the crystallinity of electrodes is quite impressive. Reconstruction of host lattice may be caused by the large volume expansion induced by accommodating Li-ions. For example, attendant to the lithiation of $FePO_4$, the volume increase is approximately 6.6% [20], whereas it can reach 270% during the lithiation of Si [19]. Moreover, the aforementioned Li-ion-induced electrode failure takes place over a long time scale and after a

large number of operating cycles. Therefore, these experimental observations have motivated the development of a computational approach that is capable of simulating long-term mass transport phenomena, while simultaneously retaining fine resolution at the nanoscale.

1.1.3 Hydrogen-induced dislocation motion in iron

Hydrogen (H) always degrades the mechanical properties of metallic materials. Specifically, the materials become brittle and have fracture due to the absorption of H atoms, a phenomenon known as H embrittlement. Extensive research has been conducted in order to understand its mechanisms. One of the mechanisms is H-enhanced localized plasticity [21]. In 1998, Ferreira *et al.* [22] provided a direct experimental evidence for this mechanism. In their experimental study, dislocations were firstly produced by deforming an iron specimen in vacuum. Then the applied load was kept constant. It was found that after H_2 gas was introduced, the motion of dislocations increased. The resolution of their experiments is about 100 nm. More recently, Wang *et al.* [23] tested iron samples under a tensile strain rate of 10^{-4} s^{-1}. They found that the existence of H reduces the effective activation volume and the thermal activation energy for dislocation motion. Also, their observations have a resolution of roughly 100 nm.

The process of H embrittlement involves (i) the transport of H atoms within metallic materials, and (ii) the effect of H atoms on mechanical behaviors of the host materials, especially in the presence of crystallographic defects. This deformation-diffusion coupled process may

occur over a long time in nanosized materials due to a low strain rate of applied loads. Therefore, to investigate the atomic mechanisms of H embrittlement, a computational method must take into account the aforementioned features.

1.1.4 Summary

The experimental observations presented above represent a large class of challenging deformation-diffusion coupled problems, which are characterized by:

- long-term transport of interstitial solute atoms;
- fine resolution at the nanoscale;

and one or more of the following features:

- solute-induced phase transformation;
- solute-induced lattice deformation and reconstruction;
- interaction between solute atoms and preexisting lattice defects.

To the author's best knowledge, currently there is no computational model that simultaneously accounts for all these features.

1.2 Computational methods in atomistic simulations

Due to the significance of describing full atomic details, various atomistic methods have been developed to study the behaviors of materials on dissimilar time scales. In the following subsections, several atomistic methods will be discussed, as well as their applications and limitations in mass transport problems.

1.2.1 Molecular Dynamics

Molecular Dynamics (MD) is a method that tracks true thermal vibrations of a set of interacting atoms. It simulates the time evolution of atoms through directly solving Newton's equations of motion. Given an accurate interatomic potential function, it can calculate the time history of the positions and momenta of the atoms in a system, and the thermodynamic properties of the system, e.g., temperature, can be calculated using the ergodic hypothesis.

MD method constitutes a powerful computational tool as it explicitly models atoms and their interactions. It has a wide range of applications in investigating nanoscale behaviors and mechanisms involved in mass transport problems. For example, Zhou *et al.* calculated mass transport (e.g., diffusion coefficients) [24] and mechanical (e.g., elastic constants) [25] properties in palladium hydrides, which are dependent of both temperature and hydrogen concentration. Ostadhossein *et al.* [26] investigated the atomic mechanisms of lithium-ion insertion into crystalline silicon, using the reactive-force-field-based MD simulations. They revealed that the insertion of lithium-ion into interlayer spacing between two adjacent {111}

layers leads to the peeling-off of the {111} faces and subsequent amorphization. In addition, Song *et al.* [27] predicted an atomic mechanism of hydrogen embrittlement in iron, referred to as hydrogen-induced ductile to brittle transition. They found that hydrogen atoms aggregate at the tip of an existing nanocrack, resulting in the suppression of dislocation emission therein and then permitting brittle-cleavage failure followed by slow growth of the nanocrack.

Although lots of significant phenomena and mechanisms at the nanoscale have been revealed by MD simulations, the key limitation of MD method lies in its short simulation time. The time-step size of MD is limited to the order of femtoseconds by the frequency of atomic vibrations. Therefore, the time window attendant to MD simulations is on the order of nanoseconds (e.g., 2.2 ns in Ref. [25]), which is far away from the diffusion time scale in the experimental observations (usually longer than 1 s). Moreover, in the simulations related to mechanical deformations, MD studies are typically performed under extremely high strain rates (e.g., 10^{10} s^{-1} in Ref. [28]), which ignores important mass transport process and precludes experimental corroboration for simulation predictions.

1.2.2 Accelerated Molecular Dynamics

A variety of techniques have been developed to overcome the time scale limitation of MD method while maintaining full atomic fidelity. For instance, in many physical processes in materials science, the dynamical evolution of a system is characterized by "infrequent-event" transitions. In other words, the residence time of the system in an activated event (i.e., a

state) is much longer than the correlation time[1]. An efficient approach to simulate this type of systems is transition state theory [30] based accelerated MD (AMD), such as parallel replica dynamics (PRD) [31], hyperdynamics [32] and temperature accelerated dynamics (TAD) [33]. AMD methods track the transitions between microscopic states. Their basic idea is to design an MD-based algorithm that leads to more quick discovery of the escape pathway from the current state to another new one. For example, MD simulations are accelerated by simultaneously running many replicas of the system in PRD, adding the potential energy surface by a non-negative bias potential in hyperdynamics, and raising the temperature of the system in TAD.

Regarding the applications, Duan *et al.* [34] employed PRD to examine lithium-ion transport through a polymer matrix. They estimated the free energy of the lithium-ion, which is dependent of its position. The time scale of their simulations is up to around 100 ns. Using hyperdynamics, Voter *et al.* [35] simulated the diffusive motion of a nickel adatom on a small nickel {100} terrace at 500 K. They are able to reach a simulation time of 20 μs. Moreover, Cogoni *et al.* [36] adopted TAD to simulate the diffusion of small self-interstitial clusters with different structures in silicon. Their simulations span up to the time scale of microseconds.

Clearly, AMD methods have made great strides in extending the time scale of conventional MD simulations. However, AMD simulations might slow down in the cases of large systems, high temperature, or low energy barrier between states. Specifically, for mass transport

[1]The correlation time of a system is defined as the duration of the system memory [29]. If the system has resided in a state for longer than the correlation time, the probability for escaping the state is independent of how the system enters the state.

problems, the total time window accessible to these methods is limited by the frequency of individual atom/vacancy hops within the material sample and is typically less than 1 s for large-scale simulations.

1.2.3 Kinetic Monte Carlo

Kinetic Monte Carlo (KMC) [37, 38, 39] is another powerful method that is capable of extending the time scale of MD simulations. Traditional KMC employs a catalog of all possible transition pathways and associated rate constants for any given state of the system. A random number can be generated to choose one of the pathways and evolve the system from the current state to a new one. This computational process is repeated, until the system reaches the final state. Obviously, traditional KMC suffers from two major limitations: a complete catalog of all possible transition pathways and a slow process of calculating the rate list. For a complex system, it is difficult or even impossible to know all the transitions in advance.

To overcome these limitations, on-the-fly KMC methods have been developed. Their basic idea is to combine traditional KMC with a technique that is able to search saddle points on the potential energy surface and hence minimum energy paths, in order to build a specific catalog of transition rates on the fly. For example, Henkelman *et al.* [40] combined traditional KMC with the dimer method [41]. They simulated ripening of aluminium adatoms on an aluminium {100} surface at 300 K. The system consists of 20 adatoms and 50 atoms on the

surface and their simulation time can reach 1 ms. In addition, Ramasubramaniam *et al.* [42] presented an on-the-fly KMC method, by combining traditional KMC with the climbing image nudged elastic band method [43]. They studied hydrogen diffusion in body-centered cubic iron and calculated hydrogen diffusivities for temperatures ranging from 300 K to 600 K. Their simulation includes 50 hydrogen atoms and the time window is up to 0.5 ms.

On-the-fly KMC methods have some advantages over traditional dynamics. It is relatively fast and accurate when the rate catalog is complete. However, searching for all possible saddle points might be very slow, especially for a large-scale system. As a result, these methods are limited to systems consisting of hundreds of atoms and the simulation time is much less than 1 s.

1.2.4 Summary

As introduced in Section 1.1, the physical processes of solute transport in crystalline solids at the nanoscale can pertain to the time scale on the order of seconds or even longer. The time scale of these processes is beyond the capability of the aforementioned atomistic methods. To this end, a new computational approach needs to be developed to investigate the atomic behaviors and mechanisms involved in these long-term processes.

1.3 Diffusive Molecular Dynamics

Diffusive Molecular Dynamics (DMD) is a relatively new class of methods that has demonstrated potential for simulating diffusion processes in crystalline solids, with a time scale beyond seconds while maintaining the atomic resolution. Its defining idea is to couple a probabilistic description of the displacive atomic movements (i.e., an optimization problem), with a calibrated empirical kinetic model for the evolution of lattice site occupancy. The basic assumption underlying DMD is that the time scale of diffusion is much larger than that of microscopic state transitions. Therefore, at an intermediate time scale, the microscopic state variables can be considered as random variables. In comparison to the established atomistic models discussed in the previous section, DMD has a larger simulation time window as it does not explicitly resolve thermal vibrations nor individual microscopic state transitions.

The general idea of DMD can be traced back to the variational Gaussian method proposed by LeSar *et al.* [44], and the generalized TDDFT (time-dependent density functional theory) method proposed by Perez and Lewis [45]. The term Diffusive Molecular Dynamics was introduced by Li *et al.* in Ref. [46], who extended DMD to handle diffusive mass transport by vacancy exchange and applied it to study nanoindentation and sintering processes [46] and dislocation reaction mechanisms [47]. Following Li *et al.*, Dontsova *et al.* investigated solute-defect interactions [48] and solute segregation kinetics and dislocation depinning [49]. Moreover, Venturini *et al.* [50] developed a general DMD model for long-term mass transport processes, including a validation of hydrogen desorption in palladium nanofilms, and Wang

et al. [51] showed that the DMD model is capable of capturing the separation of α and β phases in palladium hydrides. More recently, Simpson *et al.* provided a recent theoretical review of DMD [52] and formulated a spin-diffusion stochastic process to interpret the DMD model [53]. In addition, DMD methods have also been used to investigate the dynamic behaviors of nanovoids under tensile stress in different metals [54, 55, 56, 57].

As introduced above, a lot of efforts have been made to complete the DMD theory and expand its application scope. However, previous DMD methods have two major limitations. Firstly, currently there is no DMD model for the three-dimensional, deformation-diffusion coupled analysis of interstitial diffusion. Most of previous DMD work has focused on either pure metals (e.g., copper [46, 47, 54, 55, 57], aluminium [57], magnesium [56]) or substitutional binary alloys (e.g., aluminium-magnesium [48, 49], nickel-palladium [50]). For the problems of interstitial mass transport which have a different diffusion mechanism, previous DMD work only includes a one-dimensional analysis of hydrogen diffusion within thin palladium films [50, 51], and the hydrogen-induced lattice deformation was neglected. Secondly, the time-wise acceleration of DMD methods takes place at some computational expense, since the computational cost of DMD methods, which is dominated by the nonlinear optimization problem, can be significant. In order to reduce the computational cost, previous DMD work [46, 47, 48, 49, 52] employs the point estimate to calculate the microscopic average of many-body interatomic potential. However, this estimate may introduce relatively large errors in the solution for the simulation of interstitial diffusion, e.g., in the problem that involves the propagation of a sharp hydride phase boundary [58].

1.4 Dissertation contributions and outline

1.4.1 Dissertation contributions

The major contributions of this dissertation are summarized as follows:

- Development of a DMD computational framework for solving long-term, three-dimensional, deformation-diffusion coupled problems of interstitial solute mass transport in advanced nanomaterials. Key components of this framework include:

  (a) a computational model for the interstitial diffusion of solute atoms, which couples a nonlinear optimization problem for the deformation process, with a first-order nonlinear ordinary differential equation for the diffusion process;

  (b) two numerical methods, i.e., mean field approximation and subcycling time integration, for accelerating DMD simulations while maintaining a high computational accuracy;

  (c) a high-performance computational solver, which has been parallelized based on Message Passing Interface (MPI) and the PETSc/TAO library [59] for large-scale simulations.

- Assessment of the developed computational framework in numerical experiments with respect to palladium-hydrogen (Pd-H) systems. First, the framework is validated against a classical lattice random walk model. Then, the capability of the framework to capture the atomic details in nanomaterials (size $\sim$ 16 nm) over a diffusive

time window (time $>$ 30 s) is shown. Moreover, in the numerical experiments, the effects of the proposed numerical methods on solution accuracy and computation time are assessed quantitatively.

- Application of the developed computational framework to investigate the long-term H absorption into Pd nanoparticles with different sizes and shapes. These deformation-diffusion coupled problems involve the propagation of an atomistically sharp phase boundary, the dynamics of solute-induced lattice deformation and stacking faults, and the effect of lattice crystallinity on absorption rate. Specifically, the two-way interaction between the phase boundary propagation and the stacking fault dynamics is noteworthy. The effects of particle size and shape on both H absorption and lattice deformation processes are also discussed in detail.

1.4.2 Outline

This document is organized in the "multi-paper" format. Each of the main chapters is in the format of a peer-reviewed article. Chapter 2 presents the development of the DMD framework. The ability of the framework is demonstrated and its performance is assessed. In Chapter 3, the framework is employed to simulate H absorption into Pd nanocubes with edge lengths ranging from 4 nm to 16 nm. The effects of particle size on equilibrium and kinetic properties of the absorption process are studied. Chapter 4 presents the application of the framework to characterize H absorption in Pd nanoparticles of spherical, octahedral

and cubic shapes with the same volume of approximately $3,800$ nm^3. The effects of particle shape on H absorption and the induced lattice deformation are investigated in detail. Finally, a summary of conclusions and future work is consigned to Chapter 5.

Bibliography

[1] Webpage for Boeing Phantom Eye, `http://www.boeing.com/defense/phantom-eye/`.

[2] Webpage for Ifremer IDEF, `https://wwz.ifremer.fr/cmsm_eng/Systems/AUVs`.

[3] B. Sakintuna, F. Lamari-Darkrim, M. Hirscher, Metal hydride materials for solid hydrogen storage: a review, International Journal of Hydrogen Energy 32 (9) (2007) 1121–1140.

[4] D. Mori, K. Hirose, Recent challenges of hydrogen storage technologies for fuel cell vehicles, International Journal of Hydrogen Energy 34 (10) (2009) 4569–4574.

[5] M. Łukaszewski, K. Hubkowska, A. Czerwiński, Comparative study on the influence of temperature, electrode potential and alloy bulk composition on hydrogen electrosorption into pd–pt and pd–au alloys, Journal of Electroanalytical Chemistry 651 (2) (2011) 131–142.

[6] Webpage for Mars Curiosity Rover, `https://mars.nasa.gov/msl/`.

[7] D. A. Cogswell, M. Z. Bazant, Theory of coherent nucleation in phase-separating nanoparticles, Nano Letters 13 (7) (2013) 3036–3041.

[8] S. Huang, F. Fan, J. Li, S. Zhang, T. Zhu, Stress generation during lithiation of high-capacity electrode particles in lithium ion batteries, Acta Materialia 61 (12) (2013) 4354–4364.

[9] C. Lebouin, Y. Soldo, S. Grigoriev, M. Guymont, P. Millet, Kinetics of hydrogen sorption by palladium nanoparticles, International Journal of Hydrogen Energy 38 (2) (2013) 966–972.

[10] W. Vogel, W. He, Q.-H. Huang, Z. Zou, X.-G. Zhang, H. Yang, Palladium nanoparticles breathe hydrogen; a surgical view with x-ray diffraction, International Journal of Hydrogen Energy 35 (16) (2010) 8609–8620.

[11] D. Hardie, E. Charles, A. Lopez, Hydrogen embrittlement of high strength pipeline steels, Corrosion Science 48 (12) (2006) 4378–4385.

[12] R. Foley, Localized corrosion of aluminum alloysa review, Corrosion 42 (5) (1986) 277–288.

[13] M. Gu, W. Shi, J. Zheng, P. Yan, J.-g. Zhang, C. Wang, Probing the failure mechanism of nanoscale lifepo4 for li-ion batteries, Applied Physics Letters 106 (20) (2015) 203902.

[14] B. D. Adams, A. Chen, The role of palladium in a hydrogen economy, Materials Today 14 (6) (2011) 282–289.

[15] Y. Sakamoto, K. Yuwasa, K. Hirayama, X-ray investigation of the absorption of hydrogen by several palladium and nickel solid solution alloys, Journal of the Less Common Metals 88 (1) (1982) 115–124.

[16] T. C. Narayan, F. Hayee, A. Baldi, A. L. Koh, R. Sinclair, J. A. Dionne, Direct visualization of hydrogen absorption dynamics in individual palladium nanoparticles, Nature Communications 8 (2017) 14020.

[17] A. Ulvestad, M. Welland, S. Collins, R. Harder, E. Maxey, J. Wingert, A. Singer, S. Hy, P. Mulvaney, P. Zapol, et al., Avalanching strain dynamics during the hydriding phase transformation in individual palladium nanoparticles, Nature Communications 6 (2015) 1–8.

[18] A. Ulvestad, A. Yau, The self-healing of defects induced by the hydriding phase transformation in palladium nanoparticles, Nature Communications 8 (1) (2017) 1376.

[19] M. J. Chon, V. A. Sethuraman, A. McCormick, V. Srinivasan, P. R. Guduru, Real-time measurement of stress and damage evolution during initial lithiation of crystalline silicon, Physical Review Letters 107 (4) (2011) 045503.

[20] N. Meethong, H.-Y. Huang, S. A. Speakman, W. C. Carter, Y.-M. Chiang, Strain accommodation during phase transformations in olivine-based cathodes as a materials selection criterion for high-power rechargeable batteries, Advanced Functional Materials 17 (7) (2007) 1115–1123.

[21] C. Beachem, A new model for hydrogen-assisted cracking (hydrogen embrittlement), Metallurgical and Materials Transactions B 3 (2) (1972) 441–455.

[22] P. Ferreira, I. Robertson, H. Birnbaum, Hydrogen effects on the interaction between dislocations, Acta Materialia 46 (5) (1998) 1749–1757.

[23] S. Wang, N. Hashimoto, Y. Wang, S. Ohnuki, Activation volume and density of mobile dislocations in hydrogen-charged iron, Acta Materialia 61 (13) (2013) 4734–4742.

[24] X. Zhou, T. W. Heo, B. C. Wood, V. Stavila, S. Kang, M. D. Allendorf, Temperature- and concentration-dependent hydrogen diffusivity in palladium from statistically-averaged molecular dynamics simulations, Scripta Materialia 149 (2018) 103–107.

[25] X. Zhou, T. Heo, B. Wood, V. Stavila, S. Kang, M. Allendorf, Molecular dynamics studies of fundamental bulk properties of palladium hydrides for hydrogen storage, Journal of Applied Physics 123 (22) (2018) 225105.

[26] A. Ostadhossein, E. D. Cubuk, G. A. Tritsaris, E. Kaxiras, S. Zhang, A. C. Van Duin, Stress effects on the initial lithiation of crystalline silicon nanowires: reactive molecular dynamics simulations using reaxff, Physical Chemistry Chemical Physics 17 (5) (2015) 3832–3840.

[27] J. Song, W. Curtin, Atomic mechanism and prediction of hydrogen embrittlement in iron, Nature Materials 12 (2) (2013) 145–151.

[28] M. Wen, X.-J. Xu, S. Fukuyama, K. Yokogawa, Embedded-atom-method functions for

the body-centered-cubic iron and hydrogen, Journal of Materials Research 16 (12) (2001) 3496–3502.

[29] A. F. Voter, F. Montalenti, T. C. Germann, Extending the time scale in atomistic simulation of materials, Annual Review of Materials Research 32 (1) (2002) 321–346.

[30] H. Eyring, The activated complex in chemical reactions, The Journal of Chemical Physics 3 (2) (1935) 107–115.

[31] A. F. Voter, Parallel replica method for dynamics of infrequent events, Physical Review B 57 (22) (1998) R13985.

[32] A. F. Voter, Hyperdynamics: Accelerated molecular dynamics of infrequent events, Physical Review Letters 78 (20) (1997) 3908.

[33] M. R. So/rensen, A. F. Voter, Temperature-accelerated dynamics for simulation of infrequent events, The Journal of Chemical Physics 112 (21) (2000) 9599–9606.

[34] Y. Duan, J. Halley, L. Curtiss, P. Redfern, Mechanisms of lithium transport in amorphous polyethylene oxide, The Journal of Chemical Physics 122 (5) (2005) 054702.

[35] A. F. Voter, A method for accelerating the molecular dynamics simulation of infrequent events, The Journal of Chemical Physics 106 (11) (1997) 4665–4677.

[36] M. Cogoni, B. Uberuaga, A. Voter, L. Colombo, Diffusion of small self-interstitial clusters in silicon: temperature-accelerated tight-binding molecular dynamics simulations, Physical Review B 71 (12) (2005) 121203.

[37] A. B. Bortz, M. H. Kalos, J. L. Lebowitz, A new algorithm for monte carlo simulation of ising spin systems, Journal of Computational Physics 17 (1) (1975) 10–18.

[38] D. T. Gillespie, A general method for numerically simulating the stochastic time evolution of coupled chemical reactions, Journal of Computational Physics 22 (4) (1976) 403–434.

[39] K. A. Fichthorn, W. H. Weinberg, Theoretical foundations of dynamical monte carlo simulations, The Journal of Chemical Physics 95 (2) (1991) 1090–1096.

[40] G. Henkelman, H. Jónsson, Long time scale kinetic monte carlo simulations without lattice approximation and predefined event table, The Journal of Chemical Physics 115 (21) (2001) 9657–9666.

[41] G. Henkelman, H. Jónsson, A dimer method for finding saddle points on high dimensional potential surfaces using only first derivatives, The Journal of Chemical Physics 111 (15) (1999) 7010–7022.

[42] A. Ramasubramaniam, M. Itakura, M. Ortiz, E. Carter, Effect of atomic scale plasticity on hydrogen diffusion in iron: Quantum mechanically informed and on-the-fly kinetic monte carlo simulations, Journal of Materials Research 23 (10) (2008) 2757–2773.

[43] G. Henkelman, B. P. Uberuaga, H. Jónsson, A climbing image nudged elastic band method for finding saddle points and minimum energy paths, The Journal of Chemical Physics 113 (22) (2000) 9901–9904.

[44] R. LeSar, R. Najafabadi, D. J. Srolovitz, Finite-temperature defect properties from free-energy minimization, Phys. Rev. Lett. 63 (1989) 624–627.

[45] D. Perez, L. J. Lewis, Multiscale model for microstructure evolution in multiphase materials: Application to the growth of isolated inclusions in presence of elasticity, Physical Review E 74 (3) (2006) 031609.

[46] J. Li, S. Sarkar, W. T. Cox, T. J. Lenosky, E. Bitzek, Y. Wang, Diffusive molecular dynamics and its application to nanoindentation and sintering, Physical Review B 84 (5) (2011) 054103.

[47] S. Sarkar, J. Li, W. T. Cox, E. Bitzek, T. J. Lenosky, Y. Wang, Finding activation pathway of coupled displacive-diffusional defect processes in atomistics: Dislocation climb in fcc copper, Physical Review B 86 (1) (2012) 014115.

[48] E. Dontsova, J. Rottler, C. Sinclair, Solute-defect interactions in al-mg alloys from diffusive variational gaussian calculations, Physical Review B 90 (17) (2014) 174102.

[49] E. Dontsova, J. Rottler, C. Sinclair, Solute segregation kinetics and dislocation depinning in a binary alloy, Physical Review B 91 (22) (2015) 224103.

[50] G. Venturini, K. Wang, I. Romero, M. P. Ariza, M. Ortiz, Atomistic long-term simulation of heat and mass transport, Journal of the Mechanics and Physics of Solids 73 (2014) 242–268.

[51] K. Wang, M. Ortiz, M. P. Ariza, Long-term atomistic simulation of hydrogen diffusion in metals, International Journal of Hydrogen Energy 40 (15) (2015) 5353–5358.

[52] G. Simpson, M. Luskin, D. J. Srolovitz, A theoretical examination of diffusive molecular dynamics, SIAM Journal on Applied Mathematics 76 (6) (2016) 2175–2195.

[53] B. Farmer, M. Luskin, P. Plecháč, G. Simpson, Spin-diffusions and diffusive molecular dynamics, Modelling and Simulation in Materials Science and Engineering 25 (8) (2017) 084003.

[54] M. P. Ariza, I. Romero, M. Ponga, M. Ortiz, Hotqc simulation of nanovoid growth under tension in copper, International Journal of Fracture 174 (1) (2012) 75–85.

[55] M. Ponga, M. Ortiz, M. P. Ariza, Finite-temperature non-equilibrium quasi-continuum analysis of nanovoid growth in copper at low and high strain rates, Mechanics of Materials 90 (2015) 253–267.

[56] M. Ponga, A. A. Ramabathiran, K. Bhattacharya, M. Ortiz, Dynamic behavior of nanovoids in magnesium under hydrostatic tensile stress, Modelling and Simulation in Materials Science and Engineering 24 (6) (2016) 065003.

[57] M. Ponga, M. Ortiz, M. P. Ariza, A comparative study of nanovoid growth in fcc metals, Philosophical Magazine 97 (32) (2017) 2985–3007.

[58] X. Sun, M. P. Ariza, M. Ortiz, K. Wang, Acceleration of diffusive molecular dynamics

simulations through mean field approximation and subcycling time integration, Journal of Computational Physics 350 (2017) 470–492.

[59] S. Balay, S. Abhyankar, M. F. Adams, J. Brown, P. Brune, K. Buschelman, L. Dalcin, V. Eijkhout, W. D. Gropp, D. Kaushik, M. G. Knepley, L. C. McInnes, K. Rupp, B. F. Smith, S. Zampini, H. Zhang, H. Zhang, PETSc users manual, Tech. Rep. ANL-95/11 - Revision 3.7, Argonne National Laboratory (2016).

URL `http://www.mcs.anl.gov/petsc`

Chapter 2

Acceleration of Diffusive Molecular Dynamics Simulations Through Mean Field Approximation and Subcycling Time Integration

(Published in *Journal of Computational Physics*, 350, 470-492, 2017.)

X. Sun [a], M. P. Ariza [b], M. Ortiz [c], K. G. Wang [a]

[a] Department of Aerospace and Ocean Engineering, Virginia Polytechnic Institute and State University, Blacksburg, VA 24061, United States

[b] Escuela Técnica Superior de Ingeniería, Universidad de Sevilla, Sevilla 41092, Spain

[c] Division of Engineering and Applied Science, California Institute of Technology, Pasadena, CA 91125, United States

Abstract

Diffusive Molecular Dynamics (DMD) is a class of recently developed computational models for the simulation of long-term diffusive mass transport at atomistic length scales. Compared to previous atomistic models, e.g., transition state theory based accelerated molecular dynamics, DMD allows the use of larger time-step sizes, but has a higher computational complexity at each time-step due to the need to solve a nonlinear optimization problem at every time-step. This paper presents two numerical methods to accelerate DMD based simulations. First, we show that when a many-body potential function, e.g., embedded atom method (EAM), is employed, the cost of DMD is dominated by the computation of the mean of the potential function and its derivatives, which are high-dimensional random variables. To reduce the cost, we explore both first- and second-order mean field approximations. Specifically, we show that the first-order approximation, which uses a point estimate to calculate the mean, can reduce the cost by two to three orders of magnitude, but may introduce relatively large error in the solution. We show that adding an approximate second-order correction term can significantly reduce the error without much increase in computational cost. Second, we show that DMD can be significantly accelerated through subcycling time integration, as the cost of integrating the empirical diffusion equation is much lower than

that of the optimization solver. To assess the DMD model and the numerical approximation methods, we present two groups of numerical experiments that simulate the diffusion of hydrogen in palladium nanoparticles. In particular, we show that the computational framework is capable of capturing the propagation of an atomically sharp phase boundary over a time window of more than 30 seconds. The effects of the proposed numerical methods on solution accuracy and computation time are also assessed quantitatively.

Keywords

Diffusive Molecular Dynamics, Mean Field Approximation, Subcycling Time Integration, Long-Term Processes, Hydrogen Diffusion, Phase Transformation

2.1 Introduction

In a number of areas of application, the behavior of materials depends sensitively on processes that pertain to dissimilar time scales, ranging from atomic vibrations on the order of femtoseconds (fs), to diffusive transport of mass on the order of seconds or even longer time scales [1, 2, 3, 4]. This disparity of scales poses a significant challenge to atomistic modeling and simulation and has motivated long-standing extensive research. Classical Molecular Dynamics (MD) constitutes a powerful computational tool as it explicitly models the atoms of the material and their interactions. However, its time-step size is limited to the order of

femtosecond by the frequency of atomic vibrations, resulting in total simulation time that is typically less than one microsecond [5]. Extensive research has been devoted to expanding the simulation time window while maintaining an atomistic description of the material [6]. For instance, transition state theory based (TST-based), accelerated MD (AMD) methods [7, 8] and kinetic Monte Carlo (KMC) methods [9] track the transitions between microscopic states without explicitly resolving atomic vibrations. However, for mass transport problems the total time window accessible to these methods is limited by the frequency of individual atom/vacancy hops within the material sample and is typically less than one second [10].

Diffusive Molecular Dynamics (DMD) is a relatively new class of methods that has demonstrated potential for simulating diffusion processes in crystalline solids beyond seconds while maintaining the atomistic resolution. The basic assumption underlying DMD is that the time scale of diffusion is much larger than that of microscopic state transitions. Therefore, at an intermediate time scale, the microscopic state variables — such as the instantaneous position and occupancy of a lattice site — can be considered as random variables. The general idea of DMD can be traced back to the variational Gaussian method proposed by LeSar et al. [11], and the generalized TDDFT (time-dependent density functional theory) method proposed by Perez and Lewis [12]. More recently, Li et al. [13] have extended DMD to handle diffusive mass transport by vacancy exchange and have applied it to study nanoindentation and sintering processes [13] and dislocation reaction mechanisms [14]. Venturini et al. [15, 16, 17] have developed a general framework for diffusive molecular processes, including heat and mass transport. Farmer et al. [18] have formulated a spin-diffusion stochastic

process to interpret the DMD model. A recent theoretical review of DMD can be found in [19].

Following [15], in the present work we couple an empirical diffusion model, or *master equation*, driving the evolution of the mean value of atomic site occupancies, with a non-equilibrium statistical thermodynamics model that determines the mean value of atomic positions by minimizing a grand-canonical free entropy. In terms of numerical implementation, our approach involves the numerical integration of the *master equation*, and the numerical solution of a highly nonlinear optimization problem at every time-step. By working with atomic fractions, the characteristic time-step size of our DMD simulations can be much larger than those based on either AMD or KMC methods, since we do not explicitly track the individual atom/vacancy hops. As a consequence, the time-step size in our calculations is not restricted by the frequency of those events. Instead, it is only limited by the diffusive time scale, e.g., by the speed of the propagation of a phase boundary, which can be as slow as 1 nm/s [20].

However, this time-wise acceleration takes place at some computational expense, since the computational cost of a DMD step, which is dominated by the optimizer, can be significant. Thus, we show that when a many-body embedded atom method (EAM) potential is employed, the computational complexity of our DMD scheme is $\mathcal{O}(Q^2N)$ per time-step, where N and Q denote the number of atomic sites in the material sample and the average number of neighbors of an atomic site within the cut-off distance of the EAM potential, respectively. For many EAM potentials Q can be as large as 100, which makes the $\mathcal{O}(Q^2)$

scaling problematic. By contrast, the one-step cost of classical MD, TST-based AMD, and KMC is typically of the order of $\mathcal{O}(QN)$ [21], $\mathcal{O}(QN)$ [6] and $\mathcal{O}(N \log N)$ [9], respectively. It is therefore of interest to investigate ways of reducing the computational cost of DMD by means of additional numerical approximations.

To this end, we begin by noting that the cost of numerical optimization in calculations employing EAM potentials is dominated by the computation of the mean value of the embedding energy $F(\omega)$ with respect to a trial Gauss distribution, i.e., $\big\langle F(\omega_i)\big\rangle_0$, where ω_i denotes the electron density on site i. For many EAM potentials, e.g., [22, 23], $F(\omega)$ is convex over a broad range of ω, which suggests the use of Jensen's lower bound as an approximation [15], i.e.,

$$\big\langle F(\omega_i)\big\rangle_0 \approx F\big(\langle\omega_i\rangle_0\big). \tag{2.1}$$

This approximation is the result of estimating the random variable ω_i by its mean value. We show that the direct implementation of this approximation suffers from low accuracy in certain cases. In order to overcome this limitation, we introduce a second-order approximation of the form

$$\big\langle F(\omega_i)\big\rangle_0 \approx F\big(\langle\omega_i\rangle_0\big) + \frac{1}{2}F''\big(\langle\omega_i\rangle_0\big)\Big\langle\big(\omega_i - \langle\omega_i\rangle_0\big)^2\Big\rangle_0. \tag{2.2}$$

Finally, we show that, by a further appeal to mean field approximation, the computational complexity of DMD reduces from $\mathcal{O}(Q^2N)$ to $\mathcal{O}(QN)$ per time-step, which results in a considerable acceleration of the calculations, especially where complex potentials are concerned. The second idea explored in this study concerns the use of subcyling on the numerical inte-

gration of the empirical diffusion model. Subcycling naturally suggests itself because the cost of explicit integration of the diffusion equations is significantly lower than that of the optimizer. Subcycling has been widely used in the simulation of multiphysics problems when the time-step limit or computational cost of different physical fields differ significantly [24, 25, 26].

In order to verify the proposed numerical algorithms and assess their performance, we simulate the diffusion of hydrogen (H) in palladium (Pd) nanoparticles. This problem is relevant to several energy-related areas of application such as electrical batteries [4] and hydrogen storage systems [1]. In this system, the fundamental event is the hopping of H atoms among the interstitial sites of the primary metal lattice. However, the overall diffusion process often takes minutes to hours to reach equilibrium and occurs simultaneously with a number of phenomena of interest such as lattice distortion [1], slow propagation of phase boundaries [20], avalanching strain reversion [27], and hydrogen-induced structural disintegration [28], all of which are elucidated at the atomistic level. The use of DMD therefore suggests naturally for this type of systems.

The remainder of this paper is organized as follows. Section 2.2 summarizes the DMD model equations. Section 2.3 presents the aforementioned numerical methods for accelerating DMD simulations. Section 2.4 presents two groups of numerical experiments that simulate the long-term dynamics of hydrogen in palladium nanomaterials, in which the proposed numerical methods are assessed quantitatively. Finally, a summary and some concluding remarks are provided in Section 2.5.

2.2 Physical model

As already mentioned in the previous section, the term Diffusive Molecular Dynamics (DMD) was introduced by Li et al. [13] in 2011 to describe a novel atomistic computational model capable of coupling an empirical diffusion law (an ordinary differential equation, ODE) with a probabilistic description of the microscopic state variables. More recently, Venturini et al. [15] formulated a more general theory based on the same fundamental assumption, and applied it to both heat and mass transport problems. For the sake of completeness and convenience, we summarize in this section its generalized version.

2.2.1 Non-equilibrium statistical thermodynamics model

We consider a crystal lattice consisting of N atomic sites, which at any time instance can be occupied by one of R species of particles, e.g., atoms, ions, etc., or unoccupied. Therefore, the instantaneous status of a site can be tracked using an occupancy function, defined as

$$\boldsymbol{n}_i = \begin{bmatrix} n_{i1} \\ \vdots \\ n_{iR} \end{bmatrix}, \quad i = 1, \cdots, N, \tag{2.3}$$

where

$$n_{ik} = \begin{cases} 1, & \text{if site } i \text{ is occupied by species } k \\ 0, & \text{otherwise} \end{cases}, \quad k = 1, 2, \cdots, R. \tag{2.4}$$

The instantaneous position and momentum of site i are denoted by $\boldsymbol{q}_i$ and $\boldsymbol{p}_i$, respectively. Based on the assumption of scale separation and the ergodic hypothesis, these microscopic state variables can be viewed as random variables that have a joint probability distribution characterized by density function $\rho\big(\{\boldsymbol{q}\},\{\boldsymbol{p}\},\{\boldsymbol{n}\}\big)$, where $\{\boldsymbol{q}\}=\{\boldsymbol{q}_i\}_{i=1}^N$, $\{\boldsymbol{p}\}=\{\boldsymbol{p}_i\}_{i=1}^N$ and $\{\boldsymbol{n}\}=\{\boldsymbol{n}_i\}_{i=1}^N$. This function ρ can be directly specified as in [13]. More generally, it can be determined by applying the Jaynes' principles of maximum entropy [29, 30], that is, by maximizing the information-theoretical entropy

$$\mathcal{S}[\rho]=-k_{\mathrm{B}}\langle\log\rho\rangle, \tag{2.5}$$

among all probability measures consistent with the constraints imposed on the system. Here, k_{B} is the Boltzmann's constant, and $\langle\cdot\rangle$ represents the expectation or phase average operator [15]. Moreover, it is assumed that the Hamiltonian of the system, denoted by $\mathcal{H}$, can be written as a site-wise summation, i.e.,

$$\mathcal{H}=\sum_{i=1}^{N}h_i=\sum_{i=1}^{N}\Big(V_i\big(\{\boldsymbol{q}\},\{\boldsymbol{n}\}\big)+\frac{1}{2m(\boldsymbol{n}_i)}|\boldsymbol{p}_i|^2\Big), \tag{2.6}$$

where h_i is the local Hamiltonian associated with site i, V_i represents the interatomic potential energy, and $m(\boldsymbol{n}_i)$ denotes the mass of site i. In analogy to the general definition of the average internal energy, $E=\langle\mathcal{H}\rangle$, and the average particle number, $X=\langle N\rangle$, for the grand

canonical ensemble, we introduce particle energies, e_i, and atomic fractions, $\boldsymbol{x}_i$, defined as

$$e_i = \langle h_i \rangle, \quad \boldsymbol{x}_i = \langle \boldsymbol{n}_i \rangle, \quad i = 1, \cdots, N. \tag{2.7}$$

Maximization of $\mathcal{S}[\rho]$ subjected to the local constraints given by Eq. (2.7) yields

$$\rho = \frac{1}{\Xi} \mathrm{e}^{-\{\beta\}^{\mathrm{T}}\{h\} + \{\gamma\}^{\mathrm{T}}\{\boldsymbol{n}\}}, \tag{2.8}$$

where Ξ is the partition function, and $\{\beta\} = \{\beta_i\}_{i=1}^N$ and $\{\boldsymbol{\gamma}\} = \{\boldsymbol{\gamma}_i\}_{i=1}^N$ are Lagrange multipliers. In comparison with equilibrium statistical thermodynamics, Eq. (2.8) can be interpreted as the non-equilibrium generalization of the Gibbs grand-canonical probability density function. Also, β_i and γ_i can be interpreted as thermodynamic beta and nondimensional chemical potential of site i, respectively [15].

For most material models, V_i is typically a nonlinear function, and therefore the calculation of the particle energies, e_i, is generally intractable. Venturini et al. [15] proposed an approximation theory, in which $\mathcal{S}[\rho]$ is maximized within a finite-dimensional trial space $\mathcal{P}_0$, spanned by a pre-specified class of trial Hamiltonians $\{h_0\}$. As a result, maximizing $\mathcal{S}[\rho]$ within $\mathcal{P}_0$ is equivalent to minimizing the mean field free entropy, i.e.,

$$\min_{\{\boldsymbol{\alpha}\}} \ \mathcal{F}\big(\{\beta\}, \{\boldsymbol{\gamma}\}; \{h_0\}\big) = k_{\mathrm{B}}\{\beta\}^{\mathrm{T}}\big\{\langle h - h_0 \rangle_0\big\} - k_{\mathrm{B}} \log \Xi_0, \tag{2.9}$$

where $\{\boldsymbol{\alpha}\}$ is a finite set of parameters that characterize $\{h_0\}$. $\langle \cdot \rangle_0$ denotes the expectation

operator under the trial probability density function, and Ξ_0 is the trial partition function. Within this work, we assume that the diffusion of heat is much faster than the diffusion of mass, therefore the particle temperature, $T_i = 1/(k_{\mathrm{B}}\beta_i)$, becomes uniform over all the sites, and is equal to the temperature T defined in equilibrium thermodynamics[1]. In this case, Eq. (2.9) reduces to

$$\min_{\{\boldsymbol{\alpha}\}} \ \mathcal{F}\big(T, \{\boldsymbol{\gamma}\}; \{h_0\}\big) = \frac{1}{T}\sum_{i=1}^{N}\langle h_i - h_{0i}\rangle_0 - k_{\mathrm{B}}\log \Xi_0. \tag{2.10}$$

Clearly, if $\{h_0\}$ is designed to have a simple structure, the above optimization problem can be solved numerically or even analytically. Notably, the local equilibrium conditions derived from Eq. (2.10) can be viewed as a series of atomistic-scale equations of state (EOS) that holds at any *time point* on the scale of diffusion, provided that this scale is much larger than that of the fundamental events (e.g., the hopping of individual atoms).

2.2.2 Discrete diffusion law

Within the DMD model, an empirical diffusion law is responsible for *driving* slow diffusion processes at the atomistic length scale. At any time point, mass balance on site i requires

$$\dot{\boldsymbol{x}}_i = \sum_{j=1,\ j\neq i}^{N} \boldsymbol{J}_{ij}, \tag{2.11}$$

[1]Application of the DMD model to problems involving heat transport and non-uniform T_i can be found in [15, 31]

where $\boldsymbol{J}_{ij} = -\boldsymbol{J}_{ji}$ denotes the discrete mass flux from site j to site i. For simplicity, $\boldsymbol{J}_{ij}$ has always been assumed to be of first-order with respect to the difference in chemical potential between the two sites. Therefore, Eq. (2.11) becomes

$$\dot{x}_{ik} = \sum_{j=1,\ j\neq i}^{N} B_{ij,k} \frac{x_{ik} + x_{jk}}{2} k_{\mathrm{B}}(\gamma_{jk} - \gamma_{ik}), \quad k = 1, ..., R, \tag{2.12}$$

where $B_{ij,k}$ is a model parameter that represents the diffusivity of species k between sites i and j.

The optimization problem in Eq. (2.10) together with Eq. (2.12) form a closed system of equations that governs long-term diffusive transport of mass on an atomistic length scale, which certainly characterizes the DMD model.

2.2.3 Example: Diffusion of hydrogen in metal nanomaterials

To illustrate the DMD model described above, here we consider the diffusion of hydrogen in metals as an example problem. In this case, diffusion is dominated by the hopping of H atoms among the interstitial sites of the lattice. This problem is relevant to several energy-related application areas such as electrical batteries [4] and hydrogen storage [1], and will be further investigated to assess the numerical approximation methods developed in the present research.

Specifically, we consider a crystal lattice where the base lattice sites are always occupied by metal atoms, while the interstitial sites are either occupied by an H atom, or unoccupied.

For ease of reference, we denote the base lattice sites by I_{M}, and the interstitial sites by I_{H}. The trial Hamiltonians introduced in Eq. (2.10) are chosen to be of the form

$$h_{0i}(\boldsymbol{q}_i, \boldsymbol{p}_i, n_i;\ \bar{\boldsymbol{q}}_i, \sigma_i, \bar{\boldsymbol{p}}_i, \gamma_{0i}) = \begin{cases} \dfrac{k_{\mathrm{B}}T}{2\sigma_i^2}|\boldsymbol{q}_i - \bar{\boldsymbol{q}}_i|^2 + \dfrac{1}{2m_{\mathrm{M}}}|\boldsymbol{p}_i - \bar{\boldsymbol{p}}_i|^2, & \text{if } i \in I_{\mathrm{M}} \\ \dfrac{k_{\mathrm{B}}T}{2\sigma_i^2}|\boldsymbol{q}_i - \bar{\boldsymbol{q}}_i|^2 + \dfrac{1}{2m_{\mathrm{H}}}|\boldsymbol{p}_i - \bar{\boldsymbol{p}}_i|^2 - k_{\mathrm{B}}T\gamma_{0i}n_i, & \text{if } i \in I_{\mathrm{H}} \end{cases}, \tag{2.13}$$

where $\bar{\boldsymbol{q}}_i$, σ_i, $\bar{\boldsymbol{p}}_i$, and γ_{0i} are parameters that characterize the trial space. Herein, m_{M} and m_{H} denote the atomic mass of the metal and hydrogen, respectively. It can be shown that $\bar{\boldsymbol{q}}_i$ and σ_i are the mean and standard deviation of $\boldsymbol{q}_i$, respectively, and $\bar{\boldsymbol{p}}_i$ is the mean value of $\boldsymbol{p}_i$.

Moreover, γ_{0i} indicates the dependence of chemical potential on the H atomic fraction x_i. Specifically, by calculating $\langle n_i \rangle_0$ and applying the relation $\langle n_i \rangle_0 = x_i$, we obtain

$$\gamma_i = \log \frac{x_i}{1 - x_i} - \gamma_{0i}. \tag{2.14}$$

Details of the derivation are provided in 2.A. From Eqs. (2.40), (2.42) and (2.14), the trial probability density function ρ_0 can be derived, i.e.,

$$\begin{aligned} \rho_0 = \frac{1}{\Xi_0} \exp\Bigg(&- \sum_{i \in I_{\mathrm{M}} \cup I_{\mathrm{H}}} \frac{1}{2\sigma_i^2}|\boldsymbol{q}_i - \bar{\boldsymbol{q}}_i|^2 - \sum_{i \in I_{\mathrm{M}}} \frac{1}{2k_{\mathrm{B}}Tm_{\mathrm{M}}}|\boldsymbol{p}_i - \bar{\boldsymbol{p}}_i|^2 \\ &- \sum_{i \in I_{\mathrm{H}}} \left(\frac{1}{2k_{\mathrm{B}}Tm_{\mathrm{H}}}|\boldsymbol{p}_i - \bar{\boldsymbol{p}}_i|^2 - n_i \log \frac{x_i}{1 - x_i} \right) \Bigg), \end{aligned} \tag{2.15}$$

with

$$\Xi_0 = \prod_{i\in I_{\mathrm{M}}} \left(\frac{\sigma_i\sqrt{k_{\mathrm{B}}Tm_{\mathrm{M}}}}{\hbar}\right)^3 \prod_{i\in I_{\mathrm{H}}} \left(\frac{\sigma_i\sqrt{k_{\mathrm{B}}Tm_{\mathrm{H}}}}{\hbar}\right)^3 \frac{1}{1-x_i}, \tag{2.16}$$

where $\hbar$ is the reduced Planck's constant. After straightforward derivations, and using Eq. (2.14), the optimization problem stated in Eq. (2.10) becomes

$$\begin{aligned}
&\min_{\{\bar{\boldsymbol{q}}\},\{\sigma\},\{\bar{\boldsymbol{p}}\},\{x\}} \mathcal{F}\big(T,\{\gamma\};\{\bar{\boldsymbol{q}}\},\{\sigma\},\{\bar{\boldsymbol{p}}\},\{x\}\big) \\
&= \frac{1}{T}\langle V\rangle_0 + \frac{1}{2Tm_{\mathrm{M}}}\sum_{i\in I_{\mathrm{M}}}\bar{\boldsymbol{p}}_i^2 + \frac{1}{2Tm_{\mathrm{H}}}\sum_{i\in I_{\mathrm{H}}} x_i\bar{\boldsymbol{p}}_i^2 + \frac{3}{2}k_{\mathrm{B}}\sum_{i\in I_{\mathrm{M}}}\left(\log\frac{\hbar^2}{k_{\mathrm{B}}Tm_{\mathrm{M}}\sigma_i^2} - 1\right) \\
&+ \frac{3}{2}k_{\mathrm{B}}\sum_{i\in I_{\mathrm{H}}}\left(\log\frac{\hbar^2}{k_{\mathrm{B}}Tm_{\mathrm{H}}\sigma_i^2} + x_i - 2\right) + k_{\mathrm{B}}\sum_{i\in I_{\mathrm{H}}}\big(x_i\log x_i + (1-x_i)\log(1-x_i) - \gamma_i x_i\big).
\end{aligned} \tag{2.17}$$

In analogy to the grand canonical ensemble, T and $\{\gamma\}$ are regarded as constant on each site and then we calculate optimal values of $\{\bar{\boldsymbol{q}}\}$, $\{\sigma\}$, $\{\bar{\boldsymbol{p}}\}$ and $\{x\}$. Enforcing the first-order necessary condition

$$\frac{\partial\mathcal{F}}{\partial\bar{\boldsymbol{p}}_i} = 0, \quad \forall i \in I_{\mathrm{M}}\cup I_{\mathrm{H}}, \tag{2.18}$$

yields

$$\bar{\boldsymbol{p}}_i = 0, \quad \forall i \in I_{\mathrm{M}}\cup I_{\mathrm{H}}. \tag{2.19}$$

Then, by applying the first-order necessary condition to x_i

$$\frac{\partial\mathcal{F}}{\partial x_i} = 0, \quad \forall i \in I_{\mathrm{H}}, \tag{2.20}$$

we can compute γ_i as a function of the optimal values of $\{\bar{\boldsymbol{q}}\}$, $\{\sigma\}$ and $\{x\}$, namely,

$$\gamma_i = \frac{3}{2} + \log\frac{x_i}{1-x_i} + \frac{1}{k_{\mathrm{B}}T}\frac{\partial\langle V\rangle_0}{\partial x_i}, \quad \forall i \in I_{\mathrm{H}}. \tag{2.21}$$

Notably, γ_i can be interpreted as a nondimensional chemical potential of site i. Therefore, Eq. (2.21) shows that when calculating the chemical potential, unlike the classical entropy-of-mixing relation that only depends on the fraction of its own atomic site, the DMD model also involves the interatomic potential and the present microscopic state variables. With the expression of γ_i which satisfies the necessary condition for x_i, and by substituting $\bar{\boldsymbol{p}}_i$ in Eq. (2.17) using Eq. (2.19), the optimization problem simplifies to

$$\begin{aligned}
&\min_{\{\bar{\boldsymbol{q}}\},\{\sigma\}} \mathcal{F}\big(T,\{\gamma\};\{\bar{\boldsymbol{q}}\},\{\sigma\},\{x\}\big) \\
&= \frac{1}{T}\langle V\rangle_0 + \frac{3}{2}k_{\mathrm{B}}\sum_{i\in I_{\mathrm{M}}}\left(\log\frac{\hbar^2}{k_{\mathrm{B}}Tm_{\mathrm{M}}\sigma_i^2} - 1\right) + \frac{3}{2}k_{\mathrm{B}}\sum_{i\in I_{\mathrm{H}}}\left(\log\frac{\hbar^2}{k_{\mathrm{B}}Tm_{\mathrm{H}}\sigma_i^2} + x_i - 2\right) \\
&+ k_{\mathrm{B}}\sum_{i\in I_{\mathrm{H}}}\big(x_i\log x_i + (1-x_i)\log(1-x_i) - \gamma_i x_i\big).
\end{aligned} \tag{2.22}$$

Herein, the optimization variables are $\{\bar{\boldsymbol{q}}\}$ and $\{\sigma\}$. The thermodynamics model formulated in Eq. (2.22) is then coupled with a discrete diffusion law of the form of Eq. (2.12). For simplicity, but without loss of generality, we restrict diffusive transport within one shell of neighbors, and apply a constant bondwise diffusivity B_0. As a result, Eq. (2.12) simplifies to

$$\dot{x}_i = -k_{\mathrm{B}}B_0\sum_{j\in\mathcal{N}_{\mathrm{H},i}^{(1)}}\frac{x_i+x_j}{2}(\gamma_i-\gamma_j), \quad \forall i \in I_{\mathrm{H}}, \tag{2.23}$$

where $\mathcal{N}_{\mathrm{H},i}^{(1)}$ denotes the first shell of interstitial neighbors of site i.

2.3 Numerical methods

The DMD model couples a nonlinear optimization problem (Eq. (2.10)) with a first-order, nonlinear ordinary differential equation (ODE) (Eq. (2.12)). An efficient strategy to solve this system comprises the discretization of the ODE using an explicit time integrator, and solving the optimization problem once per time-step using a quasi-Newton method. Algorithm 1 provides a pseudocode that implements this approach, using the hydrogen diffusion problem described in Section 2.2.3 as an example. The main steps involved are illustrated in Fig. 2.1.

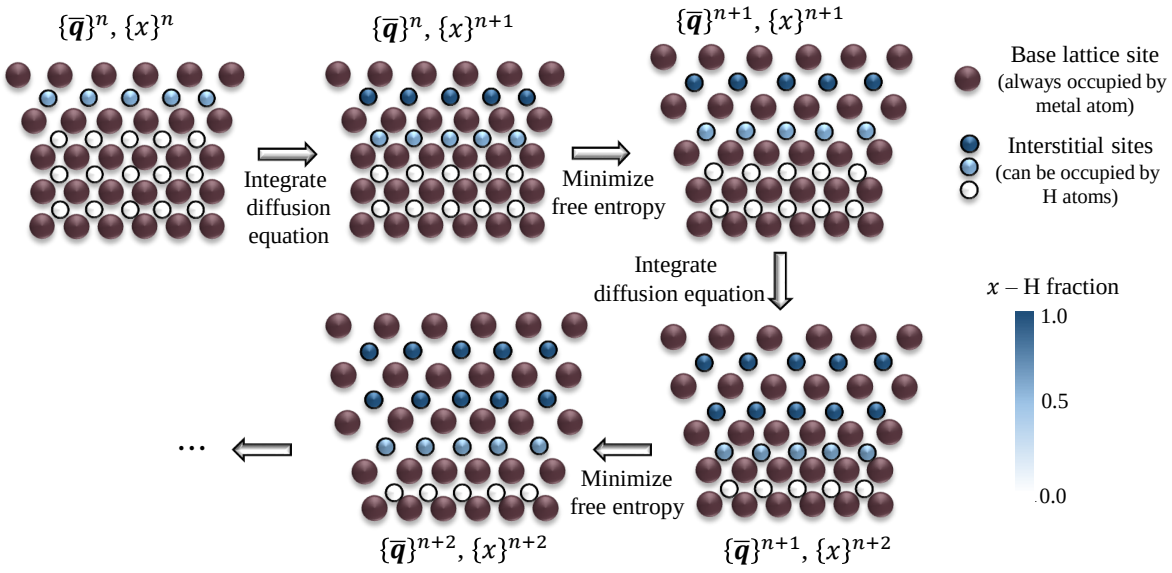

Figure 2.1: Illustration of a DMD simulation that features the diffusive transport of H atoms (from top to bottom) and the associated lattice expansion.

Algorithm 1 Solution of the DMD model equations.

Input: $\{x\}^0$ (initial condition), $t_{\max}$ (final time)
Begin
initialization:
    $t = 0,\ n = 0$
    minimize $\mathcal{F}\big(\{\bar{\boldsymbol{q}}\}, \{\sigma\}, \{x\}^0\big) \Rightarrow \{\bar{\boldsymbol{q}}\}^0, \{\sigma\}^0$
    $\gamma_i^0 \leftarrow \dfrac{3}{2} + \log\dfrac{x_i^0}{1-x_i^0} + \dfrac{1}{k_{\mathrm{B}}T}\dfrac{\partial\langle V\rangle_0}{\partial x_i}\Big|^0, \quad \forall i \in I_{\mathrm{H}}$
time loop:
    while $t < t_{\max}$ **do**
        solve Eq. (2.23) for one time-step, i.e.,
        $$x_i^{n+1} \leftarrow x_i^n - k_{\mathrm{B}}B_0\Delta t \sum_{j\in\mathcal{N}_{\mathrm{H},i}^{(1)}} \frac{1}{2}(x_i^n + x_j^n)(\gamma_i^n - \gamma_j^n), \quad \forall i \in I_{\mathrm{H}}$$
        minimize $\mathcal{F}\big(\{\bar{\boldsymbol{q}}\}, \{\sigma\}, \{x\}^{n+1}\big) \Rightarrow \{\bar{\boldsymbol{q}}\}^{n+1}, \{\sigma\}^{n+1}$:
        Begin
            $\boldsymbol{X} \equiv \big\{\{\bar{\boldsymbol{q}}\}, \{\sigma\}\big\}$
            $\mathcal{F}(\boldsymbol{X}) \equiv \mathcal{F}\big(\{\bar{\boldsymbol{q}}\}, \{\sigma\}, \{x\}^{n+1}\big)$
            for $k \leftarrow 0, \boldsymbol{X}^0 \leftarrow \big\{\{\bar{\boldsymbol{q}}\}^n, \{\sigma\}^n\big\};\ k < k_{\max}$ **do**
                compute approximate Hessian matrix $\mathcal{H}^k$
                $\Delta\boldsymbol{X} \leftarrow -(\mathcal{H}^k)^{-1}\nabla\mathcal{F}(\boldsymbol{X}^k)$
                determine step size τ by line search
                $\boldsymbol{X}^{k+1} \leftarrow \boldsymbol{X}^k + \tau\Delta\boldsymbol{X}$
                if $\big|\mathcal{F}(\boldsymbol{X}^{k+1}) - \mathcal{F}(\boldsymbol{X}^k)\big| < \epsilon_1$ or $\dfrac{\big|\mathcal{F}(\boldsymbol{X}^{k+1}) - \mathcal{F}(\boldsymbol{X}^k)\big|}{\big|\mathcal{F}(\boldsymbol{X}^k)\big|} < \epsilon_2$ **then**
                    break
                end if
                $k \leftarrow k + 1$
            end for
        End
        $\gamma_i^{n+1} \leftarrow \dfrac{3}{2} + \log\dfrac{x_i^{n+1}}{1-x_i^{n+1}} + \dfrac{1}{k_{\mathrm{B}}T}\dfrac{\partial\langle V\rangle_0}{\partial x_i}\Big|^{n+1}, \quad \forall i \in I_{\mathrm{H}}$
        $t \leftarrow t + \Delta t,\ n \leftarrow n + 1$
    end while
End
Output: $\{\gamma\}^n,\ \{\bar{\boldsymbol{q}}\}^n,\ \{\sigma\}^n,\ \{x\}^n$

2.3.1 Mean field approximation

The optimization problem (Eq. 2.22) entails computing the mean value of the interatomic potential (i.e., $\langle V \rangle_0$) at every quasi-Newton iteration. For many-body potentials, these computations are expensive, as they involve high-dimensional integration. For instance, the embedded atom method (EAM) is a class of many-body potentials widely used to describe metallic systems [32]. For binary systems such as metal-hydrogen, it carries the form

$$\begin{aligned} V\big(\{\boldsymbol{q}\},\{n\}\big) = &\sum_{i\in I_{\mathrm{M}}} F_{\mathrm{M}}(\omega_i) + \sum_{i\in I_{\mathrm{H}}} n_i F_{\mathrm{H}}(\omega_i) + \frac{1}{2}\sum_{i,\ j\in I_{\mathrm{M}},\ i\neq j} \phi_{\mathrm{MM}}(r_{ij}) \\ &+ \sum_{i\in I_{\mathrm{H}},\ j\in I_{\mathrm{M}}} n_i \phi_{\mathrm{MH}}(r_{ij}) + \frac{1}{2}\sum_{i,\ j\in I_{\mathrm{H}},\ i\neq j} n_i n_j \phi_{\mathrm{HH}}(r_{ij}), \end{aligned} \tag{2.24}$$

where $r_{ij} = |\boldsymbol{q}_i - \boldsymbol{q}_j|$, whereas ϕ_{MM}, ϕ_{MH}, and ϕ_{HH} denote the pair energy between metal-metal, metal-hydrogen, and hydrogen-hydrogen atom pairs, respectively. Also, $F_{\mathrm{M}}(\omega)$ and $F_{\mathrm{H}}(\omega)$ indicate the embedding energy function for metal and hydrogen atoms, respectively, and are defined in terms of a pseudo-density function, ω_i, which writes as

$$\omega_i = \sum_{j\in I_{\mathrm{M}},\ j\neq i} f_{\mathrm{M}}(r_{ij}) + \sum_{j\in I_{\mathrm{H}},\ j\neq i} n_j f_{\mathrm{H}}(r_{ij}), \tag{2.25}$$

i.e., the summation of electron density functions $f_{\mathrm{M}}(r)$ and $f_{\mathrm{H}}(r)$, for metal and hydrogen atoms, respectively. The pair functions $\phi_{\mathrm{MM}}(r_{ij})$, $\phi_{\mathrm{MH}}(r_{ij})$, $\phi_{\mathrm{HH}}(r_{ij})$, $f_{\mathrm{M}}(r_{ij})$ and $f_{\mathrm{H}}(r_{ij})$ are usually defined in either analytical or tabular form.

For the trial probability density function defined in Eq. (2.15), the atomic position $\boldsymbol{q}_i$, mo-

mentum $\boldsymbol{p}_i$ and occupancy n_i are independent with each other. Therefore, the mean value of the EAM potential can be written as

$$\begin{aligned}\langle V\rangle_0 = &\sum_{i\in I_{\mathrm{M}}}\big\langle F_{\mathrm{M}}(\omega_i)\big\rangle_0 + \sum_{i\in I_{\mathrm{H}}} x_i\big\langle F_{\mathrm{H}}(\omega_i)\big\rangle_0 + \frac{1}{2}\sum_{i,\ j\in I_{\mathrm{M}},\ i\neq j}\big\langle \phi_{\mathrm{MM}}(r_{ij})\big\rangle_0 \\ &+ \sum_{i\in I_{\mathrm{H}},\ j\in I_{\mathrm{M}}} x_i\big\langle \phi_{\mathrm{MH}}(r_{ij})\big\rangle_0 + \frac{1}{2}\sum_{i,\ j\in I_{\mathrm{H}},\ i\neq j} x_i x_j\big\langle \phi_{\mathrm{HH}}(r_{ij})\big\rangle_0.\end{aligned} \tag{2.26}$$

For a three-dimensional (3D) material sample, $\langle F_{\mathrm{M}}(\omega_i)\rangle_0$ and $\langle F_{\mathrm{H}}(\omega_i)\rangle_0$ are $3(Q{+}1)$-dimensional integrals, where Q denotes the number of neighbor sites within the cut-off distance of the EAM potential, which in practice is typically of the order of 100. Therefore, these integrals cannot be evaluated analytically due to the complex form of the embedding energy function and the pair energy function, and thus numerical integration methods are needed.

The Monte Carlo (MC) method has been widely used to evaluate high-dimensional integrals [33]. However, its computational cost is high, thus evaluating Eq. (2.26) with N_{m} random samples invokes $\mathcal{O}(QNN_{\mathrm{m}})$ calls of the pair functions mentioned above. N_{m} is usually greater than 10^4, and Eq. (2.26) (and its derivatives) needs to be evaluated within every quasi-Newton iteration at every time-step. To facilitate long-term DMD simulations of relatively large material samples, more efficient numerical integration methods are desirable.

An alternative approach is to use Gaussian quadratures [34]. Thus, evaluating Eq. (2.26) using the classical Gaussian quadratures requires $\mathcal{O}(QNN_{\mathrm{g}}^{3(Q+1)})$ calls of the pair functions, where N_{g} denotes the number of Gaussian points for each variable of integration, which is proven impractical even for $N_{\mathrm{g}} = 2$. A feasible strategy to accelerate Gaussian quadratures

for high-dimensional integration is to introduce a sparse grid [35]. As we show in 2.B, this approach can reduce the complexity of evaluating Eq. (2.26) to $\mathcal{O}(Q^2N)$, which is still high for long-term DMD simulations.

Next, we present two numerical schemes based on mean field approximation, which effectively reduce the computational complexity of evaluating Eq. (2.26) to $\mathcal{O}(QN)$. It is noteworthy that the optimization solver also requires computing the gradients of the objective function $\mathcal{F}$, and hence the gradients of $\langle V\rangle_0$. Evaluating the gradients of $\langle V\rangle_0$ has the same order of complexity as $\langle V\rangle_0$ by the proposed mean field approximations.

First-order mean field approximation

Expanding the embedding energy $F(\omega_i)$ about the mean value of ω_i, we obtain

$$F(\omega_i) = F\big(\langle\omega_i\rangle_0\big) + F'\big(\langle\omega_i\rangle_0\big)\big(\omega_i - \langle\omega_i\rangle_0\big) + \frac{1}{2}F''\big(\langle\omega_i\rangle_0\big)\big(\omega_i - \langle\omega_i\rangle_0\big)^2 + h.o.t., \tag{2.27}$$

where $F(\omega)$ represents both $F_{\mathrm{M}}(\omega)$ and $F_{\mathrm{H}}(\omega)$ in Eq. (2.26), $F' = \mathrm{d}F/\mathrm{d}\omega$, $F'' = \mathrm{d}^2F/\mathrm{d}\omega^2$, and "*h.o.t.*" represents, collectively, the higher-order terms of the Taylor series. Evaluating the mean of Eq. (2.27) yields

$$\big\langle F(\omega_i)\big\rangle_0 = \; F\big(\langle\omega_i\rangle_0\big) + \frac{1}{2}F''\big(\langle\omega_i\rangle_0\big)\big(\langle\omega_i^2\rangle_0 - \langle\omega_i\rangle_0^2\big) + h.o.t. \tag{2.28}$$

If only the first term on the right-hand-side of Eq. 2.28 is retained, we obtain a first-order

approximation, i.e.,

$$\big\langle F(\omega_i)\big\rangle_0 \approx F\big(\langle\omega_i\rangle_0\big). \tag{2.29}$$

This approximation relies on a point estimate to calculate the mean. In particular, if the embedding energy function $F(\omega)$ is convex, this first-order approximation represents a lower bound of the true value (i.e. Jensen's inequality). Substituting Eq. (2.29) into Eq. (2.26) yields

$$\begin{aligned}\langle V\rangle_0 \approx &\sum_{i\in I_{\mathrm{M}}} F_{\mathrm{M}}\big(\langle\omega_i\rangle_0\big) + \sum_{i\in I_{\mathrm{H}}} x_i F_{\mathrm{H}}\big(\langle\omega_i\rangle_0\big) + \frac{1}{2}\sum_{i,\ j\in I_{\mathrm{M}},\ i\neq j}\big\langle\phi_{\mathrm{MM}}(r_{ij})\big\rangle_0 \\ &+ \sum_{i\in I_{\mathrm{H}},\ j\in I_{\mathrm{M}}} x_i\big\langle\phi_{\mathrm{MH}}(r_{ij})\big\rangle_0 + \frac{1}{2}\sum_{i,\ j\in I_{\mathrm{H}},\ i\neq j} x_i x_j\big\langle\phi_{\mathrm{HH}}(r_{ij})\big\rangle_0,\end{aligned} \tag{2.30}$$

where

$$\langle\omega_i\rangle_0 = \sum_{j\in I_{\mathrm{M}},\ j\neq i}\big\langle f_{\mathrm{M}}(r_{ij})\big\rangle_0 + \sum_{j\in I_{\mathrm{H}},\ j\neq i} x_j\big\langle f_{\mathrm{H}}(r_{ij})\big\rangle_0. \tag{2.31}$$

The evaluation of $\langle\omega_i\rangle_0$ in Eq. (2.31) is straightforward and involves only two-body interactions. As a result, the first-order mean field approximation introduced in Eq. (2.29) reduces the computational cost of Eq. (2.26) to $\mathcal{O}(QN)$. Further details of the computational complexity analysis are provided in 2.C.

Remark 1. *The first-order approximation described above has been used to calculate the mean values of EAM potentials in both equilibrium [36] and non-equilibrium systems [13, 37]. However, its accuracy requires further investigation. In Section 2.4.2, we will show that for a series of hydrogen absorption simulations involving sharp phase boundaries, the first-order approximation may introduce relatively large errors. This observation motivates us to extend*

the mean field approximation towards second-order while maintaining the same computational complexity.

Second-order mean field approximation

From Eq. (2.28), a second-order approximation of $\big\langle F(\omega_i)\big\rangle_0$ can be obtained, i.e.,

$$\big\langle F(\omega_i)\big\rangle_0 \approx F\big(\langle\omega_i\rangle_0\big) + \frac{1}{2}F''\big(\langle\omega_i\rangle_0\big)\big(\langle\omega_i^2\rangle_0 - \langle\omega_i\rangle_0^2\big). \tag{2.32}$$

In particular, the variance of ω_i in the second-order term can be formulated as

$$\langle\omega_i^2\rangle_0 - \langle\omega_i\rangle_0^2 = C_{\mathrm{MM},i} + 2C_{\mathrm{MH},i} + C_{\mathrm{HH},i} + C_{0,i} + C_{1,i}, \tag{2.33}$$

where

$$\begin{aligned}
C_{\mathrm{MM},i} &= \sum_{j,\ l\in I_{\mathrm{M}},\ j\neq l} \mathrm{Cov}\big[f_{\mathrm{M}}(r_{ij}),\ f_{\mathrm{M}}(r_{il})\big],\\
C_{\mathrm{MH},i} &= \sum_{j\in I_{\mathrm{M}},\ l\in I_{\mathrm{H}}} x_l\mathrm{Cov}\big[f_{\mathrm{M}}(r_{ij}),\ f_{\mathrm{H}}(r_{il})\big],\\
C_{\mathrm{HH},i} &= \sum_{j,\ l\in I_{\mathrm{H}},\ j\neq l} x_jx_l\mathrm{Cov}\big[f_{\mathrm{H}}(r_{ij}),\ f_{\mathrm{H}}(r_{il})\big],\\
C_{0,i} &= \sum_{j\in I_{\mathrm{M}}} \Big(\big\langle f_{\mathrm{M}}^2(r_{ij})\big\rangle_0 - \big\langle f_{\mathrm{M}}(r_{ij})\big\rangle_0^2\Big),\\
C_{1,i} &= \sum_{j\in I_{\mathrm{H}}} \Big(x_j\big\langle f_{\mathrm{H}}^2(r_{ij})\big\rangle_0 - x_j^2\big\langle f_{\mathrm{H}}(r_{ij})\big\rangle_0^2\Big),\quad j\neq i,\ l\neq i,
\end{aligned} \tag{2.34}$$

where $\mathrm{Cov}[\cdot,\cdot]$ represents the covariance operator. Notably, the first three equations of (2.34) involve three-body interactions. As a result, evaluating the mean value of the EAM potential

(i.e., Eq. (2.26)) entails a computational complexity of $\mathcal{O}(Q^2N)$. To reduce this complexity, we estimate the covariances in Eq. (2.34) off-line, based on a reference configuration. Specifically, we substitute the covariances through the following approximations

$$
\begin{aligned}
C_{\mathrm{MM},i} &\approx C^{(0)}_{\mathrm{MM},i} = \sum_{j,\ l\in I_{\mathrm{M}},\ j\neq l} \mathrm{Cov}\Big[f_{\mathrm{M}}\big(r^{(0)}_{ij}\big),\ f_{\mathrm{M}}\big(r^{(0)}_{il}\big)\Big], \\
C_{\mathrm{MH},i} &\approx C^{(0)}_{\mathrm{MH},i} = \sum_{j\in I_{\mathrm{M}},\ l\in I_{\mathrm{H}}} x_l \mathrm{Cov}\Big[f_{\mathrm{M}}\big(r^{(0)}_{ij}\big),\ f_{\mathrm{H}}\big(r^{(0)}_{il}\big)\Big], \\
C_{\mathrm{HH},i} &\approx C^{(0)}_{\mathrm{HH},i} = \sum_{j,\ l\in I_{\mathrm{H}},\ j\neq l} x_j x_l \mathrm{Cov}\Big[f_{\mathrm{H}}\big(r^{(0)}_{ij}\big),\ f_{\mathrm{H}}\big(r^{(0)}_{il}\big)\Big], \quad j\neq i,\ l\neq i,
\end{aligned}
\tag{2.35}
$$

where the superscript "(0)" on r_{ij} and r_{il} refers to the reference configuration, which could be, for example, an equilibrium state relevant to the DMD analysis. This approximation can be justified, in the context of solid crystals, by the fact that the displacive atomic movements in a diffusion-dominated process are often small compared to the lattice spacing at equilibrium.

Substituting Eqs. (2.32), (2.33), and (2.35) into Eq. (2.26) yields

$$
\begin{aligned}
\langle V\rangle_0 \approx{}& \sum_{i\in I_{\mathrm{M}}} F_{\mathrm{M}}\big(\langle\omega_i\rangle_0\big) + \sum_{i\in I_{\mathrm{H}}} x_i F_{\mathrm{H}}\big(\langle\omega_i\rangle_0\big) + \frac{1}{2}\sum_{i,\ j\in I_{\mathrm{M}},\ i\neq j} \big\langle\phi_{\mathrm{MM}}(r_{ij})\big\rangle_0 + \sum_{i\in I_{\mathrm{H}},\ j\in I_{\mathrm{M}}} x_i\big\langle\phi_{\mathrm{MH}}(r_{ij})\big\rangle_0 \\
&+ \frac{1}{2}\sum_{i,\ j\in I_{\mathrm{H}},\ i\neq j} x_i x_j\big\langle\phi_{\mathrm{HH}}(r_{ij})\big\rangle_0 + \frac{1}{2}\sum_{i\in I_{\mathrm{M}}} F''_{\mathrm{M}}\big(\langle\omega_i\rangle_0\big)\big(C^{(0)}_{\mathrm{MM},i} + 2C^{(0)}_{\mathrm{MH},i} + C^{(0)}_{\mathrm{HH},i} + C_{0,i} + C_{1,i}\big) \\
&+ \frac{1}{2}\sum_{i\in I_{\mathrm{H}}} x_i F''_{\mathrm{H}}\big(\langle\omega_i\rangle_0\big)\big(C^{(0)}_{\mathrm{MM},i} + 2C^{(0)}_{\mathrm{MH},i} + C^{(0)}_{\mathrm{HH},i} + C_{0,i} + C_{1,i}\big).
\end{aligned}
\tag{2.36}
$$

Equation (2.36) does not involve three-body interactions. It is straightforward to prove that its computational complexity, in terms of the number of calls to pair functions, is $\mathcal{O}(QN)$.

Details of the computational complexity analysis are provided in 2.C.

2.3.2 Subcycling time integration

When executing the DMD algorithm, the time-step size (denoted by Δt) is limited by the time-integration of the diffusion equation — an excessively large Δt usually results in a nonphysical x_i, above 1 or below 0, which then fails Algorithm 1 at line 23. However, at each time-step, the computational cost is dominated by the iterative optimization solver, as the objective function is highly nonlinear, and involves nonlocal interactions. The same situation also occurs in other multiphysics problems, where the rate-limiting subsystem is not the most computationally intensive one. The idea of *subcycling* is to regularly skip the solution of the computationally intensive subsystem at a certain frequency, thereby accelerating the computation while retaining an acceptable accuracy. It has been shown to be effective in a number of application domains [24, 25, 26]. Here, we explore the effectiveness of subcycling for DMD simulations.

Algorithm 2 presents a revised DMD pseudocode that adopts subcycling time integration. Evaluating the chemical potential γ_i^{n+1} requires $\{\bar{\boldsymbol{q}}\}^{n+1}$ and $\{\sigma\}^{n+1}$ (line 23 of Algorithm 1), which are computed by the optimization solver. At a time-step that the optimization solver is skipped, an *ad hoc* numerical scheme is needed to determine their values. We consider the following two schemes.

1. *Constant extrapolation*: the values of $\{\bar{\boldsymbol{q}}\}^{n+1}$ and $\{\sigma\}^{n+1}$ are set to the latest solutions

of the optimization solver (line 18 of Algorithm 2).

2. *Linear extrapolation*: $\{\bar{\boldsymbol{q}}\}^{n+1}$ and $\{\sigma\}^{n+1}$ are calculated by linearly extrapolating the last two solutions of the optimization solver (line 20 of Algorithm 2).

Algorithm 2 Solution of the DMD model equations with subcycling time integration.

1: **Input**: $\{x\}^0$ (initial condition), $t_{\max}$ (final time), Δn (subcycling-step size)
2: **Begin**
3: *initialization*
4: same as Algorithm 1.
5: **if** *linear extrapolation* **then**
6: $\bar{\boldsymbol{q}}_i^* \leftarrow \bar{\boldsymbol{q}}_i^0,\ \sigma_i^* \leftarrow \sigma_i^0,\ \forall i \in I_{\mathrm{M}} \cup I_{\mathrm{H}}.$
7: **end if**
8: *time loop*:
9: **while** $t < t_{\max}$ **do**
10: solve Eq. (2.23) for one time-step. (same as Algorithm 1.)
11: **if** $(n+1 \bmod \Delta n) = 0$ **then**
12: **minimize** $\mathcal{F}\big(\{\bar{\boldsymbol{q}}\}, \{\sigma\}, \{x\}^{n+1}\big) \Rightarrow \{\bar{\boldsymbol{q}}\}^{n+1}, \{\sigma\}^{n+1}$. (same as Algorithm 1.)
13: **if** *linear extrapolation* **then**
14: $\mathrm{grad}(\bar{\boldsymbol{q}}_i) \leftarrow \dfrac{\bar{\boldsymbol{q}}_i^{n+1} - \bar{\boldsymbol{q}}_i^*}{\Delta n \Delta t},$
15: $\mathrm{grad}(\sigma_i) \leftarrow \dfrac{\sigma_i^{n+1} - \sigma_i^*}{\Delta n \Delta t},$
16: $\bar{\boldsymbol{q}}_i^* \leftarrow \bar{\boldsymbol{q}}_i^{n+1},\ \ \sigma_i^* \leftarrow \sigma_i^{n+1},\quad \forall i \in I_{\mathrm{M}} \cup I_{\mathrm{H}}$
17: **end if**
18: **else**
19: **if** *constant extrapolation* **then**
20: $\bar{\boldsymbol{q}}_i^{n+1} \leftarrow \bar{\boldsymbol{q}}_i^n,\ \ \sigma_i^{n+1} \leftarrow \sigma_i^n,\quad \forall i \in I_{\mathrm{M}} \cup I_{\mathrm{H}}$
21: **else if** *linear extrapolation* **then**
22: $\bar{\boldsymbol{q}}_i^{n+1} \leftarrow \bar{\boldsymbol{q}}_i^n + \mathrm{grad}(\bar{\boldsymbol{q}}_i)\Delta t,\ \ \sigma_i^{n+1} \leftarrow \sigma_i^n + \mathrm{grad}(\sigma_i)\Delta t,\quad \forall i \in I_{\mathrm{M}} \cup I_{\mathrm{H}}$
23: **end if**
24: **end if**
25: $\gamma_i^{n+1} \leftarrow \dfrac{3}{2} + \log\dfrac{x_i^{n+1}}{1 - x_i^{n+1}} + \dfrac{1}{k_{\mathrm{B}}T}\dfrac{\partial \langle V \rangle_0}{\partial x_i}\bigg|^{n+1},\quad \forall i \in I_{\mathrm{H}}$
26: $t \leftarrow t + \Delta t,\ \ n \leftarrow n+1$
27: **end while**
28: **End**
29: **Output**: $\{\gamma\}^n,\ \{\bar{\boldsymbol{q}}\}^n,\ \{\sigma\}^n,\ \{x\}^n$

Remark 2.

1. *We determine the initial guess for the optimization solver using the same extrapolation method selected for calculating the chemical potential.*

2. *Subcycling does not always reduce the computational cost. For example, one issue hidden behind Algorithm 2 is that as the time interval between successive calls to the optimization solver increases, the number of quasi-Newton iterations required to achieve convergence may increase accordingly. We will assess the performance of subcycling time integration in Sections 2.4.1 and 2.4.2 through a series of numerical experiments.*

2.3.3 Implementation details

In this work, we integrate the diffusion equation using the forward Euler method. We solve the optimization problem using a limited memory BFGS quasi-Newton method [38]. Important details, including the derivation of the gradients $\partial\mathcal{F}/\partial\bar{\boldsymbol{q}}_i$ and $\partial\mathcal{F}/\partial\sigma_i$, and the chemical potential γ_i, are provided in 2.D. Moreover, we parallelize Algorithm 2 with Message Passing Interface (MPI), using the PETSc library [39].

2.4 Numerical experiments

To assess the proposed DMD model and numerical methods, we take the palladium-hydrogen (Pd-H) system as an example, and simulate the diffusion of H atoms in Pd nanoparticles. The Pd-H system has broad impacts in several application areas, including hydrogen storage,

purification filters, isotope separation, and fuel cells [40, 41]. At room temperature, Pd-H exhibits two distinct phases: the dilute α phase with low hydrogen concentration (up to $PdH_{0.015}$), and the β phase with high hydrogen concentration ($PdH_{0.6}$ and above). In both phases, the Pd sublattice maintains the face-centered cubic (FCC) structure, while the H atoms occupy the octahedral interstitial sites. Attendant to the α/β phase transformation, there is a lattice expansion with 10.4% increase in volume [42].

We adopt the EAM potential developed by Zhou and Zimmerman [43], which is capable of capturing the above fundamental features. We examine the proposed DMD model and numerical methods using two different problems: (1) the diffusive transport of a single H atom; and (2) the absorption of H by Pd nanocubes. Problem (1) has a solution that varies smoothly in space and time, while Problem (2) is dominated by the propagation of a sharp phase boundary. The simulations presented in this section are performed on the BlueRidge supercomputer at Virginia Tech [44], using 100 to 500 CPU cores.

2.4.1 Long-term dynamics of a single H atom on Pd lattice

We apply the DMD model to simulate the long-term dynamics of one H atom in a perfect Pd crystal. Specifically, we create a Pd nanocube that contains $30 \times 30 \times 30$ unit cells ($108,000$ Pd sites and $108,000$ octahedral interstitial sites), with the surfaces oriented in [100], [010] and [001] directions (Fig. 2.2). The width of the nanocube is approximately 12 nm. At time $t = 0$, the interstitial site at the center of the cube is occupied by H (i.e., $x = 1$), while

all the other interstitial sites are unoccupied (i.e., $x = 0$). A no-flux boundary condition is applied to the diffusion equation, Eq. (2.23), over the surface of the nanocube. The atomic diffusivity coefficient B_0 is set to 500.0 K/(eV · s) to match the rate of diffusion observed in nanocubes of similar size [20].

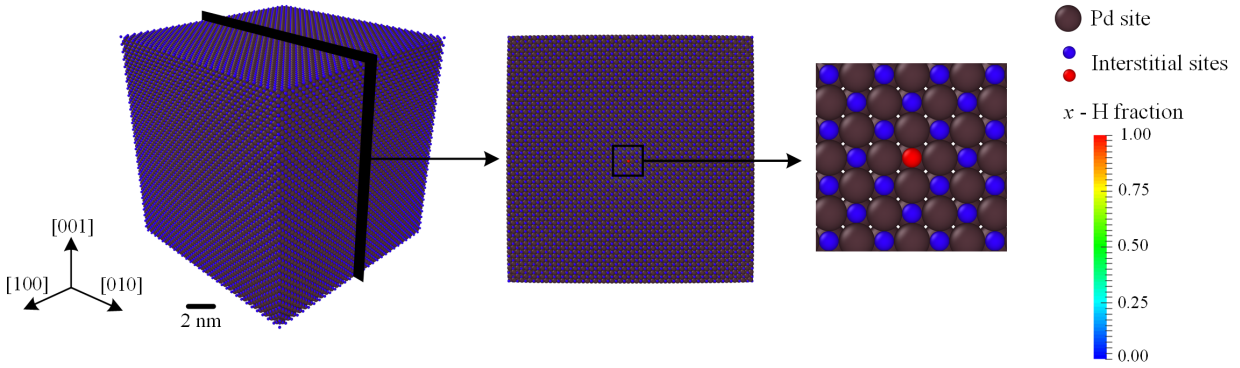

Figure 2.2: Simulation setup of one H atom on Pd lattice.

Model validation

We consider the classical random walk model as a reference. Following this model, the probability of finding the H atom on a given interstitial site — that is, the H fraction x on the site — is the solution of Fick's second law with a Dirac delta initial condition [45]. Specifically, in 3D,

$$x(r,t) = \frac{\Omega}{(4\pi D_{\mathrm{H}} t)^{3/2}} \exp\Big(-\frac{r^2}{4D_{\mathrm{H}} t}\Big), \tag{2.37}$$

where r is the distance from the site in question to the initial position of the H atom. In the expression above, $\Omega = a_{\mathrm{L}}^3/4$ is the atomic volume, where a_{L} denotes the lattice constant. It is notable that Ω is kept as a constant, which reflects the fact that, unlike DMD, the

random walk model neglects the lattice deformation induced by the solute particle. Here, we set $a_{\mathrm{L}} = 3.89$ Å, i.e., the lattice constant of FCC Pd at room temperature and atmospheric pressure [43]. In Eq. (2.37), D_{H} denotes the diffusivity coefficient. Recent experiments have revealed that the value of D_{H} is different in nanosized particles than in bulk Pd [40, 46, 27, 20]. We set $D_{\mathrm{H}} = 0.66$ Å^2/s, again to match the diffusive time scale of the aforementioned nanocube experiments [20].

Figure 2.3 compares the DMD result with the random walk model value for the H fraction on the initially occupied site. The random walk result is obtained by substituting $r = 0$ in Eq. (2.37), which reads as

$$\log x(0,t) = -\frac{3}{2}\log t - \log \frac{\Omega}{(4\pi D_{\mathrm{H}})^{3/2}}. \tag{2.38}$$

The DMD result shown in Fig. 2.3 is obtained using the second-order mean field approximation presented in Section 2.3.1. Furthermore, the relaxed Pd nanocube is used as a reference configuration to calculate the covariances in Eq. (2.35). The temperature is fixed at $T = 300$ K, and the time-step size is set as $\Delta t = 2.0 \times 10^{-3}$ s. Smaller time-step sizes have also been tested, and the differences in the results are negligible. The total number of time-steps is 5×10^5.

Moreover, Fig. 2.3 shows that the DMD result closely matches the random walk solution for $t > 20.0$ s. The discrepancy is larger early in the simulation, which is likely due to the fact that the random walk model neglects the coupling between diffusion and lattice

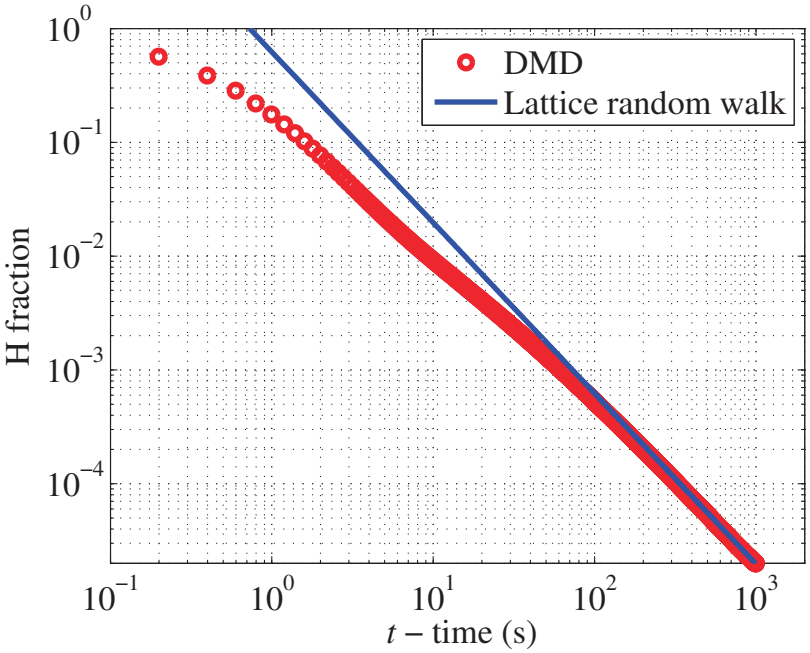

Figure 2.3: Time-history of H fraction on the initially occupied site.

deformation, while DMD accounts for this effect. Nonetheless, both models are probabilistic by nature, and are designed to simulate long-term diffusive behaviors beyond the time scale of microscopic state transitions. Therefore, the agreement shown in Fig. 2.3 is acceptable.

In addition, Fig. 2.4 shows the H fraction predicted by the two models as a function of the distance r, and at four time instances. The profiles predicted by the two models are similar, exhibiting that the H fraction varies smoothly in space. As expected, the discrepancy decreases as time t increases.

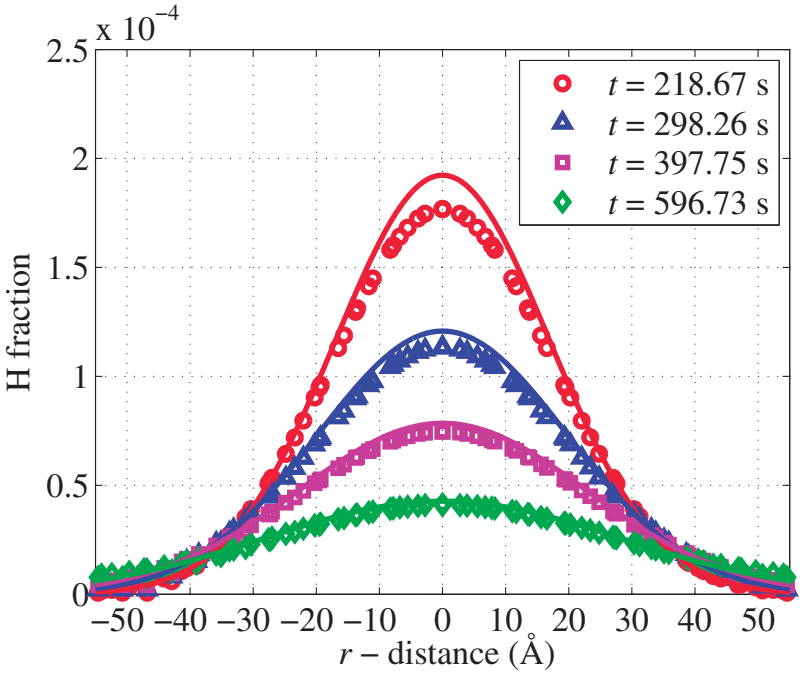

Figure 2.4: Comparison of H fractions on interstitial sites in space. Markers show the DMD results and solid lines show the random walk solutions.

Assessment of numerical methods

In this section, we focus on assessing the accuracy of the first- and second-order mean field approximation methods presented in Section 2.3.1, using the classical MC method as a reference. As already mentioned in the introduction, employing the MC method to simulate the entire process is impractical. Therefore, we limit ourselves to one time-step, specifically, at time $t = 218.67$ s. Figure 2.5 compares the relative error in $\langle F_{\mathrm{Pd}}(\omega_i)\rangle_0$ and $\langle F_{\mathrm{H}}(\omega_i)\rangle_0$ between the first- and second-order mean field approximation methods. Notably, the second-order mean field approximation reduces the numerical error in both $\langle F_{\mathrm{Pd}}(\omega_i)\rangle_0$ and $\langle F_{\mathrm{H}}(\omega_i)\rangle_0$ by a factor of 8. The total CPU time (i.e., the sum of computation time consumed by all the CPU cores) consumed by each method has also been recorded, showing that the cost of

the first- and second-order mean field approximations are nearly the same, and are 3 orders of magnitude lower than the cost of the MC method (with 10^5 samples).

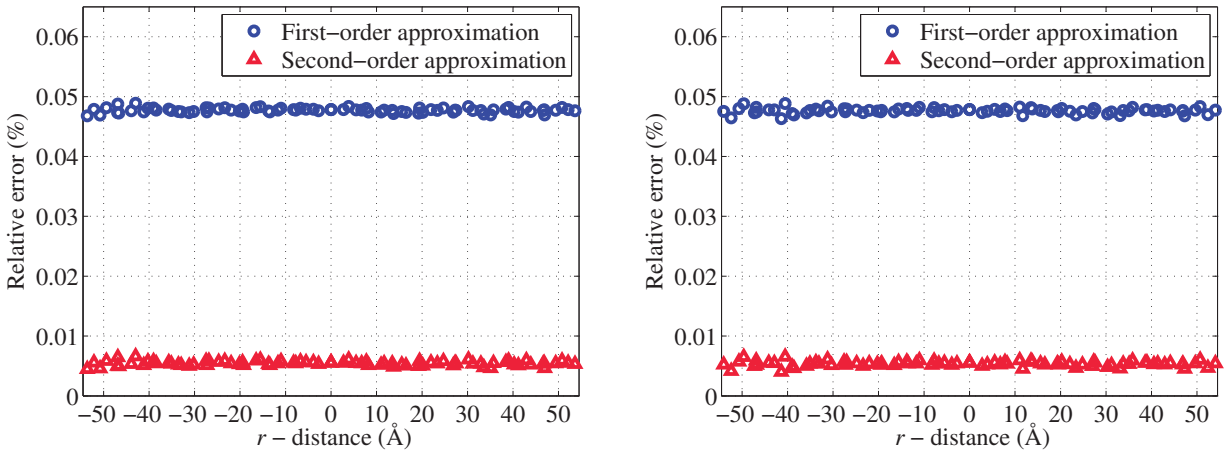

Figure 2.5: Relative error in (a) $\left\langle F_{\mathrm{Pd}}(\omega_i)\right\rangle_0$ and (b) $\left\langle F_{\mathrm{H}}(\omega_i)\right\rangle_0$.

Figure 2.6 shows the effect of subcycling on computational cost, with Δn varied between 1 (no subcycling) and 15. All simulations are terminated after 10^4 time-steps, and the total CPU time is shown in the figure. Clearly, as Δn increases, the total CPU time decreases monotonically. Moreover, with the same Δn, the constant and linear extrapolation methods presented in Section 2.3.2 incur approximately the same cost. In particular, when $\Delta n = 15$, the speed-up is 440%. It is also notable that for this problem, the effect of subcycling on solution accuracy is small. For example, the predicted maximum hydrogen fraction at $t = 2.0$ s varies by less than 0.02% for Δn between 1 and 15.

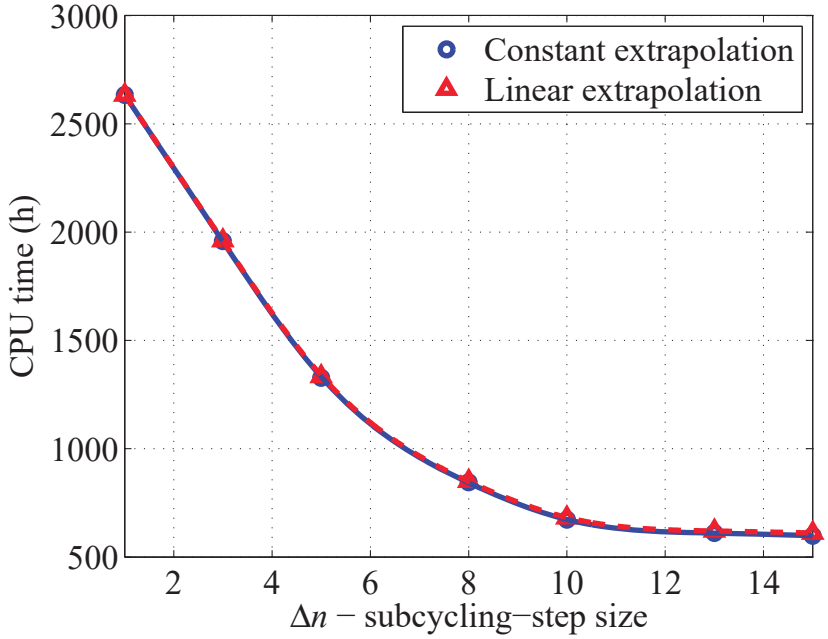

Figure 2.6: Effect of subcycling on the total CPU time.

2.4.2 Absorption of hydrogen by Pd nanocubes

Pd is capable of absorbing a large atomic percentage of hydrogen at room temperature. The process consists of three steps: (1) the dissociation of H_2 molecules into atoms on the surface of Pd; (2) the diffusion of H atoms into subsurface; and (3) the diffusion of H atoms into the interior (octahedral) interstitial sites [47, 40, 48]. Here, we apply the proposed DMD model and numerical methods to simulate Step (3). Recent experimental studies suggest that for Pd nanoparticles, this step can take minutes or longer, and is dominated by the propagation of a sharp α/β hydride phase boundary [49, 20, 27, 50, 51]. Both the large time scale and the nonlinear dynamics make it an interesting example for testing and assessing the capabilities and robustness of our DMD model.

We create a Pd nanocube with $40 \times 40 \times 40$ unit cells (Fig. 2.7), and the edge length is approximately 16 nm. The sample contains $256,000$ Pd atoms and $256,000$ octahedral interstitial sites that can be occupied by H atoms. The surfaces of the nanocube are aligned with [100], [010], and [001] directions. We assume that at time $t = 0$, the surface and subsurface layers are already saturated with H atoms. Therefore, following the theory of Zalineeva *et al.* [48], we fix $x = 1$ within the first, second, and third outermost layers of interstitial sites. The other interstitial sites are initialized with $x = 0$ (Fig. 2.7). As the simulation starts, the atomic chemical potential γ is different on the subsurface and interior interstitial sites, which drives the diffusion of H inwards. The atomic diffusivity coefficient B_0 is set to 500.0 K/(eV $\cdot$ s), same as in Section 2.4.1, whereas the temperature is fixed at $T = 300$ K. The time-step size is $\Delta t = 5.0 \times 10^{-3}$ s, and the total number of time-steps is 8×10^3.

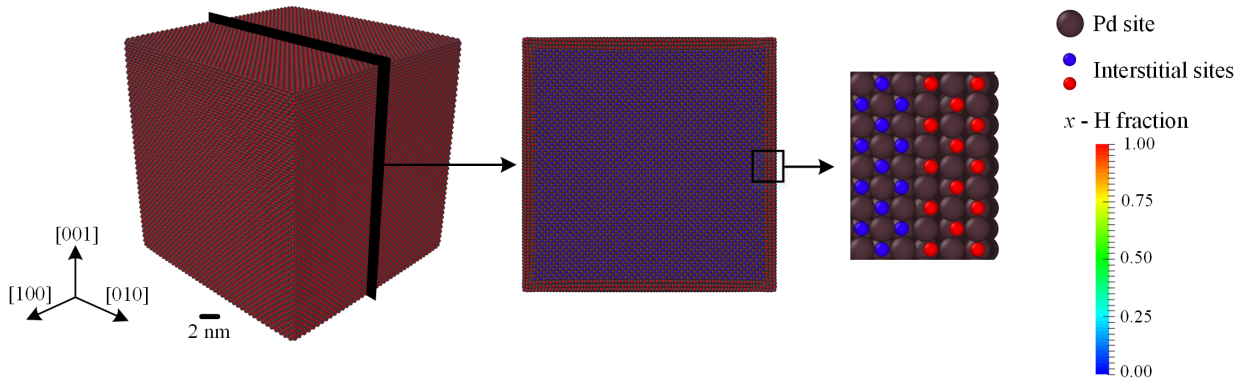

Figure 2.7: Simulation setup of H absorption by a Pd nanocube.

In order to describe the local lattice deformation resulting from the relaxation of the Pd lattice and the movements of H atoms within it, we introduce a local lattice constant a_i on

each Pd site, defined as

$$a_i = \left(\frac{\sqrt{2}}{2} \left|\mathcal{N}_{\mathrm{Pd},i}^{(1)}\right| + \left|\mathcal{N}_{\mathrm{Pd},i}^{(2)}\right| + \frac{\sqrt{6}}{2} \left|\mathcal{N}_{\mathrm{Pd},i}^{(3)}\right| \right)^{-1} \sum_j \left|\bar{\boldsymbol{q}}_i - \bar{\boldsymbol{q}}_j\right|, \quad \forall i \in I_{\mathrm{Pd}},\ j \in \mathcal{N}_{\mathrm{Pd},i}^{(1)} \cup \mathcal{N}_{\mathrm{Pd},i}^{(2)} \cup \mathcal{N}_{\mathrm{Pd},i}^{(3)}, \tag{2.39}$$

where $\mathcal{N}_{\mathrm{Pd},i}^{(k)}$, with $k = 1, 2, 3$, labels the k-th shell of Pd neighbors of site i, and $\left|\mathcal{N}_{\mathrm{Pd},i}^{(k)}\right|$ denotes the cardinality of $\mathcal{N}_{\mathrm{Pd},i}^{(k)}$. The coefficients multiplying them, i.e., $\sqrt{2}/2$, 1, and $\sqrt{6}/2$, stand to recover the uniform lattice constant for an undeformed configuration.

Simulation result

Figure 2.8 visualizes the hydrogen diffusion process predicted by our DMD model. This analysis is performed using the second-order mean field approximation presented in Section 2.3.1 without subcycling. The relaxed Pd nanocube, which is fully saturated with H (i.e., $x_i = 1,\ \forall i \in I_{\mathrm{H}}$), is used as a reference configuration to calculate the covariances in Eq. (2.35). Specifically, at time $t = 8.5$ s, the distribution of H fraction clearly indicates a phase boundary separating an α phase core and a β phase shell. At this point, the phase boundary has taken the shape of a rounded cube. Its thickness varies between 2 and 3 layers of lattice sites from the rounded edges to the faces. From the distribution of lattice constant, it can be seen that in the α phase the lattice constant is about 3.90 Å, and the lattice unit cell, located along one of the cross-section diagonals (shown by the black square on the first row of Fig. 2.8b), maintains the shape of a cube. However, an incipient lattice expansion can be observed near the phase boundary. Notably, the corners of the nanocube stretch

outwards along the body diagonals, forming a star-like shape. This phenomenon has also been observed in experimental studies [27].

Conversely, at time $t = 23.5$ s, H diffuses towards the center of the Pd nanocube, and the phase boundary has already acquired a spherical shape. The thickness of the phase boundary appears to be uniform. The distribution of lattice constant shows that the lattice deformation is most significant near the phase boundary, with a local maximum lattice constant of 4.35 Å. From the zoom-in view, on the second row of Fig. 2.8b, the pre-selected unit cell, which is near the phase boundary at this time instance, undergoes a large shear deformation, characterized by the shape of a rhombohedron.

Finally, at time $t = 31.0$ s, the spherical phase boundary dwindles until H atoms saturate the entire Pd nanocube. At this stage, the unit cell, located far away from the phase boundary, restores its shape to a cube. Overall, the capability of the proposed DMD in capturing the propagation of a sharp phase boundary over a time window of more than 30 s is remarkable.

Assessment of mean field approximation

In this section, we examine the computational accuracy and cost of the first- and second-order mean field approximation methods at time $t = 23.5$ s, when the instantaneous solution exhibits a spherical α/β phase boundary (Fig. 2.8). Figures 2.9 and 2.10 compare the accuracy of the first- and second-order mean field approximation methods for evaluating the mean of embedding energy, i.e., $\left\langle F_{\mathrm{Pd}}(\omega_i)\right\rangle_0$ and $\left\langle F_{\mathrm{H}}(\omega_i)\right\rangle_0$, using the converged MC

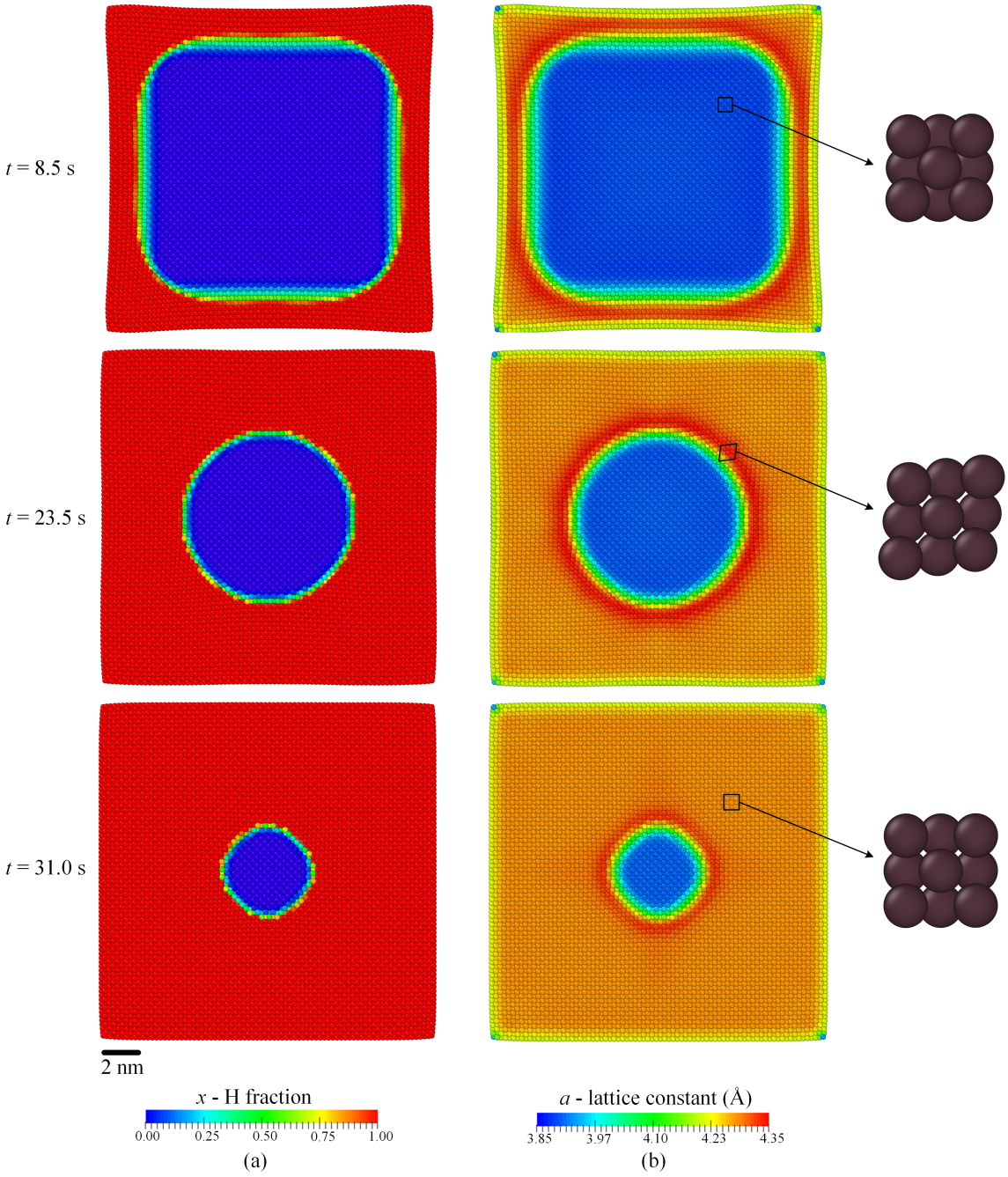

Figure 2.8: Distribution of (a) x_i and (b) a_i on the middle [100] cross-section. The zoom-in views show the deformation of the same unit cell.

solution (with 10^5 samples) as a reference. Specifically, Fig. 2.9 shows the relative error in $\langle F_{\mathrm{H}}(\omega_i)\rangle_0$. Through the first-order approximation method, the numerical error is larger

in the β phase outer shell than in the α phase core. This is likely due to the fact that the higher H fraction in the β phase results in stronger interactions between H-Pd and H-H atom pairs. This leads to a high variance of electron density ω_i in the β phase and hence a large numerical error caused by omitting the second- and higher-order terms on the right-hand-side of Eq. (2.28). Figure 2.9 also shows that, as we expect, the second-order mean field approximation significantly reduces the numerical error. Specifically, the maximum error decreases from 9.46% to 4.35%, and the average error decreases from 4.93% to 0.53%, that is, by nearly a factor of 10.

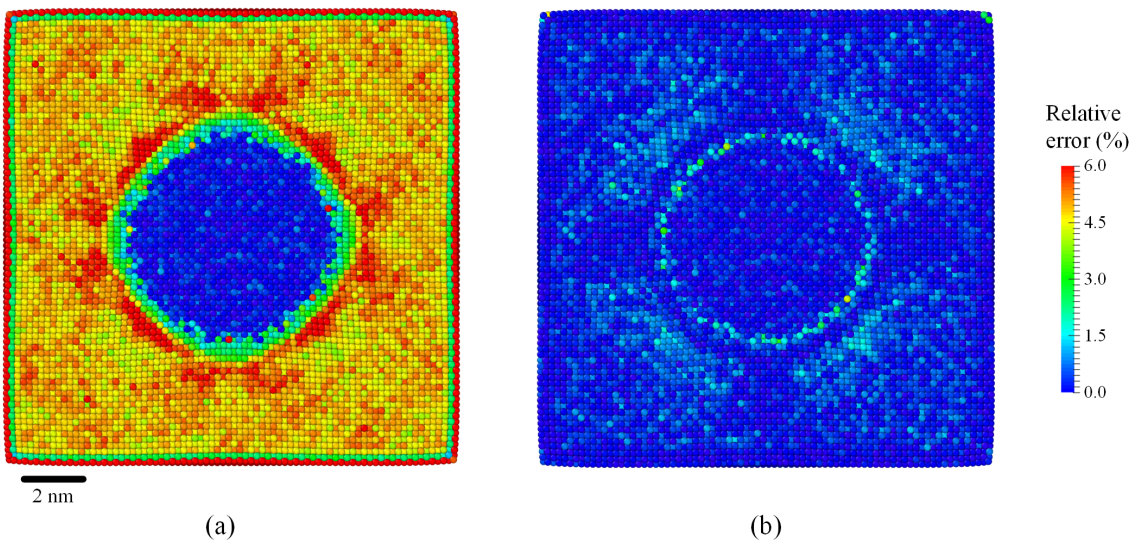

Figure 2.9: Relative error in $\left\langle F_{\mathrm{H}}(\omega_i)\right\rangle_0$ through (a) first- and (b) second-order approximation methods.

Next, Fig. 2.10 shows the relative error in $\left\langle F_{\mathrm{Pd}}(\omega_i)\right\rangle_0$. Again, the second-order mean field approximation is more accurate than the first-order counterpart. Specifically, the maximum error decreases from 0.94% to 0.84%, while the average error decreases from 0.22% to 0.06%. In addition, it is noteworthy that in both cases, the maximum error occurs near the α/β

phase boundary.

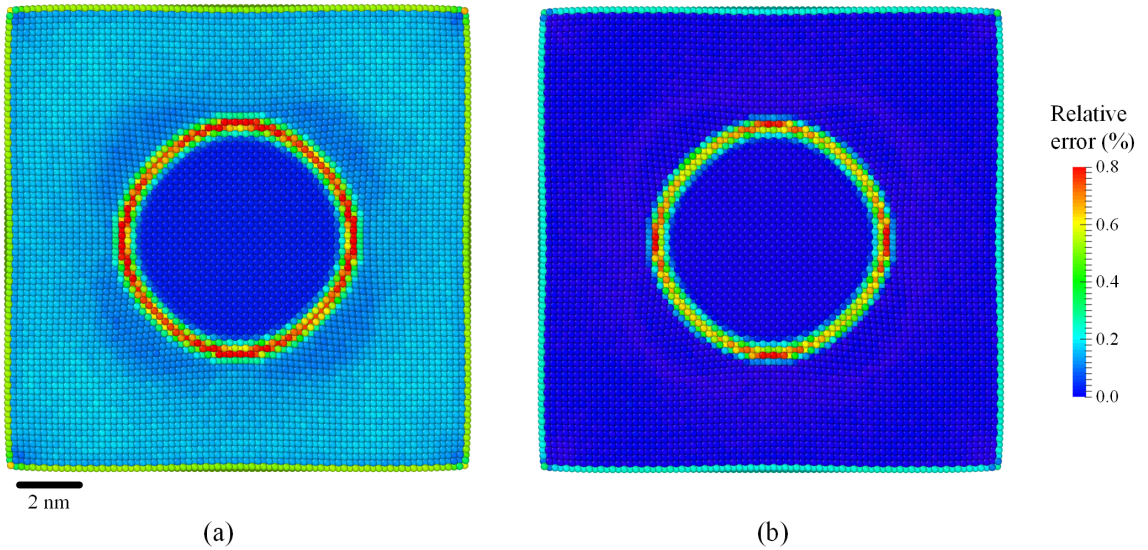

Figure 2.10: Relative error in $\left\langle F_{\mathrm{Pd}}(\omega_i)\right\rangle_0$ through (a) first- and (b) second-order approximation methods.

Figure 2.11 compares the total CPU time consumed by the mean field approximation methods and the MC method. Evidently, the computational cost of the first- and second-order mean field approximations are about the same, which is 3 orders of magnitude lower than that of MC integration (when considering 10^5 samples). Combining Figs. 2.9, 2.10 and2.11 together, it offers evidence of the ability of the second-order mean field approximation to significantly reduce the numerical error while maintaining its low computational cost.

Figure 2.12 compares the average H fraction and lattice constant predicted by the first- and second-order approximation methods. In particular, the first-order method overestimates the speed of H diffusion. The maximum discrepancy between the two methods is 7.27% and 1.34% in the average H faction and the average lattice constant, respectively.

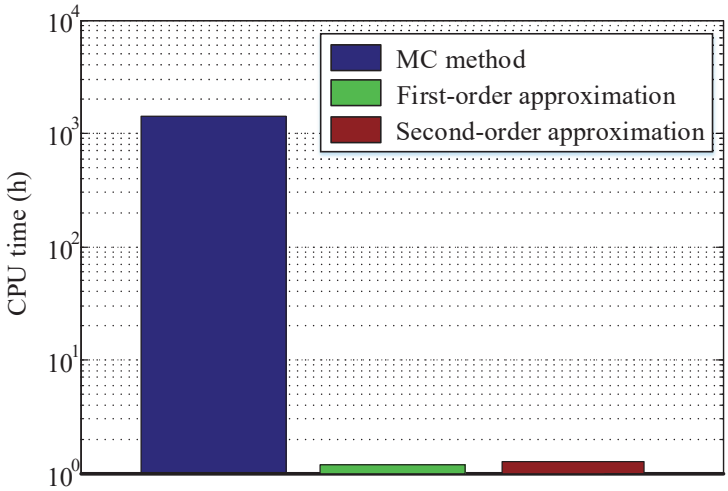

Figure 2.11: Effect of mean field approximation on the total CPU time.

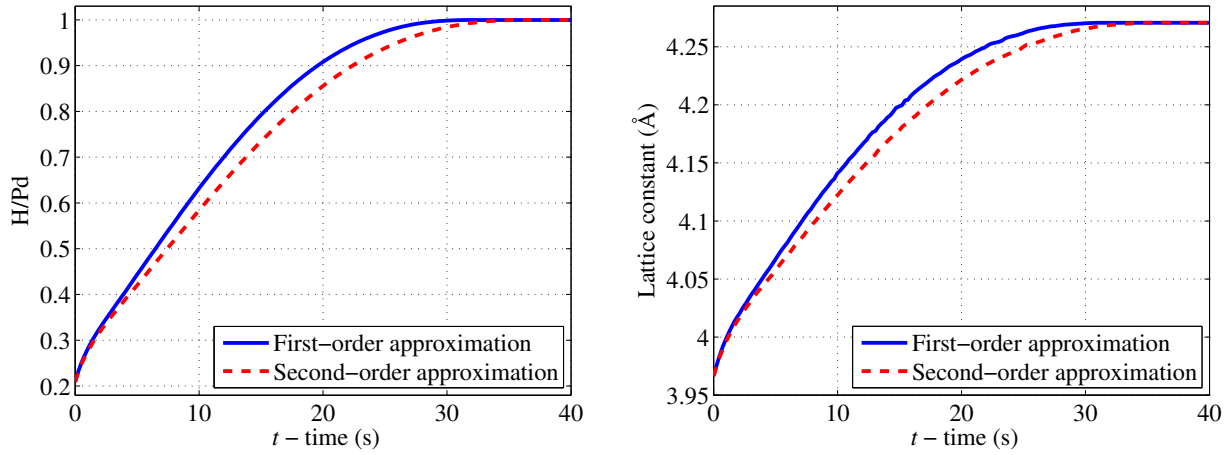

(a) (b)

Figure 2.12: Effect of mean field approximation on the average (a) H fraction and (b) lattice constant of the nanocube.

Assessment of subcycling time integration

The total CPU time consumed by the simulations with different subcycling-step sizes is compared in Fig. 2.13. With either constant or linear extrapolation, the results exhibit a

U-shaped profile. Specifically, as Δn increases, the total CPU time firstly decreases, because Algorithm 2 skips more successive calls of the computationally intensive optimization solver. However, when Δn is greater than 6, the total CPU time increases, because the optimization solver requires more quasi-Newton iterations to achieve convergence. Moreover, with the same Δn, the linear extrapolation shows a lower computational cost than the constant extrapolation, and the difference of the cost between them becomes more obvious when Δn is larger. This is due to the fact that through the linear extrapolation, the initial guess for the optimization solver is closer to the final solution, resulting in fewer quasi-Newton iterations to achieve convergence. In particular, when $\Delta n = 5$, the speed-up is about 254% through the constant extrapolation, while the linear extrapolation with $\Delta n = 8$ provides a speed-up of 647%.

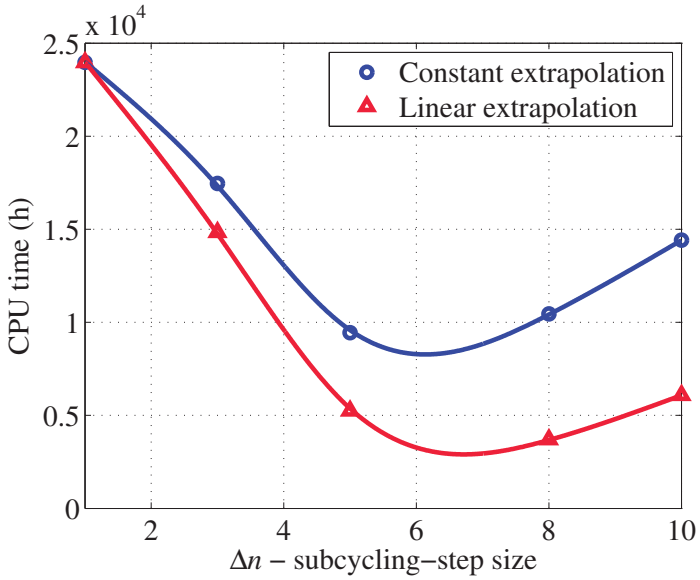

Figure 2.13: Effect of subcycling on the total CPU time.

Figures 2.14 and 2.15 show the effect of subcycling on the solution accuracy, using the

average H fraction and lattice constant as metrics. Specifically, three different values of Δn are tested, namely, 1 (no subcycling), 5 and 8. Overall, the accuracy of the solutions obtained with subcycling is acceptable. The maximum error is 2.67% and 0.24% in the average H fraction and lattice constant, respectively. From the zoom-in views, it can be seen that at one specific time instance (e.g., $t = 22.0$ s), for both schemes of extrapolation the solution accuracy decreases as Δn increases. More specifically, the solutions obtained with subcycling are all lower than the solution with $\Delta n = 1$ (i.e., no subcycling). This can be explained by considering Eq. (2.23) and the boundary conditions specified to the three outermost layers of the material sample. In addition, from the zoom-in views it can also be found that, with the same Δn (e.g., $\Delta n = 5$), the solution through the linear extrapolation is more accurate than that through the constant extrapolation. This is due to the fact that the values of $\{\bar{\boldsymbol{q}}\}$ and $\{\sigma\}$ obtained through the linear extrapolation are closer to their true values. Combining Figs. 2.13, 2.14, 2.15, the ability of subcycling time integration to accelerate the DMD simulation by more than 6 times without significant loss of accuracy is noteworthy.

2.5 Summary and concluding remarks

Diffusive molecular dynamics (DMD) is a novel computational framework that holds promise for predicting long-term diffusive mass transport in crystalline solids at atomistic resolution. It exploits the separation of diffusive and displacive time scales using a probabilistic approach,

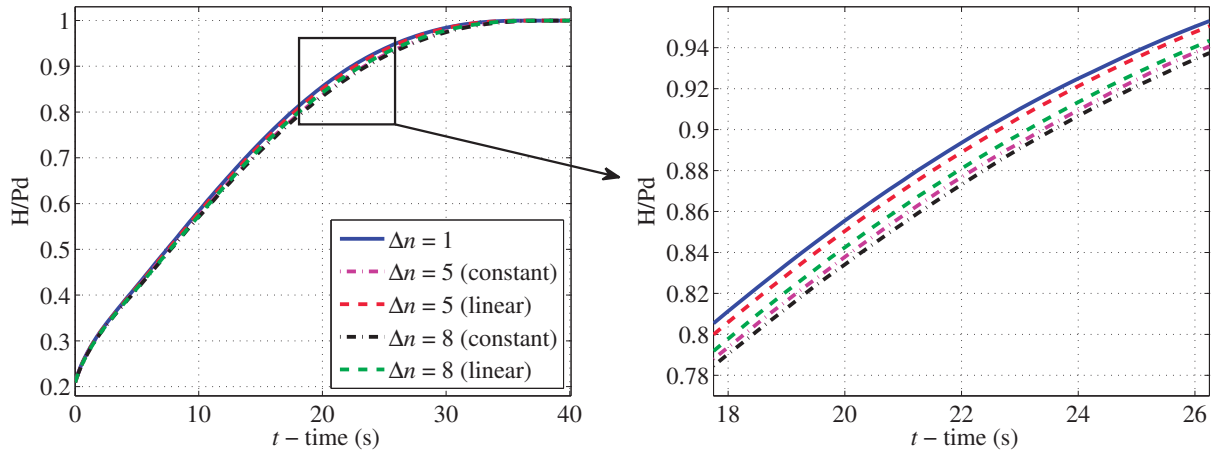

Figure 2.14: Effect of subcycling on the average H fraction of the nanocube.

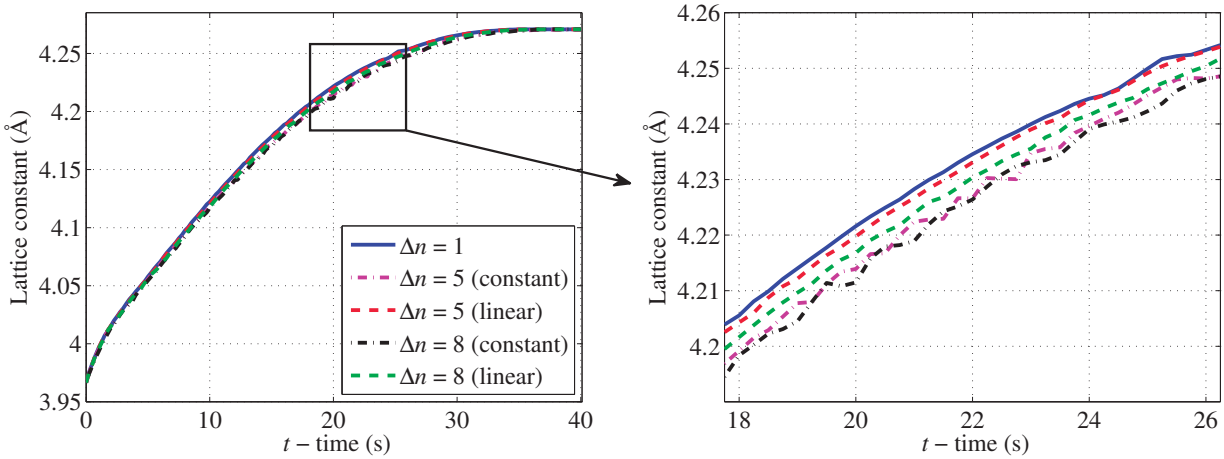

Figure 2.15: Effect of subcycling on the average lattice constant of the nanocube.

thereby alleviating the need to explicitly track individual atom/vacancy hops. As shown in Section 2.4, the time-step size of a DMD simulation can reach 1 ms, making it possible to explore larger time windows beyond the capability of previously established atomistic computational models. However, the computational cost of DMD at each time-step is high,

due to the need to solve a high-dimensional nonlinear optimization problem.

In this paper, we have presented two numerical methods to accelerate DMD simulations without significant loss of accuracy. The first method endeavors to compute the mean of a many-body interatomic potential and its derivatives, which are high-dimensional random variables, using first- or second-order mean field approximations. The first-order version of the method has been applied to DMD in [36, 13, 37], although the term *mean field approximation* was not used therein. In the present work, the second-order extension is introduced in order to improve solution accuracy, without significant increase in computational expense. It utilizes a reference configuration to calculate, off-line, the computationally expensive high-order terms, exploiting the fact that for solid crystals, the displacive atomic movements in a diffusion-dominated process are often small compared to the lattice spacing at equilibrium. The second method, subcycling time integration, consists of regularly skipping the computationally expensive optimization solver while integrating the diffusion equation more frequently in time. At intermediate steps, the optimization solution is estimated simply through constant or linear extrapolation. This idea has been exploited in various multi-physics problems in the past, but applications to DMD had not previously pursued.

We have parallelized the proposed numerical methods using the PETSc library, and applied them to the solution of two problems pertaining to diffusion of hydrogen in palladium. The two problems differ markedly in that the first has a solution that varies smoothly in space and time (Section 2.4.1), whereas the second features an atomically sharp phase boundary (Section 2.4.2). Several findings afforded by the present study are noteworthy. Firstly, for

both problems, the first- and second-order mean field approximation methods reduce the computational cost by three orders of magnitude relative to the cost of direct integration of the interatomic potential using a Monte Carlo method. Secondly, again for both problems, subcycling accelerates time integration by a factor of four or more. Thirdly, the one-step error of the first-order mean field approximation is small for the first problem, specifically, less than 0.05%, but it can exceed 9% for the second problem. In this case, the second-order extension reduces the maximum error by a factor of two, and the average error by a factor of ten.

Beyond these computational developments, we note that the study of hydrogen diffusion in metallic crystals would appear to constitute a novel application of DMD. The ability of DMD to predict the propagation of atomically-sharp phase boundaries over a time window of more than 30 s with full atomistic realism is particularly noteworthy. In closing, we also note that the scope of DMD is not limited to metal hydrides and a broad range of multi-species systems of practical interest suggest themselves as worthwhile foci for future studies.

Acknowledgments

The authors gratefully acknowledge the support of the Institute for Critical Technologies and Applied Sciences (ICTAS) at Virginia Tech through a Junior Faculty Collaboration (JFC) project, the Ministerio de Economía y Competitividad of Spain under grant number DPI2015-66534-R, and the U. S. Army Research Laboratory (ARL) through the Materials

in Extreme Dynamic Environments (MEDE) Collaborative Research Alliance (CRA) under Award Number W911NF-11-R-0001.

Appendix

2.A Derivation of Equation (2.14)

Substituting Eq. (2.13) into Eq. (2.8), we obtain

$$\begin{aligned}\rho_0 = \frac{1}{\Xi_0}\exp\Bigg(&- \sum_{i\in I_{\mathrm{M}}\cup I_{\mathrm{H}}} \frac{1}{2\sigma_i^2}|\boldsymbol{q}_i - \bar{\boldsymbol{q}}_i|^2 - \sum_{i\in I_{\mathrm{M}}} \frac{1}{2k_{\mathrm{B}}Tm_{\mathrm{M}}}|\boldsymbol{p}_i - \bar{\boldsymbol{p}}_i|^2 \\ &- \sum_{i\in I_{\mathrm{H}}}\left(\frac{1}{2k_{\mathrm{B}}Tm_{\mathrm{H}}}|\boldsymbol{p}_i - \bar{\boldsymbol{p}}_i|^2 - n_i(\gamma_i+\gamma_{0i})\right)\Bigg).\end{aligned} \tag{2.40}$$

Enforcing $\langle 1\rangle_0 = 1$, i.e.,

$$\sum_{\{n\}\in\mathcal{O}_{|I_{\mathrm{H}}|}}\left(\frac{1}{2\pi\hbar}\right)^{3(|I_{\mathrm{M}}|+|I_{\mathrm{H}}|)}\int_\Gamma \rho_0 \mathrm{d}q\mathrm{d}p = 1, \tag{2.41}$$

we obtain

$$\begin{aligned}\Xi_0 &= \sum_{\{n\}\in\mathcal{O}_{|I_{\mathrm{H}}|}}\left(\frac{1}{2\pi\hbar}\right)^{3(|I_{\mathrm{M}}|+|I_{\mathrm{H}}|)}\int_\Gamma \mathrm{e}^{-\{\beta\}^{\mathrm{T}}\{h_0\}+\{\gamma\}^{\mathrm{T}}\{n\}}\mathrm{d}q\mathrm{d}p \\ &= \prod_{i\in I_{\mathrm{M}}}\left(\frac{\sigma_i\sqrt{k_{\mathrm{B}}Tm_{\mathrm{M}}}}{\hbar}\right)^3\prod_{i\in I_{\mathrm{H}}}\left(\frac{\sigma_i\sqrt{k_{\mathrm{B}}Tm_{\mathrm{H}}}}{\hbar}\right)^3\left(\mathrm{e}^{\gamma_i+\gamma_{0i}}+1\right),\end{aligned} \tag{2.42}$$

where $|I_{\mathrm{H}}|$ and $|I_{\mathrm{M}}|$ denote the cardinality of I_{H} and I_{M}, respectively. $\mathcal{O}_{|I_{\mathrm{H}}|} = \{0,1\}^{|I_{\mathrm{H}}|}$.

$\Gamma = (\mathbb{R}^3 \times \mathbb{R}^3)^{|I_{\mathrm{M}}+I_{\mathrm{H}}|}$. $\hbar$ is the reduced Planck's constant. Also,

$$\mathrm{d}q\mathrm{d}p = \prod_{i\in I_{\mathrm{M}}\cup I_{\mathrm{H}}} \prod_{k=1}^{3} \mathrm{d}q_{ik}\mathrm{d}p_{ik}. \tag{2.43}$$

Calculating the expected atomic fraction yields

$$\begin{aligned}
x_i \equiv \langle n_i \rangle_0 &= \sum_{\{n\}\in\mathcal{O}_{|I_{\mathrm{H}}|}} \left(\frac{1}{2\pi\hbar}\right)^{3(|I_{\mathrm{M}}|+|I_{\mathrm{H}}|)} \int_{\Gamma} n_i \rho_0 \mathrm{d}q\mathrm{d}p \\
&= \frac{\left(\frac{1}{2\pi\hbar}\right)^{3(|I_{\mathrm{M}}|+|I_{\mathrm{H}}|)} \sum_{\{n\}\in\mathcal{O}_{|I_{\mathrm{H}}|}} n_i \int_{\Gamma} \mathrm{e}^{-\{\beta\}^{\mathrm{T}}\{h_0\}+\{\gamma\}^{\mathrm{T}}\{n\}} \mathrm{d}q\mathrm{d}p}{\prod_{j\in I_{\mathrm{M}}} \left(\frac{\sigma_j\sqrt{k_{\mathrm{B}}Tm_{\mathrm{M}}}}{\hbar}\right)^3 \prod_{j\in I_{\mathrm{H}}} \left(\frac{\sigma_j\sqrt{k_{\mathrm{B}}Tm_{\mathrm{H}}}}{\hbar}\right)^3 \left(\mathrm{e}^{\gamma_j+\gamma_{0j}}+1\right)} \\
&= \frac{\left(\frac{1}{2\pi}\right)^{3(|I_{\mathrm{M}}|+|I_{\mathrm{H}}|)} \mathrm{e}^{\gamma_i+\gamma_{0i}} \prod_{j\in I_{\mathrm{H}},\ j\neq i} \left(\mathrm{e}^{\gamma_j+\gamma_{0j}}+1\right) \prod_{j\in I_{\mathrm{M}}} \left(2\pi\sigma_j\sqrt{k_{\mathrm{B}}Tm_{\mathrm{M}}}\right)^3 \prod_{j\in I_{\mathrm{H}}} \left(2\pi\sigma_j\sqrt{k_{\mathrm{B}}Tm_{\mathrm{H}}}\right)^3}{\prod_{j\in I_{\mathrm{M}}} \left(\sigma_j\sqrt{k_{\mathrm{B}}Tm_{\mathrm{M}}}\right)^3 \prod_{j\in I_{\mathrm{H}}} \left(\sigma_j\sqrt{k_{\mathrm{B}}Tm_{\mathrm{H}}}\right)^3 \left(\mathrm{e}^{\gamma_j+\gamma_{0j}}+1\right)} \\
&= \frac{\mathrm{e}^{\gamma_i+\gamma_{0i}}}{\mathrm{e}^{\gamma_i+\gamma_{0i}}+1}.
\end{aligned} \tag{2.44}$$

A straightforward manipulation gives

$$\gamma_i = \log\frac{x_i}{1-x_i} - \gamma_{0i}, \tag{2.45}$$

which is Eq. (2.14).

2.B Complexity of computing phase averages using Gaussian quadratures on a sparse grid

In this section, the complexity of computing Eq. (2.26) is discussed. Clearly, the first two terms on the right-hand-side of Eq. (2.26) dominate the computational cost, as they involve high-dimensional integration. By means of Gaussian quadratures, the first term is computed as follows

$$\begin{aligned}\sum_{i\in I_{\mathrm{M}}}\left\langle F_{\mathrm{M}}(\omega_i)\right\rangle_0 &\approx \sum_{i\in I_{\mathrm{M}}}\sum_{k=1}^{k_{\max}} F_{\mathrm{M}}(\omega_{i,k})W_k \\ &= \sum_{i\in I_{\mathrm{M}}}\sum_{k=1}^{k_{\max}} F_{\mathrm{M}}\Big(\sum_{\substack{j\in I_{\mathrm{M}}\cap\mathcal{B}_i(r_{\mathrm{c}}),\\ j\neq i}} f_{\mathrm{M}}(r_{ij,k}) + \sum_{\substack{j\in I_{\mathrm{H}}\cap\mathcal{B}_i(r_{\mathrm{c}}),\\ j\neq i}} x_j f_{\mathrm{H}}(r_{ij,k})\Big)W_k,\end{aligned} \tag{2.46}$$

where $\mathcal{B}_i(r)$ denotes the set of atomic sites within a distance r of site i, and r_{c} is the cut-off distance of the EAM potential. The subscript "k" on ω and r refers to the k-th Gaussian point, whereas W_k is the weight of the k-th point. $k_{\max}$ denotes the total number of Gaussian points on a pre-defined sparse grid, which is at least $2n$ for n-dimensional integration. For Eq. (2.46), we have

$$\Big|\big(I_{\mathrm{M}}\cap\mathcal{B}_i(r_{\mathrm{c}})\big)\cup\big(I_{\mathrm{H}}\cap\mathcal{B}_i(r_{\mathrm{c}})\big)\Big| = \Big|\big(I_{\mathrm{M}}\cup I_{\mathrm{H}}\big)\cap\mathcal{B}_i(r_{\mathrm{c}})\Big| = Q+1, \tag{2.47}$$

and

$$k_{\max}\geq 6(Q+1). \tag{2.48}$$

The above derivation also applies to the second term on the right-hand-side of Eq. (2.26), i.e., $\sum_{i\in I_{\mathrm{H}}} x_i \big\langle F_{\mathrm{H}}(\omega_i)\big\rangle_0$. Therefore, computing Eq. (2.26) using Gaussian quadratures on a sparse grid requires at least $\mathcal{O}(Q^2N)$ calls of pair functions, where N is the total number of base and interstitial sites in the material sample.

2.C Complexity of computing phase averages using Gaussian quadratures with mean field approximation

By the first-order mean field approximation, the first term on the right-hand-side of Eq. (2.26) is given by

$$\begin{aligned}\sum_{i\in I_{\mathrm{M}}} \big\langle F_{\mathrm{M}}(\omega_i)\big\rangle_0 &\approx \sum_{i\in I_{\mathrm{M}}} F_{\mathrm{M}}\big(\langle\omega_i\rangle_0\big)\\ &\approx \sum_{i\in I_{\mathrm{M}}} F_{\mathrm{M}}\Big(\sum_{\substack{j\in I_{\mathrm{M}}\cap\mathcal{B}_i(r_{\mathrm{c}}),\\ j\neq i}} \sum_{k=1}^{k_{\max}} f_{\mathrm{M}}(r_{ij,k})W_k + \sum_{\substack{j\in I_{\mathrm{H}}\cap\mathcal{B}_i(r_{\mathrm{c}}),\\ j\neq i}} x_j \sum_{k=1}^{k_{\max}} f_{\mathrm{H}}(r_{ij,k})W_k\Big),\end{aligned} \tag{2.49}$$

where Eq. (2.47) is also satisfied. Here, $k_{\max}$ is independent of Q and N, since the Gaussian quadratures are performed with respect to 6-dimensional integration. The above derivation also applies to the term $\sum_{i\in I_{\mathrm{H}}} x_i \big\langle F_{\mathrm{H}}(\omega_i)\big\rangle_0$. Therefore, computing Eq. (2.26) with the first-order mean field approximation involves $\mathcal{O}(QN)$ calls of pair functions.

When using the second-order mean field approximation, the first term on the right-hand-side

of Eq. (2.26) is given by

$$\sum_{i\in I_{\rm M}}\big\langle F_{\rm M}(\omega_i)\big\rangle_0 \approx \sum_{i\in I_{\rm M}} F_{\rm M}\big(\langle\omega_i\rangle_0\big) + \frac{1}{2}\sum_{i\in I_{\rm M}} F''_{\rm M}\big(\langle\omega_i\rangle_0\big)\big(C^{(0)}_{{\rm MM},i} + 2C^{(0)}_{{\rm MH},i} + C^{(0)}_{{\rm HH},i} + C_{0,i} + C_{1,i}\big). \tag{2.50}$$

The complexity of computing the first-order term $\sum\limits_{i\in I_{\rm M}} F_{\rm M}\big(\langle\omega_i\rangle_0\big)$ has been discussed above. The second-order term of Eq. (2.50) is

$$\begin{aligned}
&\frac{1}{2}\sum_{i\in I_{\rm M}} F''_{\rm M}\big(\langle\omega_i\rangle_0\big)\big(C^{(0)}_{{\rm MM},i} + 2C^{(0)}_{{\rm MH},i} + C^{(0)}_{{\rm HH},i} + C_{0,i} + C_{1,i}\big)\\
\approx&\frac{1}{2}\sum_{i\in I_{\rm M}} F''_{\rm M}\Big(\sum_{\substack{j\in I_{\rm M}\cap\mathcal{B}_i(r_{\rm c}),\\ j\neq i}}\sum_{k=1}^{k_{\max}} f_{\rm M}(r_{ij,k})W_k + \sum_{\substack{j\in I_{\rm H}\cap\mathcal{B}_i(r_{\rm c}),\\ j\neq i}} x_j\sum_{k=1}^{k_{\max}} f_{\rm H}(r_{ij,k})W_k\Big)\\
&\Bigg(C^{(0)}_{{\rm MM},i} + 2C^{(0)}_{{\rm MH},i} + C^{(0)}_{{\rm HH},i} + \sum_{\substack{j\in I_{\rm M}\cap\mathcal{B}_i(r_{\rm c}),\\ j\neq i}}\Big(\sum_{k=1}^{k_{\max}} f^2_{\rm M}(r_{ij,k})W_k - \big(\sum_{k=1}^{k_{\max}} f_{\rm M}(r_{ij,k})W_k\big)^2\Big)\\
&+\sum_{\substack{j\in I_{\rm H}\cap\mathcal{B}_i(r_{\rm c}),\\ j\neq i}}\Big(x_j\sum_{k=1}^{k_{\max}} f^2_{\rm H}(r_{ij,k})W_k - x_j^2\big(\sum_{k=1}^{k_{\max}} f_{\rm H}(r_{ij,k})W_k\big)^2\Big)\Bigg),
\end{aligned} \tag{2.51}$$

where $C^{(0)}_{{\rm MM},i}$, $C^{(0)}_{{\rm MH},i}$, and $C^{(0)}_{{\rm HH},i}$ are defined in Eq. (2.35). The on-the-fly computational cost of $C^{(0)}_{{\rm MM},i}$, $C^{(0)}_{{\rm MH},i}$ and $C^{(0)}_{{\rm HH},i}$ is low because the covariances in them are calculated off-line for a reference equilibrium state — exploiting the fact that for solid crystals, the displacive atomic movements in a diffusion-dominated process are often small compared to the lattice spacing at equilibrium. For Eq. (2.51), Eq. (2.47) is satisfied, and similarly, $k_{\max}$ is independent of Q and N. The above derivation also works for $\sum\limits_{i\in I_{\rm H}} x_i\big\langle F_{\rm H}(\omega_i)\big\rangle_0$. Therefore, computing Eq. (2.26) with the second-order mean field approximation requires $\mathcal{O}(QN)$ calls of pair functions.

2.D Some implementation details

Solving the optimization problem formulated in Eq. (2.22) requires calculating the gradients of the objective function with respect to the state variables $\{\bar{\boldsymbol{q}}\}$ and $\{\sigma\}$. Solving the integration problem formulated in Eq. (2.23) requires calculating the chemical potential $\{\gamma\}$. In this section, we derive $\partial\mathcal{F}/\partial\bar{\boldsymbol{q}}_i$, $\partial\mathcal{F}/\partial\sigma_i$ and γ_i as functions of $\{\bar{\boldsymbol{q}}\}$ and $\{\sigma\}$, using the second-order mean field approximation formulated in Eq. (2.36).

1. $\partial\mathcal{F}/\partial\bar{\boldsymbol{q}}_i$ is given by

$$\begin{aligned}\frac{\partial\mathcal{F}}{\partial\bar{\boldsymbol{q}}_i} = \frac{1}{T}\Bigg(&\frac{\partial F_{\mathrm{M}}\big(\langle\omega_i\rangle_0\big)}{\partial\bar{\boldsymbol{q}}_i} + \frac{1}{2}\frac{\partial F''_{\mathrm{M}}\big(\langle\omega_i\rangle_0\big)}{\partial\bar{\boldsymbol{q}}_i}C_i + \frac{1}{2}F''_{\mathrm{M}}\big(\langle\omega_i\rangle_0\big)\frac{\partial C_i}{\partial\bar{\boldsymbol{q}}_i} + \sum_{j\in I_{\mathrm{M}},\ j\neq i}\Big(\frac{\partial F_{\mathrm{M}}\big(\langle\omega_j\rangle_0\big)}{\partial\bar{\boldsymbol{q}}_i}\\ &+ \frac{\partial\big\langle\phi_{\mathrm{MM}}(r_{ij})\big\rangle_0}{\partial\bar{\boldsymbol{q}}_i} + \frac{1}{2}\frac{\partial F''_{\mathrm{M}}\big(\langle\omega_j\rangle_0\big)}{\partial\bar{\boldsymbol{q}}_i}C_j + \frac{1}{2}F''_{\mathrm{M}}\big(\langle\omega_j\rangle_0\big)\frac{\partial C_j}{\partial\bar{\boldsymbol{q}}_i}\Big) + \sum_{j\in I_{\mathrm{H}}}x_j\Big(\frac{\partial F_{\mathrm{H}}\big(\langle\omega_j\rangle_0\big)}{\partial\bar{\boldsymbol{q}}_i}\\ &+ \frac{\partial\big\langle\phi_{\mathrm{MH}}(r_{ij})\big\rangle_0}{\partial\bar{\boldsymbol{q}}_i} + \frac{1}{2}\frac{\partial F''_{\mathrm{H}}\big(\langle\omega_j\rangle_0\big)}{\partial\bar{\boldsymbol{q}}_i}C_j + \frac{1}{2}F''_{\mathrm{H}}\big(\langle\omega_j\rangle_0\big)\frac{\partial C_j}{\partial\bar{\boldsymbol{q}}_i}\Big)\Bigg), \quad \forall i\in I_{\mathrm{M}},\end{aligned} \tag{2.52}$$

and

$$\begin{aligned}\frac{\partial\mathcal{F}}{\partial\bar{\boldsymbol{q}}_i} = \frac{x_i}{T}\Bigg(&\frac{\partial F_{\mathrm{H}}\big(\langle\omega_i\rangle_0\big)}{\partial\bar{\boldsymbol{q}}_i} + \frac{1}{2}\frac{\partial F''_{\mathrm{H}}\big(\langle\omega_i\rangle_0\big)}{\partial\bar{\boldsymbol{q}}_i}C_i + \frac{1}{2}F''_{\mathrm{H}}\big(\langle\omega_i\rangle_0\big)\frac{\partial C_i}{\partial\bar{\boldsymbol{q}}_i} + \sum_{j\in I_{\mathrm{M}}}\Big(\frac{\partial F_{\mathrm{M}}\big(\langle\omega_j\rangle_0\big)}{\partial\bar{\boldsymbol{q}}_i}\\ &+ \frac{\partial\big\langle\phi_{\mathrm{MH}}(r_{ij})\big\rangle_0}{\partial\bar{\boldsymbol{q}}_i} + \frac{1}{2}\frac{\partial F''_{\mathrm{M}}\big(\langle\omega_j\rangle_0\big)}{\partial\bar{\boldsymbol{q}}_i}C_j + \frac{1}{2}F''_{\mathrm{M}}\big(\langle\omega_j\rangle_0\big)\frac{\partial C_j}{\partial\bar{\boldsymbol{q}}_i}\Big) + \sum_{j\in I_{\mathrm{H}},\ j\neq i}x_j\Big(\frac{\partial F_{\mathrm{H}}\big(\langle\omega_j\rangle_0\big)}{\partial\bar{\boldsymbol{q}}_i}\\ &+ \frac{\partial\big\langle\phi_{\mathrm{HH}}(r_{ij})\big\rangle_0}{\partial\bar{\boldsymbol{q}}_i} + \frac{1}{2}\frac{\partial F''_{\mathrm{H}}\big(\langle\omega_j\rangle_0\big)}{\partial\bar{\boldsymbol{q}}_i}C_j + \frac{1}{2}F''_{\mathrm{H}}\big(\langle\omega_j\rangle_0\big)\frac{\partial C_j}{\partial\bar{\boldsymbol{q}}_i}\Big)\Bigg), \quad \forall i\in I_{\mathrm{H}},\end{aligned} \tag{2.53}$$

where the gradients of F and F'' — collectively represented by G — are given by

$$\begin{aligned}
\frac{\partial G\big(\langle\omega_i\rangle_0\big)}{\partial\bar{\boldsymbol{q}}_i} &= G'\big(\langle\omega_i\rangle_0\big)\Big(\sum_{j\in I_{\mathrm{M}},\ j\neq i}\frac{\partial\big\langle f_{\mathrm{M}}(r_{ij})\big\rangle_0}{\partial\bar{\boldsymbol{q}}_i}+\sum_{j\in I_{\mathrm{H}},\ j\neq i}x_j\frac{\partial\big\langle f_{\mathrm{H}}(r_{ij})\big\rangle_0}{\partial\bar{\boldsymbol{q}}_i}\Big),\quad \forall i\in I_{\mathrm{M}}\cup I_{\mathrm{H}},\\
\frac{\partial G\big(\langle\omega_j\rangle_0\big)}{\partial\bar{\boldsymbol{q}}_i} &= G'\big(\langle\omega_j\rangle_0\big)\frac{\partial\big\langle f_{\mathrm{M}}(r_{ij})\big\rangle_0}{\partial\bar{\boldsymbol{q}}_i},\quad \forall i\in I_{\mathrm{M}},\ \forall j\in I_{\mathrm{M}}\cup I_{\mathrm{H}},\ j\neq i,\\
\frac{\partial G\big(\langle\omega_j\rangle_0\big)}{\partial\bar{\boldsymbol{q}}_i} &= x_iG'\big(\langle\omega_j\rangle_0\big)\frac{\partial\big\langle f_{\mathrm{H}}(r_{ij})\big\rangle_0}{\partial\bar{\boldsymbol{q}}_i},\quad \forall i\in I_{\mathrm{H}},\ \forall j\in I_{\mathrm{M}}\cup I_{\mathrm{H}},\ j\neq i,
\end{aligned}\tag{2.54}$$

and

$$\begin{aligned}
C_i &= C^{(0)}_{\mathrm{MM},i}+2C^{(0)}_{\mathrm{MH},i}+C^{(0)}_{\mathrm{HH},i}+C_{0,i}+C_{1,i},\quad \forall i\in I_{\mathrm{M}}\cup I_{\mathrm{H}},\\
\frac{\partial C_i}{\partial\bar{\boldsymbol{q}}_i} &= \sum_{j\in I_{\mathrm{M}},\ j\neq i}\Big(\frac{\partial\big\langle f^2_{\mathrm{M}}(r_{ij})\big\rangle_0}{\partial\bar{\boldsymbol{q}}_i}+2\langle f_{\mathrm{M}}(r_{ij})\big\rangle_0\frac{\partial\big\langle f_{\mathrm{M}}(r_{ij})\big\rangle_0}{\partial\bar{\boldsymbol{q}}_i}\Big)\\
&\quad+\sum_{j\in I_{\mathrm{H}},\ j\neq i}\Big(x_j\frac{\partial\big\langle f^2_{\mathrm{H}}(r_{ij})\big\rangle_0}{\partial\bar{\boldsymbol{q}}_i}+2x_j^2\langle f_{\mathrm{H}}(r_{ij})\big\rangle_0\frac{\partial\big\langle f_{\mathrm{H}}(r_{ij})\big\rangle_0}{\partial\bar{\boldsymbol{q}}_i}\Big),\quad \forall i\in I_{\mathrm{M}}\cup I_{\mathrm{H}},\\
\frac{\partial C_j}{\partial\bar{\boldsymbol{q}}_i} &= \frac{\partial\big\langle f^2_{\mathrm{M}}(r_{ij})\big\rangle_0}{\partial\bar{\boldsymbol{q}}_i}+2\langle f_{\mathrm{M}}(r_{ij})\big\rangle_0\frac{\partial\big\langle f_{\mathrm{M}}(r_{ij})\big\rangle_0}{\partial\bar{\boldsymbol{q}}_i},\quad \forall i\in I_{\mathrm{M}},\ \forall j\in I_{\mathrm{M}}\cup I_{\mathrm{H}},\ j\neq i,\\
\frac{\partial C_j}{\partial\bar{\boldsymbol{q}}_i} &= x_j\frac{\partial\big\langle f^2_{\mathrm{H}}(r_{ij})\big\rangle_0}{\partial\bar{\boldsymbol{q}}_i}+2x_j^2\langle f_{\mathrm{H}}(r_{ij})\big\rangle_0\frac{\partial\big\langle f_{\mathrm{H}}(r_{ij})\big\rangle_0}{\partial\bar{\boldsymbol{q}}_i},\quad \forall i\in I_{\mathrm{H}},\ \forall j\in I_{\mathrm{M}}\cup I_{\mathrm{H}},\ j\neq i.
\end{aligned}\tag{2.55}$$

$\langle\omega_i\rangle_0$ is calculated using Eq. (2.31). From Eqs. (2.31), (2.54) and (2.55), it can be seen that evaluating $\partial\mathcal{F}/\partial\bar{\boldsymbol{q}}_i$ requires calculating the mean of pair functions f, ϕ, and f^2 and their gradients. Through a change of variables with respect to atomic positions

$$\boldsymbol{q}_i=\bar{\boldsymbol{q}}_i+\sqrt{2}\sigma_i\boldsymbol{s}_i,\tag{2.56}$$

where $\{\boldsymbol{s}\}$ is a set of normally distributed variables, the integration involved in the

calculation of mean is performed with respect to $\{\boldsymbol{s}\}$. Then, by Gaussian quadratures, $\langle f\rangle_0$, $\langle\phi\rangle_0$, $\langle f^2\rangle_0$ — collectively represented by $\langle g\rangle_0$ — and $\partial\langle g\rangle_0/\partial\bar{\boldsymbol{q}}_i$ are given by

$$\begin{aligned}\big\langle g(r_{ij})\big\rangle_0 &= \sum_{k=1}^{k_{\max}} g(r_{ij,k})W_k,\\ \frac{\partial\big\langle g(r_{ij})\big\rangle_0}{\partial\bar{\boldsymbol{q}}_i} &= \sum_{k=1}^{k_{\max}} g'(r_{ij,k})\frac{\boldsymbol{r}_{ij,k}}{r_{ij,k}}W_k,\end{aligned} \tag{2.57}$$

where

$$\boldsymbol{r}_{ij,k} = \sqrt{2}\sigma_i\boldsymbol{s}_{i,k} - \sqrt{2}\sigma_j\boldsymbol{s}_{j,k} + \bar{\boldsymbol{q}}_i - \bar{\boldsymbol{q}}_j, \tag{2.58}$$

with $r_{ij,k} = |\boldsymbol{r}_{ij,k}|$. Here, $\boldsymbol{s}_{i,k}$ is the value of $\boldsymbol{s}_i$ at the k-th Gaussian point. Notably, $\langle g\rangle_0$ and $\partial\langle g\rangle_0/\partial\bar{\boldsymbol{q}}_i$ in Eq. (2.57), and hence $\partial\mathcal{F}/\partial\bar{\boldsymbol{q}}_i$, are functions of $\{\bar{\boldsymbol{q}}\}$ and $\{\sigma\}$.

2. $\partial\mathcal{F}/\partial\sigma_i$ is given by

$$\begin{aligned}\frac{\partial\mathcal{F}}{\partial\sigma_i} = \frac{1}{T}\Bigg(&\frac{\partial F_{\mathrm{M}}\big(\langle\omega_i\rangle_0\big)}{\partial\sigma_i} + \frac{1}{2}\frac{\partial F''_{\mathrm{M}}\big(\langle\omega_i\rangle_0\big)}{\partial\sigma_i}C_i + \frac{1}{2}F''_{\mathrm{M}}\big(\langle\omega_i\rangle_0\big)\frac{\partial C_i}{\partial\sigma_i} + \sum_{j\in I_{\mathrm{M}},\ j\neq i}\Big(\frac{\partial F_{\mathrm{M}}\big(\langle\omega_j\rangle_0\big)}{\partial\sigma_i}\\ &+ \frac{\partial\big\langle\phi_{\mathrm{MM}}(r_{ij})\big\rangle_0}{\partial\sigma_i} + \frac{1}{2}\frac{\partial F''_{\mathrm{M}}\big(\langle\omega_j\rangle_0\big)}{\partial\sigma_i}C_j + \frac{1}{2}F''_{\mathrm{M}}\big(\langle\omega_j\rangle_0\big)\frac{\partial C_j}{\partial\sigma_i}\Big) + \sum_{j\in I_{\mathrm{H}}}x_j\Big(\frac{\partial F_{\mathrm{H}}\big(\langle\omega_j\rangle_0\big)}{\partial\sigma_i}\\ &+ \frac{\partial\big\langle\phi_{\mathrm{MH}}(r_{ij})\big\rangle_0}{\partial\sigma_i} + \frac{1}{2}\frac{\partial F''_{\mathrm{H}}\big(\langle\omega_j\rangle_0\big)}{\partial\sigma_i}C_j + \frac{1}{2}F''_{\mathrm{H}}\big(\langle\omega_j\rangle_0\big)\frac{\partial C_j}{\partial\sigma_i}\Big)\Bigg) - \frac{3k_{\mathrm{B}}}{\sigma_i}, \quad \forall i\in I_{\mathrm{M}},\end{aligned} \tag{2.59}$$

and

$$\frac{\partial\mathcal{F}}{\partial\sigma_i}=\frac{x_i}{T}\Big(\frac{\partial F_{\rm H}\big(\langle\omega_i\rangle_0\big)}{\partial\sigma_i}+\frac{1}{2}\frac{\partial F''_{\rm H}\big(\langle\omega_i\rangle_0\big)}{\partial\sigma_i}C_i+\frac{1}{2}F''_{\rm H}\big(\langle\omega_i\rangle_0\big)\frac{\partial C_i}{\partial\sigma_i}+\sum_{j\in I_{\rm M}}\Big(\frac{\partial F_{\rm M}\big(\langle\omega_j\rangle_0\big)}{\partial\sigma_i}$$
$$+\frac{\partial\big\langle\phi_{\rm MH}(r_{ij})\big\rangle_0}{\partial\sigma_i}+\frac{1}{2}\frac{\partial F''_{\rm M}\big(\langle\omega_j\rangle_0\big)}{\partial\sigma_i}C_j+\frac{1}{2}F''_{\rm M}\big(\langle\omega_j\rangle_0\big)\frac{\partial C_j}{\partial\sigma_i}\Big)+\sum_{j\in I_{\rm H},\ j\neq i}x_j\Big(\frac{\partial F_{\rm H}\big(\langle\omega_j\rangle_0\big)}{\partial\sigma_i}$$
$$+\frac{\partial\big\langle\phi_{\rm HH}(r_{ij})\big\rangle_0}{\partial\sigma_i}+\frac{1}{2}\frac{\partial F''_{\rm H}\big(\langle\omega_j\rangle_0\big)}{\partial\sigma_i}C_j+\frac{1}{2}F''_{\rm H}\big(\langle\omega_j\rangle_0\big)\frac{\partial C_j}{\partial\sigma_i}\Big)\Big)-\frac{3k_{\rm B}}{\sigma_i},\quad\forall i\in I_{\rm H},\tag{2.60}$$

where $\partial F/\partial\sigma$, $\partial F''/\partial\sigma$ and $\partial C/\partial\sigma$ can be calculated based on Eqs. (2.54) and (2.55) by replacing $\partial\bar{\boldsymbol{q}}_i$ with $\partial\sigma_i$. The gradients $\partial\langle f\rangle_0/\partial\sigma_i$, $\partial\langle\phi\rangle_0/\partial\sigma_i$ and $\partial\langle f^2\rangle_0/\partial\sigma_i$ — collectively represented by $\partial\langle g\rangle_0/\partial\sigma_i$ — are given by

$$\frac{\partial\big\langle g(r_{ij})\big\rangle_0}{\partial\sigma_i}=\sum_{k=1}^{k_{\rm max}}g'(r_{ij,k})\frac{\boldsymbol{r}_{ij,k}\cdot\boldsymbol{s}_{i,k}}{r_{ij,k}}W_k,\tag{2.61}$$

which is a function of state variables. Therefore, $\partial\mathcal{F}/\partial\sigma_i$ is a function of $\{\bar{\boldsymbol{q}}\}$ and $\{\sigma\}$.

3. γ_i is given by

$$\gamma_i=\frac{3}{2}+\log\frac{x_i}{1-x_i}+\frac{1}{k_{\rm B}T}\Big(\sum_{j\in I_{\rm M}}\Big(\frac{\partial F_{\rm M}\big(\langle\omega_j\rangle_0\big)}{\partial x_i}+\frac{1}{2}\frac{\partial F''_{\rm M}\big(\langle\omega_j\rangle_0\big)}{\partial x_i}C_j+\frac{1}{2}F''_{\rm M}\big(\langle\omega_j\rangle_0\big)\frac{\partial C_j}{\partial x_i}$$
$$+\big\langle\phi_{\rm MH}(r_{ij})\big\rangle_0\Big)+F'_{\rm H}\big(\langle\omega_i\rangle_0\big)+\frac{1}{2}F''_{\rm H}\big(\langle\omega_i\rangle_0\big)C_i+\sum_{j\in I_{\rm H},\ j\neq i}x_j\Big(\frac{\partial F_{\rm H}\big(\langle\omega_j\rangle_0\big)}{\partial x_i}$$
$$+\frac{1}{2}\frac{\partial F''_{\rm H}\big(\langle\omega_j\rangle_0\big)}{\partial x_i}C_j+\frac{1}{2}F''_{\rm H}\big(\langle\omega_j\rangle_0\big)\frac{\partial C_j}{\partial x_i}+\big\langle\phi_{\rm HH}(r_{ij})\big\rangle_0\Big)\Big),\quad\forall i\in I_{\rm H},\tag{2.62}$$

where the gradients of F, F'' — collectively represented by G — and C with respect

to x_i are given by

$$\frac{\partial G\big(\langle\omega_j\rangle_0\big)}{\partial x_i} = G'\big(\langle\omega_j\rangle_0\big)\big\langle f_{\rm H}(r_{ij})\big\rangle_0, \quad \forall i \in I_{\rm H},\ \forall j \in I_{\rm M}\cup I_{\rm H},\ j\neq i,$$
$$\frac{\partial C_j}{\partial x_i} = \big\langle f_{\rm H}^2(r_{ij})\big\rangle_0 - 2x_i\big\langle f_{\rm H}(r_{ij})\big\rangle_0^2 + 2\sum_{l\in I_{\rm M}} {\rm Cov}\Big[f_{\rm M}\big(r_{jl}^{(0)}\big),\ f_{\rm H}\big(r_{ij}^{(0)}\big)\Big]$$
$$+ 2\sum_{l\in I_{\rm H},\ l\neq i} x_l {\rm Cov}\Big[f_{\rm H}\big(r_{jl}^{(0)}\big),\ f_{\rm H}\big(r_{ij}^{(0)}\big)\Big], \quad \forall i \in I_{\rm H},\ \forall j \in I_{\rm M}\cup I_{\rm H},\ i\neq j,\ l\neq j. \tag{2.63}$$

The covariances are calculated off-line. Similarly, γ_i is a function of $\{\bar{\boldsymbol{q}}\}$ and $\{\sigma\}$.

Bibliography

[1] A. Pundt, Hydrogen in nano-sized metals, Advanced Engineering Materials 6 (1-2) (2004) 11–21.

[2] O. V. Salata, Applications of nanoparticles in biology and medicine, Journal of Nanobiotechnology 2 (1) (2004) 3.

[3] W. Lu, C. M. Lieber, Nanoelectronics from the bottom up, Nature Materials 6 (11) (2007) 841–850.

[4] X. Su, Q. Wu, J. Li, X. Xiao, A. Lott, W. Lu, B. W. Sheldon, J. Wu, Silicon-based nanomaterials for lithium-ion batteries: a review, Advanced Energy Materials 4 (1).

[5] S. Plimpton, Computational limits of classical molecular dynamics simulations, Computational Materials Science 4 (4) (1995) 361 – 364.

[6] A. F. Voter, F. Montalenti, T. C. Germann, Extending the time scale in atomistic simulation of materials, Annual Review of Materials Research 32 (1) (2002) 321–346.

[7] R. A. Miron, K. A. Fichthorn, Accelerated molecular dynamics with the bond-boost method, The Journal of Chemical Physics 119 (12) (2003) 6210–6216.

[8] I. Brihuega, O. Custance, J. Gómez-Rodríguez, Surface diffusion of single vacancies on ge (111)- c (2× 8) studied by variable temperature scanning tunneling microscopy, Physical Review B 70 (16) (2004) 165410.

[9] A. F. Voter, Introduction to the kinetic monte carlo method, in: Radiation Effects in Solids, Springer, 2007, pp. 1–23.

[10] R. A. Miron, K. A. Fichthorn, Heteroepitaxial growth of co/ cu (001): An accelerated molecular dynamics simulation study, Physical Review B 72 (3) (2005) 035415.

[11] R. LeSar, R. Najafabadi, D. J. Srolovitz, Finite-temperature defect properties from free-energy minimization, Phys. Rev. Lett. 63 (1989) 624–627.

[12] D. Perez, L. J. Lewis, Multiscale model for microstructure evolution in multiphase materials: Application to the growth of isolated inclusions in presence of elasticity, Physical Review E 74 (3) (2006) 031609.

[13] J. Li, S. Sarkar, W. T. Cox, T. J. Lenosky, E. Bitzek, Y. Wang, Diffusive molecular dynamics and its application to nanoindentation and sintering, Physical Review B 84 (5) (2011) 054103.

[14] S. Sarkar, J. Li, W. T. Cox, E. Bitzek, T. J. Lenosky, Y. Wang, Finding activation pathway of coupled displacive-diffusional defect processes in atomistics: Dislocation climb in fcc copper, Physical Review B 86 (1) (2012) 014115.

[15] G. Venturini, K. Wang, I. Romero, M. P. Ariza, M. Ortiz, Atomistic long-term simulation of heat and mass transport, Journal of the Mechanics and Physics of Solids 73 (2014) 242–268.

[16] K. Wang, M. Ortiz, M. P. Ariza, Long-term atomistic simulation of hydrogen diffusion in metals, International Journal of Hydrogen Energy 40 (15) (2015) 5353–5358.

[17] X. Sun, M. P. Ariza, K. Wang, Deformation-diffusion coupled analysis of long-term hydrogen diffusion in nanofilms, in: Proceedings of VII European Congress on Computational Methods in Applied Sciences and Engineering, Vol. 1, ECCOMAS, 2016, pp. 197–208.

[18] B. A. Farmer, M. Luskin, P. Plecháč, G. Simpson, Spin-diffusions and diffusive molecular dynamics, arXiv preprint arXiv:1702.01469.

[19] G. Simpson, M. Luskin, D. J. Srolovitz, A theoretical examination of diffusive molecular dynamics, SIAM Journal on Applied Mathematics 76 (6) (2016) 2175–2195.

[20] T. C. Narayan, F. Hayee, A. Baldi, A. L. Koh, R. Sinclair, J. A. Dionne, Direct visualization of hydrogen absorption dynamics in individual palladium nanoparticles, Nature Communications 8 (2017) 14020.

[21] L. Verlet, Computer" experiments" on classical fluids. i. thermodynamical properties of lennard-jones molecules, Physical Review 159 (1) (1967) 98.

[22] X.-Y. Liu, J. B. Adams, F. Ercolessi, J. A. Moriarty, Eam potential for magnesium from quantum mechanical forces, Modelling and Simulation in Materials Science and Engineering 4 (3) (1996) 293.

[23] M. I. Baskes, Modified embedded-atom potentials for cubic materials and impurities, Physical Review B 46 (1992) 2727–2742.

[24] S. Piperno, Explicit/implicit fluid/structure staggered procedures with a structural predictor and fluid subcycling for 2d inviscid aeroelastic simulations, International Journal for Numerical Methods in Fluids 25 (10) (1997) 1207–1226.

[25] A. Valli, G. Carey, A. Coutinho, On decoupled time step/subcycling and iteration strategies for multiphysics problems, International Journal for Numerical Methods in Biomedical Engineering 24 (12) (2008) 1941–1952.

[26] X. Yu, A. E. Jeffers, A comparison of subcycling algorithms for bridging disparities in temporal scale between the fire and solid domains, Fire Safety Journal 59 (2013) 55–61.

[27] A. Ulvestad, M. Welland, S. Collins, R. Harder, E. Maxey, J. Wingert, A. Singer, S. Hy,

P. Mulvaney, P. Zapol, et al., Avalanching strain dynamics during the hydriding phase transformation in individual palladium nanoparticles, Nature Communications 6 (2015) 1–8.

[28] W. Li, C. Li, H. Ma, J. Chen, Magnesium nanowires: enhanced kinetics for hydrogen absorption and desorption, Journal of the American Chemical Society 129 (21) (2007) 6710–6711.

[29] E. T. Jaynes, Information theory and statistical mechanics i, Physical Review 106 (4) (1957) 620–630.

[30] E. T. Jaynes, Information theory and statistical mechanics ii, Physical Review 108 (2) (1957) 171–190.

[31] M. Ponga, M. Ortiz, M. P. Ariza, Finite-temperature non-equilibrium quasi-continuum analysis of nanovoid growth in copper at low and high strain rates, Mechanics of Materials 90 (2015) 253–267.

[32] M. S. Daw, M. I. Baskes, Embedded-atom method: Derivation and application to impurities, surfaces, and other defects in metals, Physical Review B 29 (12) (1984) 6443.

[33] N. Metropolis, S. Ulam, The monte carlo method, Journal of the American Statistical Association 44 (247) (1949) 335–341.

[34] G. H. Golub, J. H. Welsch, Calculation of gauss quadrature rules, Mathematics of Computation 23 (106) (1969) 221–230.

[35] Y. Kulkarni, J. Knap, M. Ortiz, A variational approach to coarse graining of equilibrium and non-equilibrium atomistic description at finite temperature, Journal of the Mechanics and Physics of Solids 56 (4) (2008) 1417–1449.

[36] R. LeSar, R. Najafabadi, D. Srolovitz, Thermodynamics of solid and liquid embedded-atom-method metals: A variational study, The Journal of Chemical Physics 94 (7) (1991) 5090–5097.

[37] E. Dontsova, J. Rottler, C. Sinclair, Solute-defect interactions in al-mg alloys from diffusive variational gaussian calculations, Physical Review B 90 (17) (2014) 174102.

[38] J. Nocedal, Updating quasi-newton matrices with limited storage, Mathematics of Computation 35 (151) (1980) 773–782.

[39] S. Balay, S. Abhyankar, M. F. Adams, J. Brown, P. Brune, K. Buschelman, L. Dalcin, V. Eijkhout, W. D. Gropp, D. Kaushik, M. G. Knepley, L. C. McInnes, K. Rupp, B. F. Smith, S. Zampini, H. Zhang, H. Zhang, PETSc users manual, Tech. Rep. ANL-95/11 - Revision 3.7, Argonne National Laboratory (2016).

[40] G. Li, H. Kobayashi, J. M. Taylor, R. Ikeda, Y. Kubota, K. Kato, M. Takata, T. Yamamoto, S. Toh, S. Matsumura, et al., Hydrogen storage in pd nanocrystals covered with a metal–organic framework, Nature Materials 13 (8) (2014) 802–806.

[41] Y.-M. Lin, G.-L. Lee, M.-H. Rei, An integrated purification and production of hydrogen with a palladium membrane-catalytic reactor, Catalysis Today 44 (1) (1998) 343–349.

[42] R. J. Wolf, M. W. Lee, R. C. Davis, P. J. Fay, J. R. Ray, Pressure-composition isotherms for palladium hydride, Physical Review B 48 (17) (1993) 12415.

[43] X. Zhou, J. A. Zimmerman, B. M. Wong, J. J. Hoyt, An embedded-atom method interatomic potential for pd–h alloys, Journal of Materials Research 23 (03) (2008) 704–718.

[44] Webpage for BlueRidge (Sandy Bridge), `https://secure.hosting.vt.edu/www.arc.vt.edu/computing/blueridge-sandy-bridge/`.

[45] R. W. Balluffi, S. Allen, W. C. Carter, Kinetics of materials, John Wiley & Sons, 2005.

[46] G. Li, H. Kobayashi, S. Dekura, R. Ikeda, Y. Kubota, K. Kato, M. Takata, T. Yamamoto, S. Matsumura, H. Kitagawa, Shape-dependent hydrogen-storage properties in pd nanocrystals: which does hydrogen prefer, octahedron (111) or cube (100)?, Journal of the American Chemical Society 136 (29) (2014) 10222–10225.

[47] H. Okuyama, W. Siga, N. Takagi, M. Nishijima, T. Aruga, Path and mechanism of hydrogen absorption at pd (100), Surface Science 401 (3) (1998) 344–354.

[48] A. Zalineeva, S. Baranton, C. Coutanceau, G. Jerkiewicz, Octahedral palladium nanoparticles as excellent hosts for electrochemically adsorbed and absorbed hydrogen, Science Advances 3 (2) (2017) e1600542.

[49] A. Baldi, T. C. Narayan, A. L. Koh, J. A. Dionne, In situ detection of hydrogen-induced

phase transitions in individual palladium nanocrystals, Nature Materials 13 (12) (2014) 1143–1148.

[50] T. C. Narayan, A. Baldi, A. L. Koh, R. Sinclair, J. A. Dionne, Reconstructing solute-induced phase transformations within individual nanocrystals, Nature Materials 15 (7) (2016) 768–774.

[51] A. Ulvestad, M. Welland, W. Cha, Y. Liu, J. Kim, R. Harder, E. Maxey, J. Clark, M. Highland, H. You, et al., Three-dimensional imaging of dislocation dynamics during the hydriding phase transformation, Nature Materials 16 (2017) 565–571.

Chapter 3

Long-Term Atomistic Simulation of Hydrogen Absorption in Palladium Nanocubes Using a Diffusive Molecular Dynamics Method

(Published in *International Journal of Hydrogen Energy*, 43(11), 5657-5667, 2018.)

X. Sun [a], M. P. Ariza [b], M. Ortiz [c], K. G. Wang [a]

[a] Department of Aerospace and Ocean Engineering, Virginia Polytechnic Institute and State University, Blacksburg, VA 24061, United States

[b] Escuela Técnica Superior de Ingeniería, Universidad de Sevilla, Sevilla 41092, Spain

[c] Division of Engineering and Applied Science, California Institute of Technology, Pasadena, CA 91125, United States

Abstract

Understanding the transport of hydrogen within metallic nanomaterials is crucial for the advancement of energy storage and the mitigation of hydrogen embrittlement. Using nanosized palladium particles as a model, recent experimental studies have revealed several interesting phenomena that occur over long time periods. The time scale of these phenomena is beyond the capability of established atomistic models such as molecular dynamics. In this work, we present the application of a new approach, referred to as diffusive molecular dynamics (DMD), to the simulation of long-term diffusive mass transport at the atomic scale. Specifically, we simulate the absorption of hydrogen by palladium nanocubes with edge lengths in the range of 4 nm and 16 nm. We find that the absorption process is dominated by the initiation and propagation of an atomistically sharp α/β Pd-H phase boundary, with thickness in the range of 0.2 to 1.0 nm, which separates an α phase core from a β phase shell. The evolution of phase boundary and the resulting local lattice deformation are described in this paper in detail. The effects of size on both equilibrium and kinetic properties are also assessed.

Keywords

Palladium Nanocubes, Hydrogen Absorption, Phase Boundary Propagation, Lattice Deformation, Size Effects, Diffusive Molecular Dynamics

3.1 Introduction

Solute-induced phase transformation is a fundamental process in various energy conversion and storage applications. For example, the storage of hydrogen in metals relies on the phase transformation of the hydride (e.g., MgH_x, $NaAlH_x$), induced by the diffusion of hydrogen atoms [1, 2, 3, 4]. Similarly, the operation of lithium-ion batteries relies on a reversible phase transformation in the cathodic material (e.g., Li_xCoO_2, Li_xFePO_4), induced by the diffusion of lithium ions [5]. For these applications, there has been a continuous push towards nanostructured systems, as they hold promise to accelerate the charging and discharging process, increase the energy and power density, and extend the life cycle [5, 6, 7].

The palladium-hydrogen (Pd-H) system is a prototypical model for studying solute-induced phase transformation, because it allows for relatively fast reaction kinetics at easily accessible temperatures and pressures [8]. The Pd-H system exhibits two distinct phases at room temperature: the dilute α phase at low H concentration (up to $PdH_{0.015}$), and the β phase at high H concentration ($PdH_{0.6}$ and above). In both phases, the Pd lattice maintains the face-centered cubic (FCC) structure, while the H atoms occupy the interstitial octahedral sites.

Attendant to the α/β phase transformation, there is a lattice expansion with approximately 3.5% increase in lattice constant [9] and 10.4% increase in volume, which, in bulk materials, results in the formation of misfit dislocations.

While the behavior of Pd-H is well-understood in the bulk, the phase transformation dynamics within nanostructured Pd-H systems is an active area of ongoing research [10, 11, 12, 13, 14, 15, 16, 17]. Specifically, the sloped isotherms of nanoparticle ensembles seem to suggest that the phase transformation is continuous, and hence the two phases may coexist in equilibrium [10]. However, this hypothesis is challenged by several recent experiments at the scale of individual nanoparticles. For example, using scanning transmission electron microscopy, Narayan *et al.* observed the propagation of a sharp α/β phase boundary in individual Pd nanocubes with edge lengths between 10 and 35 nm [15]. Using coherent X-ray diffractive imaging, Ulvestad *et al.* measured the evolution of strain within individual Pd nanocubes between 120 and 340 nm, which also indicates a sharp α/β phase transformation [13, 16]. Beyond the overall transformation mechanism, i.e., *continuous transformation* versus *phase boundary propagation*, other unresolved issues include the morphology of the phase boundary, e.g., *spherical shell* versus *spherical cap* [11, 15, 16], the effect of particle shape and lattice orientation [12], and the interaction of phase boundary with preexisting defects [14].

Moreover, these experimental studies suggest that in nanosized particles, the α/β phase boundary may be atomistically sharp, and it may propagate very slowly at around 1 nm/s. This confluence of atomistic length scale and a long time scale (i.e., minutes or longer) chal-

lenges theory and simulation. Phase-field models have been applied to interpret some of the experimental results from nanosized Pd particles [11, 13]. However, continuum models fail to account for the fine atomistic structure (e.g., local lattice distortion and dislocations) across the phase boundary. By way of contrast, classical Molecular Dynamics (MD) does supply full atomistic detail [18], but the need to resolve the thermal vibrations of the atoms places slow diffusive processes such as phase boundary propagation outside its scope. Transition state theory based accelerated MD methods [19] and kinetic Monte Carlo (kMC) methods [20] have been developed to expand the simulation time window of MD while maintaining full atomistic fidelity. However, for mass transport problems, such as hydride phase boundary propagation, the total time window accessible to these methods is limited by the frequency of individual atom hops within the material sample and is typically less than one second [21]. Besides the aforementioned kinetic models, the equilibrium MC method has also been applied to investigate H absorption by Pd nanoparticles and nanofilms, which predicted isotherms at different equilibrium states [22, 23, 24].

In this work, we apply a novel computational model, referred to as diffusive molecular dynamics (DMD), to the investigation of the detailed dynamics of H absorption and hydride phase propagation within Pd nanocubes with edge lengths in the range of 4 nm to 16 nm. DMD is a new paradigm for simulating long-term diffusive mass and heat transport while maintaining full atomic resolution [17, 25, 26, 27, 28, 29, 30]. Its defining idea is to couple a calibrated empirical kinetic model for the evolution of lattice site occupancy with a non-equilibrium statistical thermodynamics model that supplies the requisite driving forces

for kinetics. The basic assumption underlying DMD is that the time scale of diffusion is much larger than that of microscopic state transitions. Therefore at an intermediate time scale, the microscopic state variables can be considered as random variables. In comparison to the established atomistic models mentioned above, DMD has a larger simulation time window as it does not explicitly resolve thermal vibrations nor individual microscopic state transitions. It has been applied to nanoindentation and sintering [25], dislocation extension [26], nanovoid growth [31], solute-defect interactions [32] and silicon lithiation [33]. In particular, a recent study by Wang *et al.* [17] shows that the DMD model, when equipped with an embedded atom method (EAM) potential function [34], is capable of capturing the separation of the α and β phases of Pd-H. In Reference [17], the DMD model is also validated against experimental data for the desorption of hydrogen in Pd nanofilms. Nonetheless, the study was limited to a one-dimensional analysis of hydrogen diffusion within thin Pd films. Also, the lattice deformation induced by hydrogen diffusion was neglected. The application of the DMD theory to investigate three-dimensional Pd-H systems — accounting for the deformation-diffusion coupling — is therefore the main novelty of the present paper.

The large time window and atomic resolution of DMD renders it an excellent tool for studying hydride phase transformations within Pd nanoparticles, which operates on time scales of seconds to minutes. In this work, we begin by presenting a succinct summary of DMD in the interest of completeness, in Section 3.2. The assumptions and computational setup are subsequently described in Section 3.3. Simulation results concerned with the final equilibrium state, the morphology of the α/β Pd-H phase boundary, the attendant local lattice distortion,

the absorption transient, as well as the effect of nanoparticle size are presented in Section 3.4. A summary and concluding remarks are consigned to Section 3.5 by way of closing.

3.2 Methodology

We consider an FCC Pd sample, which includes host sites occupied by Pd atoms and interstitial octahedral sites that can be either occupied by H atoms or unoccupied. For ease of reference, we denote the host sites by I_{Pd}, and the interstitial sites by I_{H}. At each interstitial site $i \in I_{\mathrm{H}}$, we introduce an occupancy function defined as

$$n_i = \begin{cases} 1 & \text{if the site } i \text{ is occupied by H atom} \\ 0 & \text{if the site } i \text{ is unoccupied} \end{cases}. \tag{3.1}$$

The instantaneous position and momentum of each site i are denoted by $\boldsymbol{q}_i$ and $\boldsymbol{p}_i$, respectively. Based on the assumption of scale separation and the ergodic hypothesis, these microscopic state variables can be viewed as random variables that have a joint probability distribution characterized by density function $\rho\big(\{\boldsymbol{q}\},\{\boldsymbol{p}\},\{n\}\big)$, where $\{\boldsymbol{q}\} = (\boldsymbol{q}_i)_{i\in I_{\mathrm{Pd}}\cup I_{\mathrm{H}}}$, $\{\boldsymbol{p}\} = (\boldsymbol{p}_i)_{i\in I_{\mathrm{Pd}}\cup I_{\mathrm{H}}}$ and $\{n\} = (n_i)_{i\in I_{\mathrm{H}}}$. We determine ρ by applying Jaynes' principles of maximum entropy [35, 36], i.e., by maximizing the information-theoretical entropy

$$S[\rho] = -k_{\mathrm{B}}\langle \log \rho \rangle, \tag{3.2}$$

with the local constraints

$$\begin{cases} \langle h_i \rangle = e_i, & i \in I_{\mathrm{Pd}} \cup I_{\mathrm{H}} \\ \langle n_i \rangle = x_i, & i \in I_{\mathrm{H}} \end{cases}, \tag{3.3}$$

where k_{B} is the Boltzmann constant, and $\langle \cdot \rangle$ represents the expectation operator. Here, h_i, e_i and x_i denote the local Hamiltonian, particle energy and H atomic fraction of site i, respectively. As a result, we have

$$\rho = \frac{1}{\Xi} \mathrm{e}^{-\{\beta\}^{\mathrm{T}}\{h\}+\{\gamma\}^{\mathrm{T}}\{n\}}, \tag{3.4}$$

where Ξ is the partition function, and $\{\beta\}$ and $\{\gamma\}$ are Lagrange multipliers. In comparison with equilibrium statistical thermodynamics, Eq. (3.4) can be interpreted as non-equilibrium generalization of the Gibbs grand-canonical probability density function. Also, $T_i = 1/(k_{\mathrm{B}}\beta_i)$ and $\mu_i = k_{\mathrm{B}} T_i \gamma_i$ can be defined as the particle absolute temperature and the chemical potential of site i, respectively.

Because the Hamiltonian h_i is typically a nonlinear function, the calculation of the thermodynamic potentials (e.g., e_i and Ξ) is generally intractable. Venturini et al. [27] proposed an approximation theory, in which the optimization problem is performed within a finite-dimensional trial space. We consider uniform temperature and apply the approximation

theory with a carefully designed trial Hamiltonian

$$
\begin{aligned}
&h_{0i}(\boldsymbol{q}_i, \boldsymbol{p}_i, n_i;\ \bar{\boldsymbol{q}}_i, \sigma_i, \bar{\boldsymbol{p}}_i, \gamma_{0i}) \\
&= \begin{cases} \dfrac{k_{\mathrm{B}}T}{2\sigma_i^2}|\boldsymbol{q}_i - \bar{\boldsymbol{q}}_i|^2 + \dfrac{1}{2m_{\mathrm{Pd}}}|\boldsymbol{p}_i - \bar{\boldsymbol{p}}_i|^2, & \text{if } i \in I_{\mathrm{Pd}} \\ \dfrac{k_{\mathrm{B}}T}{2\sigma_i^2}|\boldsymbol{q}_i - \bar{\boldsymbol{q}}_i|^2 + \dfrac{1}{2m_{\mathrm{H}}}|\boldsymbol{p}_i - \bar{\boldsymbol{p}}_i|^2 - k_{\mathrm{B}}T\gamma_{0i}n_i, & \text{if } i \in I_{\mathrm{H}} \end{cases},
\end{aligned} \tag{3.5}
$$

where T is the constant temperature, $\bar{\boldsymbol{q}}_i$, σ_i, $\bar{\boldsymbol{p}}_i$, and γ_{0i} are parameters that characterize the trial space, and m_{Pd} and m_{H} denote the atomic mass of Pd and H, respectively. It can be shown that $\bar{\boldsymbol{q}}_i$ and σ_i are the mean and standard deviation of $\boldsymbol{q}_i$, respectively, whereas $\bar{\boldsymbol{p}}_i$ is the mean of $\boldsymbol{p}_i$. In Eq. (3.5), γ_{0i} indicates the dependence of chemical potential on H fraction x_i. Specifically, by calculating $\langle n_i \rangle_0$, where $\langle \cdot \rangle_0$ denotes the expectation operator under the trial probability density function, and applying the relation $\langle n_i \rangle_0 = x_i$, we obtain

$$
\gamma_{0i} = \log \frac{x_i}{1 - x_i} - \gamma_i. \tag{3.6}
$$

After straightforward derivations according to Reference [27], and using Eq. (3.6), the opti-

mization problem of Eq. (3.2) becomes

$$
\begin{aligned}
&\min_{\{\bar{\boldsymbol{q}}\},\{\sigma\},\{\bar{\boldsymbol{p}}\}} \mathcal{F}\big(T,\{\gamma\};\{\bar{\boldsymbol{q}}\},\{\sigma\},\{\bar{\boldsymbol{p}}\},\{x\}\big) \\
&= \frac{1}{T}\langle V\rangle_0 + \frac{1}{2Tm_{\mathrm{Pd}}}\sum_{i\in I_{\mathrm{Pd}}}\bar{\boldsymbol{p}}_i^2 + \frac{1}{2Tm_{\mathrm{H}}}\sum_{i\in I_{\mathrm{H}}} x_i\bar{\boldsymbol{p}}_i^2 \\
&+ \frac{3}{2}k_{\mathrm{B}}\sum_{i\in I_{\mathrm{Pd}}}\left(\log\frac{\hbar^2}{k_{\mathrm{B}}Tm_{\mathrm{Pd}}\sigma_i^2} - 1\right) \\
&+ \frac{3}{2}k_{\mathrm{B}}\sum_{i\in I_{\mathrm{H}}}\left(\log\frac{\hbar^2}{k_{\mathrm{B}}Tm_{\mathrm{H}}\sigma_i^2} + x_i - 2\right) \\
&+ k_{\mathrm{B}}\sum_{i\in I_{\mathrm{H}}}\big(x_i\log x_i + (1-x_i)\log(1-x_i) - \gamma_i x_i\big),
\end{aligned}
\tag{3.7}
$$

where $\hbar$ is the reduced Planck constant. $V\big(\{\boldsymbol{q}\},\{n\}\big)$ denotes the interatomic potential energy and its average is calculated by third-order Gaussian quadratures on a sparse grid [37]. The nondimensional chemical potential γ_i is obtained by enforcing the first-order necessary condition to atomic fraction x_i, which yields

$$
\gamma_i = \frac{3}{2} + \log\frac{x_i}{1-x_i} + \frac{1}{k_{\mathrm{B}}T}\frac{\partial\langle V\rangle_0}{\partial x_i}, \quad i\in I_{\mathrm{H}}. \tag{3.8}
$$

The thermodynamics model formulated in Eq. (3.7) is then coupled with a discrete diffusion law, which enforces the balance of mass at each interstitial site, i.e.,

$$
\dot{x}_i = \sum_{j\neq i} J_{ij}, \tag{3.9}
$$

where J_{ij} denotes the *bondwise* mass flux from site j to site i, and satisfies $J_{ij} = -J_{ji}$. For

simplicity, but without loss of generality, we restrict diffusive transport within one shell of neighbors, and enforce a linear dependence of the bondwise mass flux on both the H atomic fraction and the difference in chemical potential. As a result, we have

$$\dot{x}_i = -k_{\mathrm{B}} B_0 \sum_{j \in \mathcal{N}_i^{(1)}} \frac{x_i + x_j}{2} (\gamma_i - \gamma_j), \quad i \in I_{\mathrm{H}}, \tag{3.10}$$

where $\mathcal{N}_i^{(1)}$ denotes the first shell of neighbors of site i. B_0 denotes the bondwise diffusion coefficient, which can be calibrated to reproduce the speed of diffusion observed in experiments. It is noteworthy that B_0 should not be directly compared with the diffusion coefficient (in Fick's second law) measured in bulk Pd-H. Also, the classical Fick's second law would not be able to capture the initiation and propagation of sharp phase boundaries.

The above discrete diffusion law has been validated against the classical lattice random walk model for the long-term dynamics of a single H atom in Pd [30]. It has also been applied to study surface segregation in AuAg alloys [38]. Moreover, similar bondwise flux functions have been employed to simulate spin-diffusion in a one-dimensional binary alloy [39].

Our DMD model couples a nonlinear optimization problem with a first-order, nonlinear ordinary differential equation (ODE), i.e., Eqs. (3.7) and (3.10), respectively. We solve this coupled system by discretizing the ODE using an explicit time integrator, and solving the optimization problem once per time step using a quasi-Newton method BFGS (Broyden-Fletcher-Goldfarb-Shanno) algorithm [40]. We have parallelized the solver with Message Passing Interface (MPI), using the PETSc library [41] for large-scale simulations on com-

puter clusters with distributed memory. Details of the solutions of the equations and the computation procedure of DMD can be found in Reference [30]. The simulations reported in this work consume up to $7,000$ CPU hours (e.g., 24 hours on 300 CPU cores), using the BlueRidge supercomputer at Virginia Tech [42].

3.3 Simulation setup

Pd nanoparticles are capable of absorbing a large percentage of H atoms at room temperature. The process consists of three stages: (1) the dissociation of H_2 molecules into atoms on the surface of Pd nanoparticles; (2) the diffusion of H atoms into subsurface; and (3) the diffusion of H atoms into the interior (octahedral) interstitial sites [43, 44]. Here, we apply the proposed DMD model to simulate stage (3). Recent experimental studies suggest that for Pd nanoparticles, this step can take minutes or longer, and may be dominated by the propagation of a sharp α/β hydride phase boundary [16, 15, 13, 11, 45]. Given the large time scale and the nonlinear dynamics, we anticipate that the novel DMD model would be a useful analysis tool that can lead to improved understanding. In this work, we consider cubic nanoparticles with edge lengths (denoted by L) in the range of 4 nm and 16 nm (Fig. 3.1). All the samples are single crystals, and the surfaces are aligned with the [100], [010], and [001] directions.

Previous studies have shown that during stages (1) and (2), H atoms occupy the surface and subsurface interstitial sites of Pd nanoparticles in equilibrium with external H_2 partial

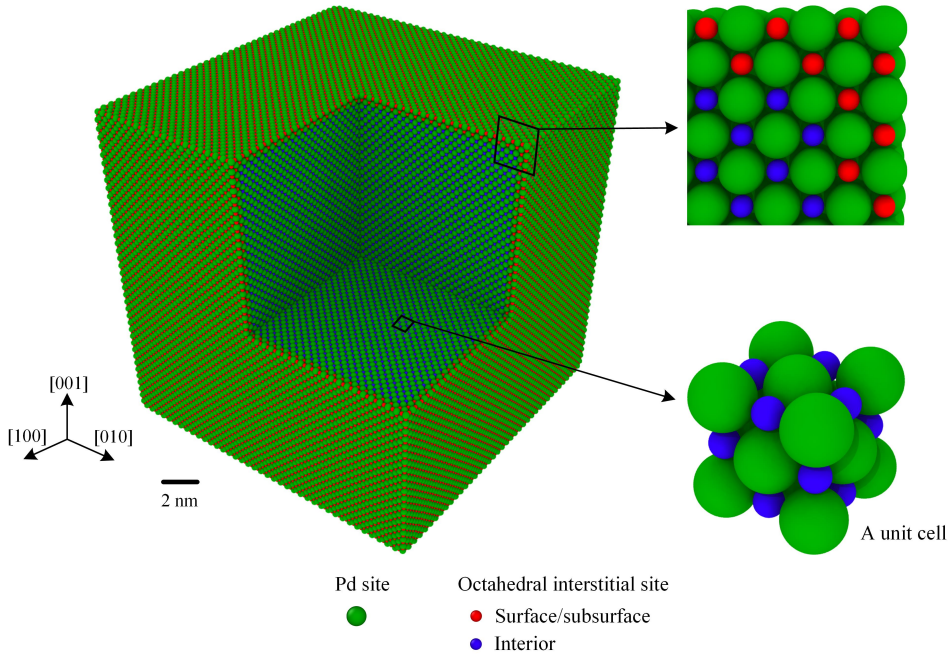

Figure 3.1: Simulation setup of H absorption by a Pd nanocube ($L = 16$ nm).

pressures below the α/β phase transformation pressure [46, 47]. Moreover, the time scale associated with surface and subsurface saturation is much smaller than that of H diffusion inside the nanoparticle [11, 44] . Therefore, we assume that at any time instance in the simulation, the surface and subsurface layers are partially or fully saturated with H atoms, with a constant atomic fraction $x = x_{\text{surf}}$. We also assume that the remaining octahedral sites in the interior of the particle, are unoccupied at the beginning of the simulation, and thus we set $x = 0$ at these sites at time $t = 0$. Then, the inward hydrogen diffusion starts owing to the initial gradient between the chemical potential γ on the subsurface and interior interstitial sites.

Moreover, we employ the embedded atom method (EAM) potential developed by Zhou *et al.* [34] to model the interatomic potential energy, and the temperature is fixed at $T = 300$ K.

The atomic diffusivity coefficient B_0 is set to 500.0 K/(eV $\cdot$ s), basing on recent experimental data for nanocubes of similar sizes [15]. The simulation results are visualized and post-processed using OVITO [48].

3.4 Results and discussion

Since the occupancy of octahedral sites by H atoms during the first two stages enforces the initial boundary conditions of the studies carried out in this work, our starting point consists on finding the threshold on the H atomic fraction that drives the inward diffusion of hydrogen in Pd nanocubes.

Thus, we have conducted a series of simulations, in which we proceed by varying the boundary condition x_{surf} between 0 to 1, and analyze the H atomic ratio at the end of the absorption process. Figure 3.2 shows, for three Pd nanocubes with edge lengths $L = 4$ nm, 8 nm, and 16 nm, the H atomic ratio in the interior of the cube, i.e., excluding the surface and subsurface layers (denoted by x_{int}), and that in the entire cube (denoted by x_{ent}). In Fig. 3.2(a), it can be seen that all the data points have $x_{\text{surf}} \geq x_{\text{int}}$. This indicates that at equilibrium, H atoms prefer to stay on and near the surface, than in the interior, of the nanocube. It is also notable that when $x_{\text{surf}} \leq 0.3$, $x_{\text{int}} \approx 0$. In other words, there is a threshold in boundary H concentration for the initiation of absorption. These findings are consistent with several experimental studies [46, 47] and recent simulation results using an equilibrium Monte Carlo method [49] and a phase-field model [44]. The simulation also predicts that when $x_{\text{surf}} = 1$,

the interior interstitial sites are fully occupied (i.e. $x_{\text{int}} = 1$), although this is difficult to achieve in practice, at temperature $T = 300$ K. Further, comparison of the two subfigures in Fig. 3.2 suggests that the effect of nanocube size (specifically, for 4 nm $< L <$ 16 nm) is dominated by the resulting variation in surface-to-volume ratio. Its effect on the interior H concentration (i.e., x_{int}), however, is not clearly captured. This may be due to the limited capability of the EAM potential in capturing the complete atomistic picture of hyrided Pd nanoparticles, which may exhibit different electronic states in the core and shell regions.

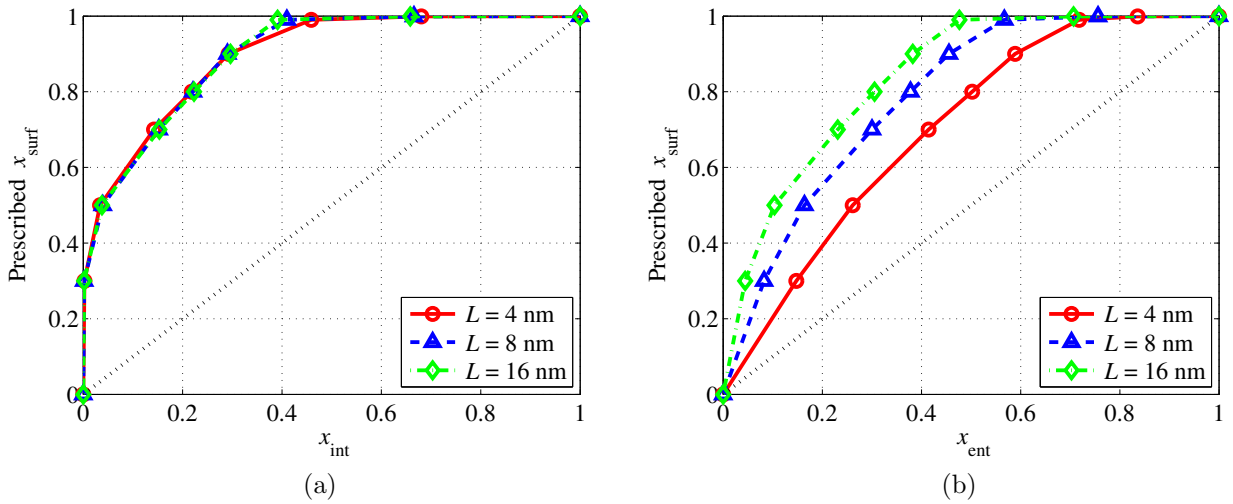

Figure 3.2: H concentration at equilibrium. In each subfigure, the dotted line without markers represent the result from the classical model $\gamma = \log(x)$.

3.4.1 Evolution of phase boundary

We examine the evolution of the α/β phase boundary for the case of $x_{\text{surf}} = 1$, i.e., the surface and subsurface layers are fully saturated. Figure 3.3 visualizes the evolution of the phase boundary for the three Pd nanocubes. We examine the distribution and variation

of H atomic ratio at four time instances, corresponding to $x_{\text{int}} = 0.1$, 0.5, 0.85, and 0.98, respectively. Specifically, from the two-dimensional images, it can be observed that at the beginning of the absorption process (e.g., when $x_{\text{int}} = 0.1$), all the three nanocubes form a *shell* with high H atomic ratio (close to 1.0), which indicates the β phase of Pd-H. The interior of the nanocubes, on the other hand, is in α phase, with low H atomic ratio (close to 0). The α and β phases are separated by a sharp boundary that consists of only a few layers of lattice sites. This phase boundary is extracted and visualized in three-dimension in Fig.3.3. As time increases, the phase boundary moves inwards, and its corners and edges become rounded. Near the end of the absorption process (e.g., when $x_{\text{int}} = 0.85$), the phase boundary evolves into a spherical shape. Finally, the phase boundary disappears after reaching the center of the nanocube, which also completes the absorption process. The observed phase boundary morphology likely suggests that, for the simulated nanocubes, the phase boundary moves faster in $\langle 111 \rangle$ or $\langle 110 \rangle$ directions than along $\langle 100 \rangle$ directions, which is consistent with the indication of a recent experiment by Narayan *et al.* [15].

It is notable that the thickness of the α/β phase boundary varies in the range of 0.2 to 1.0 nm, dependent upon time, location, and the size of the nanocube. Specifically, comparing the zoom-in view on the second row of Fig. 3.3 shows that as the size of the nanocube increases, so does the thickness of the phase boundary. Also, comparing each column of Fig. 3.3 shows that as time increases, the thickness of phase boundary first increases, then decreases. Furthermore, when the phase boundary has the shape of a rounded cube (e.g., at $x_{\text{int}} = 0.50$), its thickness is smaller in $\langle 111 \rangle$ and $\langle 110 \rangle$ directions than in $\langle 100 \rangle$ directions.

It can also be observed that the distribution of H atomic fraction is nonuniform on the phase boundary. In particular, early in the simulation, when the phase boundary has relatively sharp edges and corners, large gradient in H atomic fraction is observed near these geometric singularities.

Figure 3.4 compares statistically the H absorption process for the three nanocubes with different sizes. For all the nanocubes, the H atomic ratio increases monotonically in time, while the speed of H absorption — characterized by the time derivative of the H atomic ratio (Fig. 3.4 (b)) — decreases. As expected, the absorption process completes sooner in smaller nanocubes. Notably, the maximum speed of H absorption, obtained at $t = 0$ in all the three cases, increases as the size of the nanocube decreases.

Figure 3.5 visualizes the evolution of chemical potential ($\mu_i = k_{\mathrm{B}} T \gamma_i$) for the nanocube with $L = 16$ nm. Clearly, the α phase Pd-H has a lower chemical potential (approximately -2.57 eV) than the β phase (approximately -2.01 eV). This difference drives the diffusion of H from the subsurface to the interior. Moreover, the transition between these two values occurs within a relatively narrow band of interstitial sites, which supports the sharp α/β phase boundary observed in Fig. 3.3.

3.4.2 Evolution of local lattice distortion

Next, we examine the local Pd lattice distortion induced by the initiation and propagation of the α/β phase boundary. To characterize lattice distortion, we adopt the elastic Green-

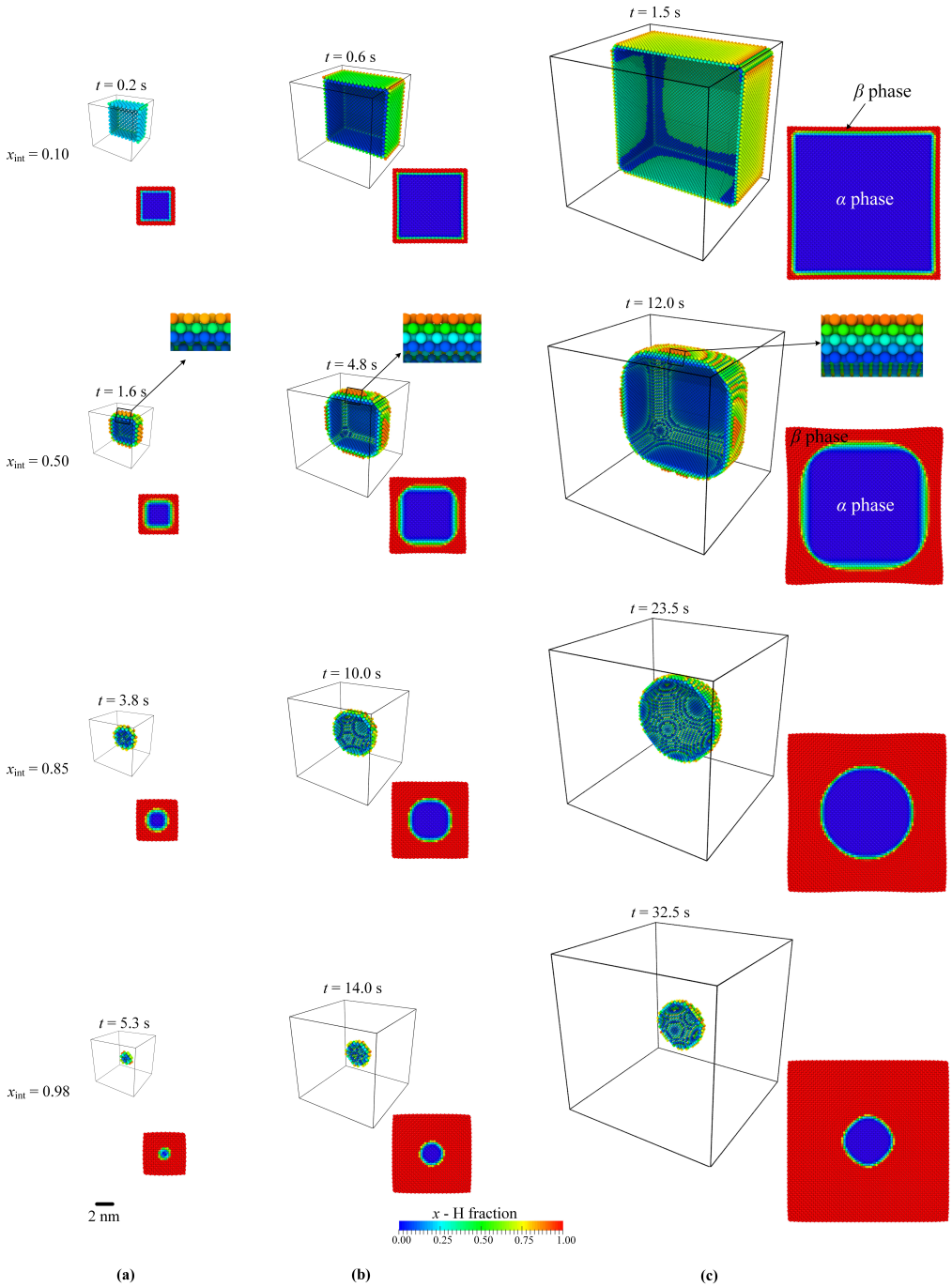

Figure 3.3: Evolution of the α/β Pd-H phase boundary: (a) $L = 4$ nm, (b) $L = 8$ nm, and (c) $L = 16$ nm. The three-dimensional snapshots visualize the phase boundary by displaying the subset of interstitial sites with H fraction $0.1 < x < 0.9$. The two-dimensional snapshots display the H fraction on the middle [100] cross-section.

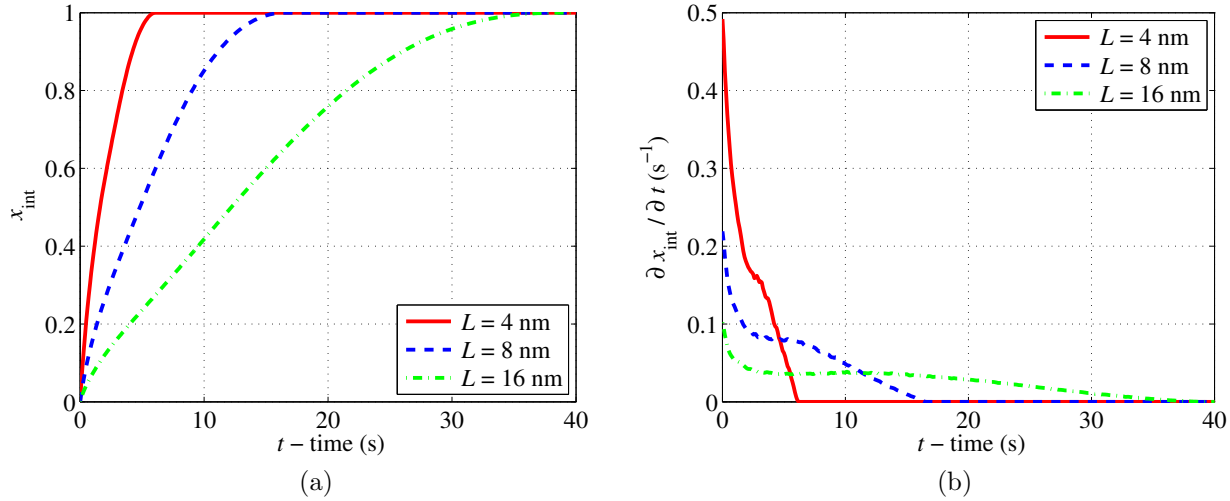

Figure 3.4: Time-history of H absorption: (a) H atomic ratio, and (b) the speed of H absorption.

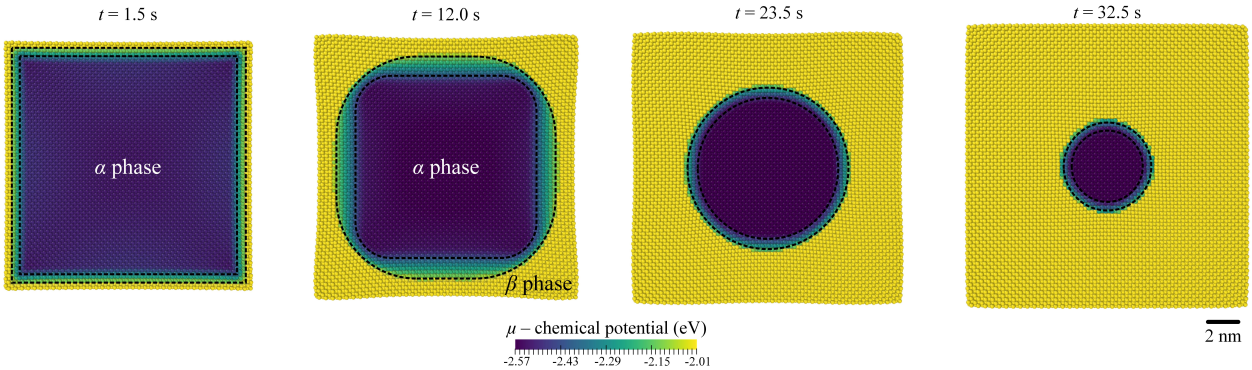

Figure 3.5: Evolution of chemical potential ($\mu_i = k_B T \gamma_i$) on the middle [100] cross-section ($L = 16$ nm).

Lagrangian strain tensor in the current atomistic setting (e.g., References [48, 50]). Figure 3.6 compares the distribution of the shear strain that is parallel to the y- and z-planes (denoted by ϵ_{yz}), between the initial state (i.e., $x_{int} = 0.00$ in Fig. 3.6(d)) and the final, equilibrium state (i.e., $x_{int} = 1.00$ in Fig. 3.6(d)). For all the three nanocubes, there is a clear inversion in strain direction at the corners. In particular, at the initial state, the corners are stretching

outwards along the body diagonals, forming a star-like shape. This shape is due to the H-rich surface and subsurface layers, and is likely to increase the surface area of the H-poor core. Conversely, at the final state, the nanocubes contract their corners inwards, evolving towards a spherical geometry, in order to reduce the surface energy. This behavior of *strain inversion* is consistent with the recent experimental result from Ulvestad *et al.* [13], despite that the nanocube studied therein is larger (edge length: 100 nm).

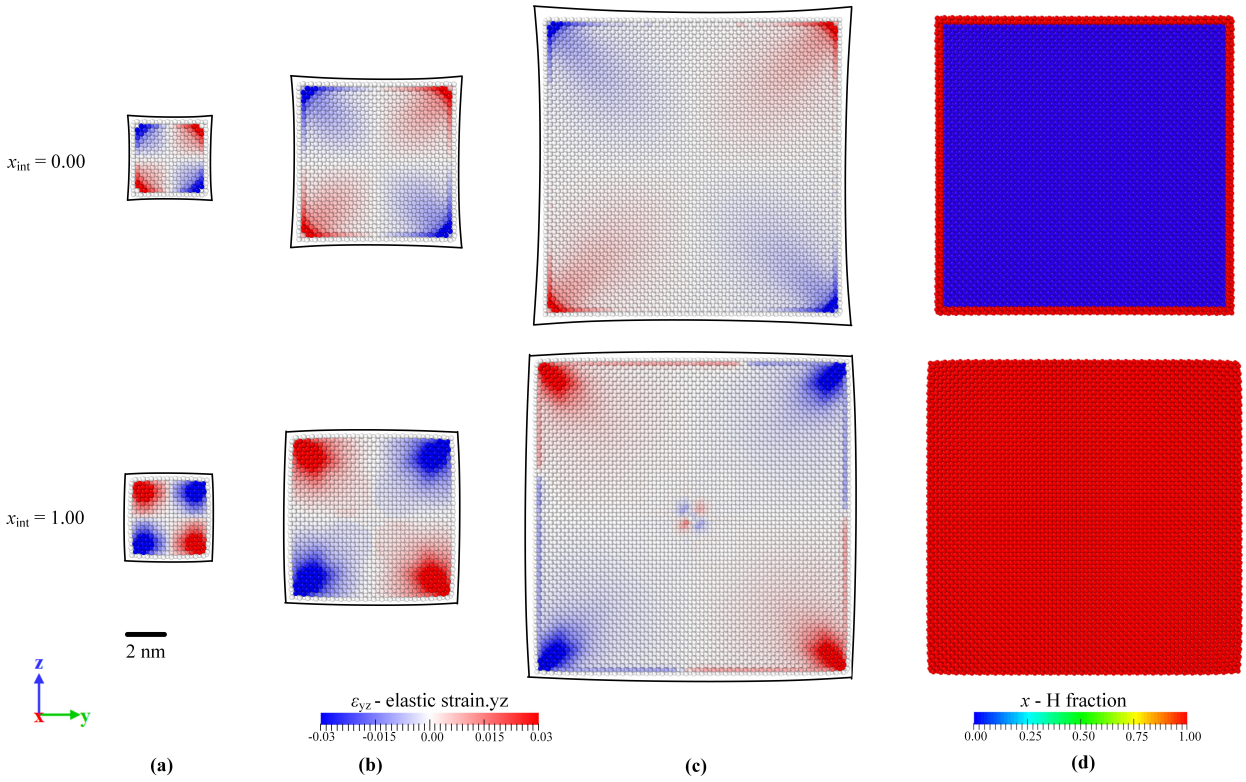

Figure 3.6: Inversion of shear strain on the middle [100] cross-section: (a) $L = 4$ nm, (b) $L = 8$ nm, and (c) $L = 16$ nm. Subfigure (d) shows the H atomic fraction for the nanocube with $L = 16$ nm.

Figure 3.7 visualizes the evolution of shear strain, with snapshots taken at the same time instances as in Fig. 3.3. In particular, it can be seen that when $x_{\text{int}} = 0.10$, the corners of the nanocube are distorted. Later, when $x_{\text{int}} = 0.50$, the distorted region expands and

moves inwards, along with the propagation of the α/β phase boundary. It is notable that the distorted region is primarily within the β phase shell, near the rounded regions of the phase boundary. On the other hand, the α phase core is largely intact. Also, the maximum value of $|\epsilon_{yz}|$ increases as the size of the nanocube increases, specifically, 0.06 for $L = 4$ nm, 0.12 for $L = 8$ nm and 0.15 for $L = 16$ nm. Finally, when $x_{\text{int}} = 0.85$ (and afterwards), the distorted region moves towards the center and dwindles, until H atoms saturate the entire Pd nanocube. It is also noteworthy that for the three simulated nanocubes, the phase boundary remains coherent, and no crystalline defect appears in the phase transformation process.

Figure 3.8 presents the volume fraction of the distorted region, using $|\epsilon_{yz}| > 0.01$ as a criterion. Before reaching equilibrium, for both $L = 8$ nm and 16 nm, the result exhibits an inverted U-shaped profile, while the result for $L = 4$ nm increases almost monotonically in time. In particular, the maximum value of the volume fraction increases as the size of the nanocube increases, specifically, 22.8 % for $L = 4$ nm, 24.5 % for $L = 8$ nm and 26.8 % for $L = 16$ nm. At the initial and the final states, the volume fraction is nonzero, due to the distortion at the corners of the nanocubes (Fig. 3.6).

3.5 Conclusions

The palladium-hydrogen (Pd-H) system serves as an excellent model for understanding solute-induced phase transformation. In particular, whereas hydride-phase transformations in bulk Pd have been long well-known, the corresponding behavior of nanosized Pd particles

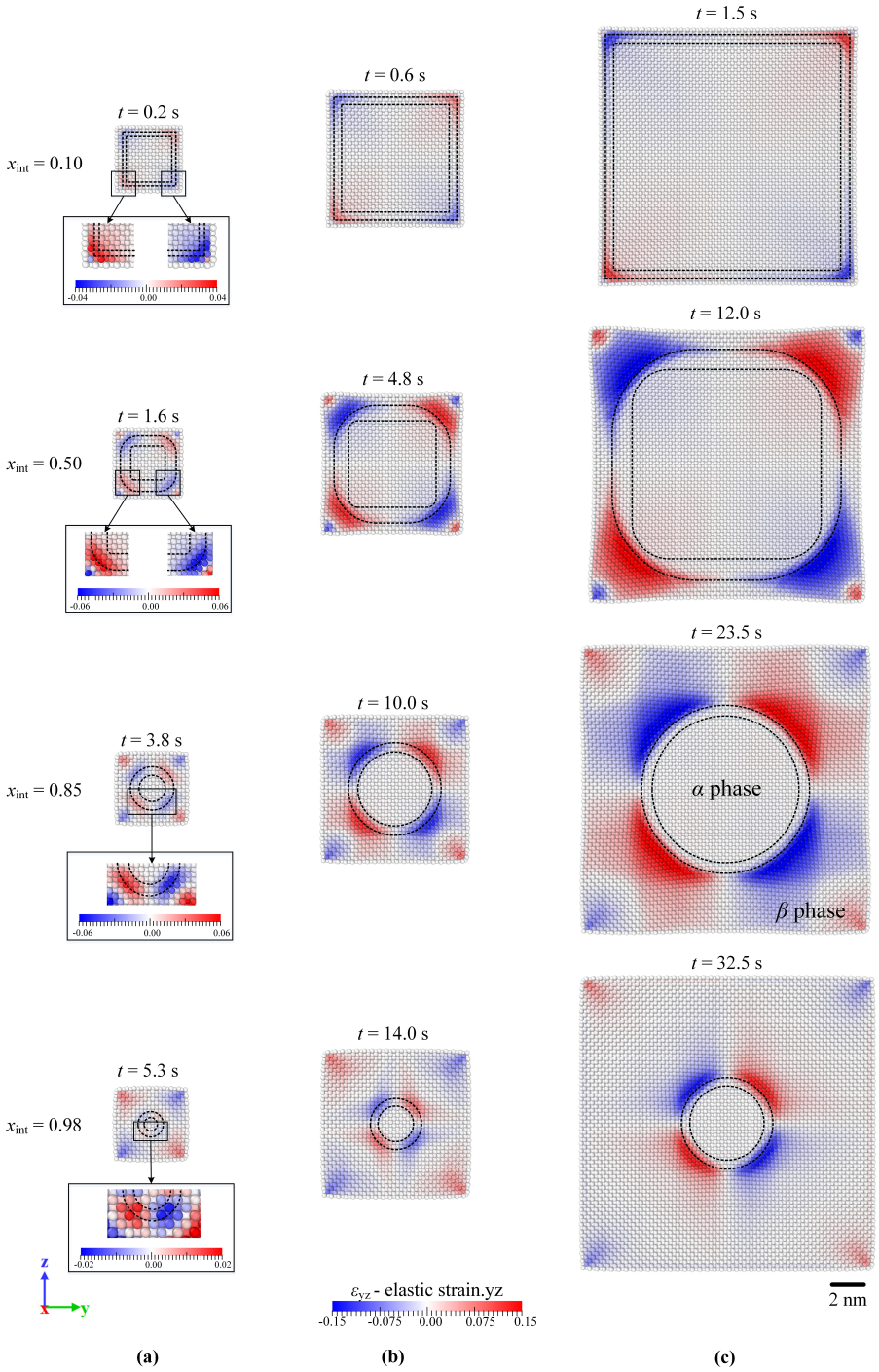

Figure 3.7: Evolution of shear strain on the middle [100] cross-section: (a) $L = 4$ nm, (b) $L = 8$ nm, and (c) $L = 16$ nm. In each subfigure, the dashed lines indicate the location of the phase boundary.

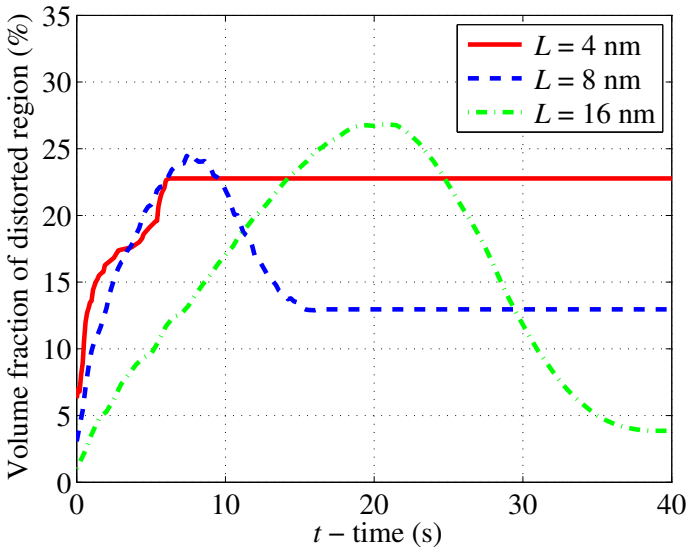

Figure 3.8: Volume fraction of the distorted region, using $|\epsilon_{yz}| > 0.01$ as the criterion.

is comparatively less well-understood and has come under investigation only recently. In this regard, recent experimental studies have revealed several coupled deformation-diffusion phenomena that occur at atomic spatial resolution, yet evolve over time scales of the order of seconds to minutes. This time scale is beyond present capability of established molecular-dynamics models.

In this paper, we have presented the application of a novel atomistic model, referred to as diffusive molecular dynamics (DMD), to the simulation of the long-term (up to 40 s) hydrogen absorption into Pd nanocubes with edge length ranging from 4 nm to 16 nm. Our DMD solver is parallelized using the PETSc library, and the DMD simulations reported in this study consume up to $7,000$ CPU hours (e.g., 24 hours on 300 CPU cores) on the BlueRidge supercomputer at Virginia Tech. The following findings are noteworthy:

- The process of H absorption into Pd nanocubes is controlled by the propagation of

an atomistically sharp α/β Pd-H phase boundary. During the process, the phase boundary propagates towards the center of the cube, and its shape evolves from a cube to a rounded cube, then gradually morphs into a sphere. At the end of the process, the phase boundary annihilates at the center of the nanocube. The thickness of the phase boundary is found to vary between 0.2 and 1.0 nm, depending on both sample size and the specific time during the absorption process. It is also found that at the final equilibrium state H atoms have an affinity for the boundary and stay preferentially on and near the surface of the nanocube at the expense of the interior.

- A concave-convex inversion of form and shear strain is observed between the initial and final states of the nanocube. Moreover, the initiation and propagation of α/β phase boundary induces local transient lattice distortions, especially in the β phase. The corners of the nanocube become distorted first. Then, the distorted region moves inwards tracking the phase boundary.

The calculations reported in this paper generally portray a picture of deformation-diffusion coupled processes and of complex transients occurring on the second to minute time scale. DMD is instrumental for enabling the characterization of those long and complex transients while ensuring the atomistic fidelity necessary to account for phase transformations, sharp-interface motion, surface/edge/corner effects, and other effects.

A number of questions not addressed in this paper immediately suggest themselves. Given the role played by sharp corners, edges and facets as rate-controlling features, it is of interest

to ascertain generally the effect of nanoparticle shape on H absorption. In addition, the present calculations reveal the development of large lattice distortions during the absorption transient, especially across the moving phase boundary. Those distortions in turn stress the lattice, which begs the question of whether relaxation mechanisms such as point defects or dislocations can be activated and the effect of such relaxation mechanisms on the process of absorption itself. These phenomena are currently under investigation and will be addressed in upcoming publications.

Acknowledgments

The authors gratefully acknowledge the support of the Institute for Critical Technologies and Applied Sciences (ICTAS) at Virginia Tech through a Junior Faculty Collaboration (JFC) project, the Ministerio de Economía y Competitividad of Spain under grant number DPI2015-66534-R, and the U. S. Army Research Laboratory (ARL) through the Materials in Extreme Dynamic Environments (MEDE) Collaborative Research Alliance (CRA) under Award Number W911NF-11-R-0001.

Bibliography

[1] B. Sakintuna, F. Lamari-Darkrim, M. Hirscher, Metal hydride materials for solid hydrogen storage: a review, International Journal of Hydrogen Energy 32 (9) (2007) 1121–1140.

[2] D. Mori, K. Hirose, Recent challenges of hydrogen storage technologies for fuel cell vehicles, International Journal of Hydrogen Energy 34 (10) (2009) 4569–4574.

[3] D. Chartouni, N. Kuriyama, T. Kiyobayashi, J. Chen, Metal hydride fuel cell with intrinsic capacity, International Journal of Hydrogen Energy 27 (9) (2002) 945–952.

[4] M. Łukaszewski, K. Hubkowska, A. Czerwiński, Comparative study on the influence of temperature, electrode potential and alloy bulk composition on hydrogen electrosorption into pd–pt and pd–au alloys, Journal of Electroanalytical Chemistry 651 (2) (2011) 131–142.

[5] D. A. Cogswell, M. Z. Bazant, Theory of coherent nucleation in phase-separating nanoparticles, Nano Letters 13 (7) (2013) 3036–3041.

[6] C. Lebouin, Y. Soldo, S. Grigoriev, M. Guymont, P. Millet, Kinetics of hydrogen sorption by palladium nanoparticles, International Journal of Hydrogen Energy 38 (2) (2013) 966–972.

[7] W. Vogel, W. He, Q.-H. Huang, Z. Zou, X.-G. Zhang, H. Yang, Palladium nanoparticles breathe hydrogen; a surgical view with x-ray diffraction, International Journal of Hydrogen Energy 35 (16) (2010) 8609–8620.

[8] B. D. Adams, A. Chen, The role of palladium in a hydrogen economy, Materials Today 14 (6) (2011) 282–289.

[9] Y. Sakamoto, K. Yuwasa, K. Hirayama, X-ray investigation of the absorption of hydrogen by several palladium and nickel solid solution alloys, Journal of the Less Common Metals 88 (1) (1982) 115–124.

[10] R. Bardhan, L. O. Hedges, C. L. Pint, A. Javey, S. Whitelam, J. J. Urban, Uncovering the intrinsic size dependence of hydriding phase transformations in nanocrystals, Nature Materials 12 (10) (2013) 905–912.

[11] A. Baldi, T. C. Narayan, A. L. Koh, J. A. Dionne, In situ detection of hydrogen-induced phase transitions in individual palladium nanocrystals, Nature Materials 13 (12) (2014) 1143–1148.

[12] G. Li, H. Kobayashi, S. Dekura, R. Ikeda, Y. Kubota, K. Kato, M. Takata, T. Yamamoto, S. Matsumura, H. Kitagawa, Shape-dependent hydrogen-storage properties in pd nanocrystals: which does hydrogen prefer, octahedron (111) or cube (100)?, Journal of the American Chemical Society 136 (29) (2014) 10222–10225.

[13] A. Ulvestad, M. Welland, S. Collins, R. Harder, E. Maxey, J. Wingert, A. Singer, S. Hy, P. Mulvaney, P. Zapol, et al., Avalanching strain dynamics during the hydriding phase

transformation in individual palladium nanoparticles, Nature Communications 6 (2015) 1–8.

[14] B. Amin-Ahmadi, D. Connétable, M. Fivel, D. Tanguy, R. Delmelle, S. Turner, L. Malet, S. Godet, T. Pardoen, J. Proost, et al., Dislocation/hydrogen interaction mechanisms in hydrided nanocrystalline palladium films, Acta Materialia 111 (2016) 253–261.

[15] T. C. Narayan, F. Hayee, A. Baldi, A. L. Koh, R. Sinclair, J. A. Dionne, Direct visualization of hydrogen absorption dynamics in individual palladium nanoparticles, Nature Communications 8 (2017) 14020.

[16] A. Ulvestad, M. Welland, W. Cha, Y. Liu, J. Kim, R. Harder, E. Maxey, J. Clark, M. Highland, H. You, et al., Three-dimensional imaging of dislocation dynamics during the hydriding phase transformation, Nature materials 16 (5) (2017) 565–571.

[17] K. Wang, M. Ortiz, M. P. Ariza, Long-term atomistic simulation of hydrogen diffusion in metals, International Journal of Hydrogen Energy 40 (15) (2015) 5353–5358.

[18] Y. Li, G. Wahnström, Molecular-dynamics simulation of hydrogen diffusion in palladium, Physical Review B 46 (22) (1992) 14528.

[19] R. A. Miron, K. A. Fichthorn, Accelerated molecular dynamics with the bond-boost method, The Journal of Chemical Physics 119 (12) (2003) 6210–6216.

[20] A. F. Voter, Introduction to the kinetic monte carlo method, in: Radiation Effects in Solids, Springer, 2007, pp. 1–23.

[21] R. A. Miron, K. A. Fichthorn, Heteroepitaxial growth of co/ cu (001): An accelerated molecular dynamics simulation study, Physical Review B 72 (3) (2005) 035415.

[22] E. Crespo, S. Claramonte, M. Ruda, S. R. de Debiaggi, Thermodynamics of hydrogen in pd nanoparticles, International Journal of Hydrogen Energy 35 (11) (2010) 6037–6041.

[23] E. A. Crespo, M. Ruda, S. R. de Debiaggi, E. M. Bringa, F. U. Braschi, G. Bertolino, Hydrogen absorption in pd nanoparticles of different shapes, International Journal of Hydrogen Energy 37 (19) (2012) 14831–14837.

[24] S. R. de Debiaggi, E. Crespo, F. Braschi, E. Bringa, M. Ali, M. Ruda, Hydrogen absorption in pd thin-films, International Journal of Hydrogen Energy 39 (16) (2014) 8590–8595.

[25] J. Li, S. Sarkar, W. T. Cox, T. J. Lenosky, E. Bitzek, Y. Wang, Diffusive molecular dynamics and its application to nanoindentation and sintering, Physical Review B 84 (5) (2011) 054103.

[26] S. Sarkar, J. Li, W. T. Cox, E. Bitzek, T. J. Lenosky, Y. Wang, Finding activation pathway of coupled displacive-diffusional defect processes in atomistics: Dislocation climb in fcc copper, Physical Review B 86 (1) (2012) 014115.

[27] G. Venturini, K. Wang, I. Romero, M. P. Ariza, M. Ortiz, Atomistic long-term simulation of heat and mass transport, Journal of the Mechanics and Physics of Solids 73 (2014) 242–268.

[28] G. Simpson, M. Luskin, D. J. Srolovitz, A theoretical examination of diffusive molecular dynamics, SIAM Journal on Applied Mathematics 76 (6) (2016) 2175–2195.

[29] X. Sun, M. P. Ariza, K. Wang, Deformation-diffusion coupled analysis of long-term hydrogen diffusion in nanofilms, in: Proceedings of VII European Congress on Computational Methods in Applied Sciences and Engineering, Vol. 1, ECCOMAS, 2016, pp. 197–208.

[30] X. Sun, M. P. Ariza, M. Ortiz, K. Wang, Acceleration of diffusive molecular dynamics simulations through mean field approximation and subcycling time integration, Journal of Computational Physics 350 (2017) 470–492.

[31] M. P. Ariza, I. Romero, M. Ponga, M. Ortiz, Hotqc simulation of nanovoid growth under tension in copper, International Journal of Fracture 174 (1) (2012) 75–85.

[32] E. Dontsova, J. Rottler, C. Sinclair, Solute-defect interactions in al-mg alloys from diffusive variational gaussian calculations, Physical Review B 90 (17) (2014) 174102.

[33] J. P. Mendez, M. Ponga, M. Ortiz, Diffusive molecular dynamics simulations of lithiation of silicon nanopillars, Journal of the Mechanics and Physics of Solids.

[34] X. Zhou, J. A. Zimmerman, B. M. Wong, J. J. Hoyt, An embedded-atom method interatomic potential for pd–h alloys, Journal of Materials Research 23 (03) (2008) 704–718.

[35] E. T. Jaynes, Information theory and statistical mechanics i, Physical Review 106 (4) (1957) 620–630.

[36] E. T. Jaynes, Information theory and statistical mechanics ii, Physical Review 108 (2) (1957) 171–190.

[37] Y. Kulkarni, J. Knap, M. Ortiz, A variational approach to coarse graining of equilibrium and non-equilibrium atomistic description at finite temperature, Journal of the Mechanics and Physics of Solids 56 (4) (2008) 1417–1449.

[38] B. Gonzalez-Ferreiro, I. Romero, M. Ortiz, A numerical method for the time coarsening of transport processes at the atomistic scale, Modelling and Simulation in Materials Science and Engineering 24 (4) (2016) 045011.

[39] B. A. Farmer, M. Luskin, P. Plecháč, G. Simpson, Spin-diffusions and diffusive molecular dynamics, arXiv preprint arXiv:1702.01469.

[40] J. D. Head, M. C. Zerner, A broyden-fletcher-goldfarb-shanno optimization procedure for molecular geometries, Chemical Physics Letters 122 (3) (1985) 264 – 270.

[41] S. Balay, S. Abhyankar, M. F. Adams, J. Brown, P. Brune, K. Buschelman, L. Dalcin, V. Eijkhout, W. D. Gropp, D. Kaushik, M. G. Knepley, L. C. McInnes, K. Rupp, B. F. Smith, S. Zampini, H. Zhang, H. Zhang, PETSc users manual, Tech. Rep. ANL-95/11 - Revision 3.7, Argonne National Laboratory (2016).
URL `http://www.mcs.anl.gov/petsc`

[42] Webpage for BlueRidge (Sandy Bridge), https://secure.hosting.vt.edu/www.arc.vt.edu/computing/blueridge-sandy-bridge/.

[43] H. Okuyama, W. Siga, N. Takagi, M. Nishijima, T. Aruga, Path and mechanism of hydrogen absorption at pd (100), Surface Science 401 (3) (1998) 344–354.

[44] A. Zalineeva, S. Baranton, C. Coutanceau, G. Jerkiewicz, Octahedral palladium nanoparticles as excellent hosts for electrochemically adsorbed and absorbed hydrogen, Science Advances 3 (2) (2017) e1600542.

[45] T. C. Narayan, A. Baldi, A. L. Koh, R. Sinclair, J. A. Dionne, Reconstructing solute-induced phase transformations within individual nanocrystals, Nature Materials 15 (7) (2016) 768–774.

[46] C. Sachs, A. Pundt, R. Kirchheim, M. Winter, M. Reetz, D. Fritsch, Solubility of hydrogen in single-sized palladium clusters, Physical Review B 64 (7) (2001) 075408.

[47] C. Lemier, J. Weissmüller, Grain boundary segregation, stress and stretch: effects on hydrogen absorption in nanocrystalline palladium, Acta Materialia 55 (4) (2007) 1241–1254.

[48] A. Stukowski, Visualization and analysis of atomistic simulation data with ovito–the open visualization tool, Modelling and Simulation in Materials Science and Engineering 18 (1) (2009) 015012.

[49] M. Ruda, E. Crespo, S. R. de Debiaggi, Atomistic modeling of h absorption in pd nanoparticles, Journal of Alloys and Compounds 495 (2) (2010) 471–475.

[50] A. Stukowski, A. Arsenlis, On the elastic–plastic decomposition of crystal deformation at the atomic scale, Modelling and Simulation in Materials Science and Engineering 20 (3) (2012) 035012.

Chapter 4

Atomistic Modeling and Analysis of Hydride Phase Transformation in Palladium Nanoparticles

(Submitted to *Journal of the Mechanics and Physics of Solids*.)

X. Sun [a], M. P. Ariza [b], M. Ortiz [c], K. G. Wang [a]

[a] Department of Aerospace and Ocean Engineering, Virginia Polytechnic Institute and State University, Blacksburg, VA 24061, United States

[b] Escuela Técnica Superior de Ingeniería, Universidad de Sevilla, Sevilla 41092, Spain

[c] Division of Engineering and Applied Science, California Institute of Technology, Pasadena, CA 91125, United States

Abstract

Palladium-hydrogen (Pd-H) is a prototypical system for studying solute-induced phase transformation in various energy conversion and storage applications. While the behaviors of bulk Pd-H have been studied extensively, the detailed atomic picture of hydride phase transformation within individual Pd nanoparticles is still unclear. In this work, we employ a novel atomistic computational model, referred to as Diffusive Molecular Dynamics (DMD), to characterize the H absorption dynamics in Pd nanoparticles of spherical, octahedral and cubic shapes. The DMD model couples a non-equilibrium thermodynamic model with a discrete diffusion law, which allows it to reach diffusive time scales with atomic resolution. The model is capable of capturing the propagation of an atomistically sharp hydride phase boundary. A remarkable feature of the phase boundary structure that is predicted by the calculations is the emergence of misfit dislocations distributed over the interface. These dislocations relieve the elastic residual stresses induced by the change of volume that accompanies the phase transformation. Shape effects are also investigated in this work. More specifically, in both spherical and octahedral nanoparticles, we observe stacking faults during the H absorption process while the phase boundary in the cubic nanoparticle remains coherent. The spatial distribution of the stacking faults in the spherical sample is investigated in detail using an elastic core-shell model. We also identify the mechanisms that enable the movement of the stacking faults as they track the propagation of the phase boundary. Finally, we find that the rate of H absorption is reduced by the formation and movement of the stacking faults.

Keywords

Hydrogen Absorption, Palladium Nanoparticles, Phase Transformation, Misfit Dislocations, Diffusive Molecular Dynamics

4.1 Introduction

Solute-induced phase transformation is a fundamental process in various energy conversion and storage applications. For example, the operation of lithium-ion batteries relies on a reversible phase transformation in the cathodic material (e. g., Li_xCoO_2, Li_xFePO_4), induced by the diffusion of lithium ions [1, 2]. Similarly, the storage of hydrogen in metals relies on the phase transformation of the hydride (e. g., MgH_x, $NaAlH_x$), induced by the diffusion of hydrogen atoms [3, 4, 5]. For these applications, there has been a continuous push towards nanostructured systems, as they hold promise for accelerating the charging and discharging process, increasing the energy and power density, and extending the life cycle [1, 6, 7, 8].

The palladium-hydrogen (Pd-H) system is a prototypical model for studying solute-induced phase transformation, as it allows for relatively fast reaction kinetics at easily accessible temperatures and pressures [9]. The Pd-H system exhibits two distinct phases at room temperature: the dilute α phase at low H concentration (up to $PdH_{0.015}$), and the β phase at high H concentration ($PdH_{0.6}$ and above). In both phases, the Pd lattice maintains the face-centered cubic (FCC) structure, while the H atoms occupy the octahedral interstitial

sites. Attendant to the α/β phase transformation, there is a lattice expansion with 10.4% increase in volume which may lead to the formation of misfit dislocations.

While the behavior of Pd-H is well-understood in the bulk, the phase transformation dynamics within nanostructured Pd-H systems remains an active area of research [7, 10, 11, 12, 13, 14, 15, 16, 17, 18]. In this regard, a few recent experiments suggest that in nanosized particles, the phase transformation is driven by the propagation of an atomistically sharp phase boundary at a speed as low as 1 nm/s. For example, by scanning transmission electron microscopy (STEM), Narayan *et al.* observed the propagation of a sharp α/β phase boundary in individual Pd nanocubes with edge lengths between 20 nm and 40 nm [16]. Using coherent X-ray diffractive imaging, Ulvestad *et al.* measured the evolution of strain within individual Pd nanocubes between 60 nm and 100 nm, which also indicates a sharp α/β phase transformation [14, 17]. Beyond the overall transformation mechanism, other unresolved issues include the morphology of the phase boundary [11, 16, 17], the effect of particle shape and lattice orientation [12], and the interaction of phase boundary with preexisting defects [15].

In this work, we apply a novel computational method, referred to as Diffusive Molecular Dynamics (DMD), to investigate the detailed dynamics of hydride phase transformation in Pd nanoparticles, focusing on the two-way interaction between the motion of the phase boundary and the formation and evolution of misfit dislocations. DMD is a new paradigm for simulating long-term diffusive mass and heat transport while maintaining full atomic resolution [19, 20, 21, 22, 18, 23, 24, 25, 26, 27, 28]. The basic idea is to couple a calibrated empirical kinetic model for the evolution of lattice site occupancy with a non-equilibrium

statistical thermodynamics model that supplies the requisite driving forces for kinetics. The basic assumption underlying DMD is that the time scale of diffusion is much larger than that of microscopic state transitions. Therefore at an intermediate time scale, the microscopic state variables can be considered as random variables. In comparison to the established atomistic methods (e. g., Molecular Dynamics (MD), transition state theory based accelerated MD [29], and kinetic Monte Carlo [30]), DMD has a larger simulation time window as it does not explicitly resolve thermal vibrations or the individual microscopic state transitions. DMD has been applied to nanoindentation and sintering [19, 23], dislocation extension [24], nanovoid growth [20, 22, 27], heat conduction in nanowires [31] and solute-defect interactions [21, 32]. Recently, DMD has been employed to study the effect of particle size on the hydrogenation process of cubic Pd nanoparticles [33]. A one-dimensional version has also been applied to simulate H diffusion in Pd nanofilms, in which the Pd subsystem was assumed to be rigid [18].

The large time window and atomic resolution of DMD makes it an excellent tool for studying hydride phase transformation within Pd nanoparticles, which unfolds on a time scale of minutes to hours. In this paper, we start with a brief summary of assumptions and model equations underlying DMD, in Section 4.2. Then, we describe the setup of the numerical H absorption experiments under consideration in Section 4.3. Specifically, we consider three nanoparticles of approximately the same volume ($3,800 \pm 90$ nm^3), yet of different shapes, including a spherical particle exemplifying smooth geometries, and an octahedral and a cubic particles that have flat faces and sharp edges and corners. The octahedral particle is designed

such that all of its 8 faces are on {111} planes, which are the most common slip planes in FCC crystals. By contrast, the cubic particle is designed with their faces on {100} planes. Next, we discuss the results of the numerical experiments, including the propagation of the α/β phase boundary (Section 4.4), the attendant dynamics of interfacial misfit dislocations and stacking faults (Section 4.5), and the rate of H absorption (Section 4.6). In order to explain the observed stacking fault distribution, we formulate a simple elastic core-shell model amenable to analytical solution. Finally, we provide a summary and concluding remarks in Section 4.7.

4.2 Methodology

4.2.1 Non-equilibrium thermodynamics model

We consider a binary Pd-H system consisting of host sites that are occupied by Pd atoms and interstitial sites that can be either occupied by H atoms or unoccupied. For ease of reference, the sets of host and interstitial sites are denoted by I_{Pd} and I_{H}, respectively. On each interstitial site $i \in I_{\mathrm{H}}$, we introduce an occupancy function n_i, defined as

$$n_i = \begin{cases} 1 & \text{if the site } i \text{ is occupied by a H atom,} \\ 0 & \text{if the site } i \text{ is unoccupied.} \end{cases} \tag{4.1}$$

The instantaneous position and momentum of site i are denoted by $\boldsymbol{q}_i$ and $\boldsymbol{p}_i$, respectively. Based on the assumption of scale separation and the ergodic hypothesis, these microscopic state variables can be viewed as random variables that have a joint probability distribution characterized by density function $\rho\big(\{\boldsymbol{q}\},\{\boldsymbol{p}\},\{n\}\big)$, where $\{\boldsymbol{q}\}=\{\boldsymbol{q}_i : i\in I_{\mathrm{Pd}}\cup I_{\mathrm{H}}\}$, $\{\boldsymbol{p}\}=\{\boldsymbol{p}_i : i\in I_{\mathrm{Pd}}\cup I_{\mathrm{H}}\}$ and $\{n\}=\{n_i : i\in I_{\mathrm{H}}\}$. We assume that the statistics of the system follows Jaynes' principles of maximum entropy [34, 35]. Therefore, the probability density function ρ is calculated by maximizing the information-theoretical entropy

$$S[\rho]=-k_{\mathrm{B}}\langle\log\rho\rangle, \tag{4.2}$$

with local constraints on each site

$$\begin{cases}\langle h_i\rangle=e_i, & i\in I_{\mathrm{Pd}}\cup I_{\mathrm{H}},\\ \langle n_i\rangle=x_i, & i\in I_{\mathrm{H}},\end{cases} \tag{4.3}$$

where k_{B} is the Boltzmann constant, and $\langle\cdot\rangle$ denotes the expectation operator. Here, h_i, e_i and x_i denote the local Hamiltonian, particle energy and H atomic fraction of site i, respectively. Using the method of Lagrange multipliers, we have

$$\rho=\frac{1}{\Xi}\mathrm{e}^{-\{\beta\}^{\mathrm{T}}\{h\}+\{\gamma\}^{\mathrm{T}}\{n\}}, \tag{4.4}$$

where Ξ is the partition function, and $\{\beta\}$ and $\{\gamma\}$ are Lagrange multipliers. In comparison with equilibrium statistical thermodynamics, Eq. (4.4) can be interpreted as a non-

equilibrium generalization of the Gibbs grand-canonical probability density function. Also, $T_i = 1/(k_{\mathrm{B}}\beta_i)$ and $\mu_i = k_{\mathrm{B}}T_i\gamma_i$ can be defined as the absolute temperature and the chemical potential of atomic site i, respectively.

Since the Hamiltonian h_i is typically a nonlinear function, the exact calculation of the thermodynamic properties (e. g., e_i and Ξ) is generally impossible. Venturini *et al.* [21] proposed an approximation theory, in which the optimization problem is performed within a finite-dimensional trial space $\mathcal{P}_0$, spanned by a pre-specified class of trial Hamiltonians $\{h_0\}$. As a result, maximizing $\mathcal{S}[\rho]$ within $\mathcal{P}_0$ is equivalent to minimizing the mean field free entropy, i. e.,

$$\min_{\{\alpha\}} \ \mathcal{F}\big(\{\beta\},\{\gamma\};\{h_0\}\big) = k_{\mathrm{B}}\{\beta\}^{\mathrm{T}}\big\{\langle h - h_0\rangle_0\big\} - k_{\mathrm{B}}\log\Xi_0, \tag{4.5}$$

where $\{\alpha\}$ is a finite set of parameters that characterize $\{h_0\}$. $\langle\cdot\rangle_0$ denotes the expectation operator under the trial probability density function, and Ξ_0 is the trial partition function. We consider a uniform and constant temperature and apply the approximation theory with a trial Hamiltonian

$$h_{0i}(\boldsymbol{q}_i,\boldsymbol{p}_i,n_i;\ \bar{\boldsymbol{q}}_i,\sigma_i,\bar{\boldsymbol{p}}_i,\gamma_{0i}) = \begin{cases} \dfrac{k_{\mathrm{B}}T}{2\sigma_i^2}|\boldsymbol{q}_i-\bar{\boldsymbol{q}}_i|^2 + \dfrac{1}{2m_{\mathrm{Pd}}}|\boldsymbol{p}_i-\bar{\boldsymbol{p}}_i|^2, & \text{if } i\in I_{\mathrm{Pd}}, \\ \dfrac{k_{\mathrm{B}}T}{2\sigma_i^2}|\boldsymbol{q}_i-\bar{\boldsymbol{q}}_i|^2 + \dfrac{1}{2m_{\mathrm{H}}}|\boldsymbol{p}_i-\bar{\boldsymbol{p}}_i|^2 - k_{\mathrm{B}}T\gamma_{0i}n_i, & \text{if } i\in I_{\mathrm{H}}, \end{cases} \tag{4.6}$$

where T is the constant temperature. $\bar{\boldsymbol{q}}_i$, σ_i, $\bar{\boldsymbol{p}}_i$, and γ_{0i} are parameters that characterize the trial space. m_{Pd} and m_{H} denote the atomic mass of Pd and H, respectively. It can be shown that $\bar{\boldsymbol{q}}_i$ and σ_i are the mean and standard deviation of $\boldsymbol{q}_i$, respectively, whereas $\bar{\boldsymbol{p}}_i$ is the

mean of $\boldsymbol{p}_i$. In Eq. (4.6), γ_{0i} indicates the dependence of chemical potential on H fraction x_i. Specifically, applying $\langle n_i \rangle_0 = x_i$ yields

$$\gamma_{0i} = \log \frac{x_i}{1 - x_i} - \gamma_i. \tag{4.7}$$

Substituting Eqs. (4.6) and (4.7) into Eq. (4.5) gives

$$\begin{aligned}
&\min_{\{\bar{\boldsymbol{q}}\},\{\sigma\},\{\bar{\boldsymbol{p}}\},\{x\}} \mathcal{F}\big(T, \{\gamma\}; \{\bar{\boldsymbol{q}}\}, \{\sigma\}, \{\bar{\boldsymbol{p}}\}, \{x\}\big) \\
&= \frac{1}{T}\langle V \rangle_0 + \frac{1}{2Tm_{\mathrm{Pd}}} \sum_{i \in I_{\mathrm{Pd}}} \bar{\boldsymbol{p}}_i^2 + \frac{1}{2Tm_{\mathrm{H}}} \sum_{i \in I_{\mathrm{H}}} x_i \bar{\boldsymbol{p}}_i^2 + \frac{3}{2} k_{\mathrm{B}} \sum_{i \in I_{\mathrm{Pd}}} \left(\log \frac{\hbar^2}{k_{\mathrm{B}} T m_{\mathrm{Pd}} \sigma_i^2} - 1 \right) \\
&+ \frac{3}{2} k_{\mathrm{B}} \sum_{i \in I_{\mathrm{H}}} \left(\log \frac{\hbar^2}{k_{\mathrm{B}} T m_{\mathrm{H}} \sigma_i^2} + x_i - 2 \right) + k_{\mathrm{B}} \sum_{i \in I_{\mathrm{H}}} \big(x_i \log x_i + (1 - x_i) \log (1 - x_i) - \gamma_i x_i \big),
\end{aligned} \tag{4.8}$$

where $\hbar$ is the reduced Planck constant. $V\big(\{\boldsymbol{q}\}, \{n\}\big)$ denotes the interatomic potential energy and its average is calculated by third-order Gaussian quadratures on a sparse grid [19]. Enforcing the first-order necessary condition with respect to $\bar{\boldsymbol{p}}_i$ yields $\bar{\boldsymbol{p}}_i = \boldsymbol{0}$. Enforcing the first-order necessary condition with respect to x_i yields

$$\gamma_i = \frac{3}{2} + \log \frac{x_i}{1 - x_i} + \frac{1}{k_{\mathrm{B}} T} \frac{\partial \langle V \rangle_0}{\partial x_i}, \quad i \in I_{\mathrm{H}}, \tag{4.9}$$

which shows that the atomic chemical potential depends on both the atomic H fraction and

the interatomic potential energy. As a result, the optimization problem simplifies to

$$\begin{aligned}
&\min_{\{\bar{\boldsymbol{q}}\},\{\sigma\}} \mathcal{F}\big(T,\{\gamma\};\{\bar{\boldsymbol{q}}\},\{\sigma\},\{x\}\big) \\
&= \frac{1}{T}\langle V\rangle_0 + \frac{3}{2}k_{\mathrm{B}}\sum_{i\in I_{\mathrm{Pd}}}\left(\log\frac{\hbar^2}{k_{\mathrm{B}}Tm_{\mathrm{Pd}}\sigma_i^2}-1\right) + \frac{3}{2}k_{\mathrm{B}}\sum_{i\in I_{\mathrm{H}}}\left(\log\frac{\hbar^2}{k_{\mathrm{B}}Tm_{\mathrm{H}}\sigma_i^2}+x_i-2\right) \\
&+ k_{\mathrm{B}}\sum_{i\in I_{\mathrm{H}}}\big(x_i\log x_i+(1-x_i)\log(1-x_i)-\gamma_i x_i\big).
\end{aligned} \tag{4.10}$$

4.2.2 Discrete diffusion model

The thermodynamics model formulated in Eq. (4.10) is then coupled with a discrete kinetic law, which enforces the balance of mass at each interstitial site, i. e.,

$$\dot{x}_i = \sum_{j\neq i} J_{ij}, \quad i,j\in I_{\mathrm{H}}, \tag{4.11}$$

where J_{ij} denotes the *bondwise* mass flux from site j to site i, and satisfies $J_{ij}=-J_{ji}$. After a straightforward calculation, the internal entropy production rate from a pair of sites $\langle i,j\rangle$ is

$$\Sigma_{ij} = K_{ij}J_{ij}, \tag{4.12}$$

where

$$K_{ij} = -\frac{1}{T}(\mu_i-\mu_j) = -k_{\mathrm{B}}(\gamma_i-\gamma_j) \tag{4.13}$$

defines the discrete thermodynamic force corresponding to the discrete mass transport J_{ij}. Following Onsager's theory of kinetic relations [36], we employ a kinetic law of the general

form

$$J_{ij} = -\frac{\partial \psi}{\partial K_{ij}}\big(\{K\}\big), \tag{4.14}$$

where $\psi\big(\{K\}\big)$ is a discrete kinetic potential, which needs to be modeled. Venturini *et al.* [21] proposed a simple kinetic potential, by assuming linear relation between mass flux J_{ij} and driving force K_{ij}. The resulting discrete mass transport J_{ij} is

$$J_{ij} = B_0 \frac{x_i + x_j}{2} K_{ij}, \tag{4.15}$$

where B_0 denotes the bondwise diffusion coefficient, which can be calibrated to reproduce the speed of diffusion observed in experiments. As a result, we have

$$\dot{x}_i = -k_{\mathrm{B}} B_0 \sum_{j \neq i} \frac{x_i + x_j}{2} (\gamma_i - \gamma_j), \quad i, j \in I_{\mathrm{H}}. \tag{4.16}$$

For simplicity, but without loss of generality, in our DMD simulations we restrict diffusive transport within one shell of neighbors. The above discrete kinetic law has been validated against the classical lattice random walk model for the long-term dynamics of a single H atom in Pd [37]. It has also been applied to study surface segregation in AuAg alloys [38]. Moreover, similar bondwise flux functions have been employed to simulate spin-diffusion in a one-dimensional binary alloy [39].

4.2.3 Implementation details

Our DMD model couples a nonlinear optimization problem, i. e., Eq. (4.10), with a first-order, nonlinear ordinary differential equation (ODE), i. e., Eq. (4.16). We solve this coupled system by discretizing the ODE using an explicit time integrator (e. g., forward-Euler), and solving the optimization problem once per time step using a quasi-Newton Broyden-Fletcher-Goldfarb-Shanno (BFGS) method [40]. We have developed a DMD solver, which is parallelized with Message Passing Interface (MPI), using the PETSc/TAO library [41] for large-scale simulations on computer clusters with distributed memory. Details of the solutions of the equations and the computation procedure of DMD can be found in Ref. [37].

4.3 Setup of numerical experiments

We build three nanoparticles of different shapes, including a sphere, an octahedron with faces on {111} planes, and a cube with faces on {100} planes. The three particles are designed to have approximately the same volume, that is, $3,800 \pm 90$ nm^3 and $516,000 \pm 8,000$ atomic sites (including the octahedral interstitial sites that can be occupied by H atoms). The sphere has a diameter of 19.5 nm. The octahedron and the cube have an edge length of 19.9 nm and 15.6 nm, respectively. As an example, Fig. 4.1 shows the computational model of the spherical particle. All the three particles are single crystals.

Under a gas-phase condition, the absorption of H_2 by Pd begins with the dissociation of

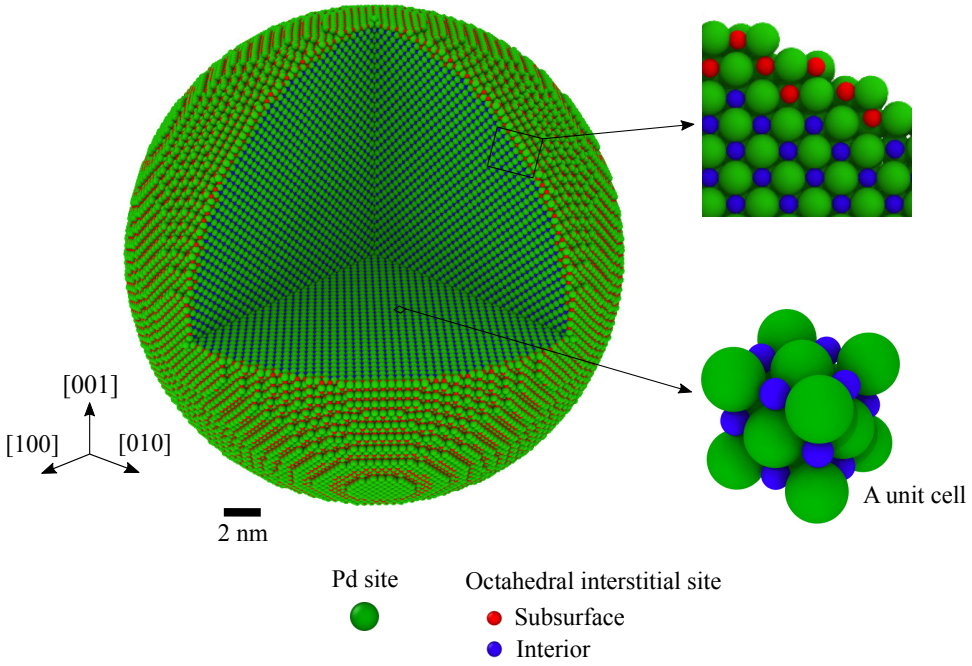

Figure 4.1: Computational model of the spherical particle with a diameter of 19.5 nm.

H_2 into H atoms on the surface of the Pd specimen (i. e., adsorption). The H atoms penetrate into a subsurface layer, then move into the interior of the Pd specimen, occupying the octahedral interstitial sites of the FCC lattice [42, 13, 43]. Palladium hydride (Pd-H) exists in two phases, namely a low H concentration α phase and a high H concentration β phase. Both phases have an FCC lattice, with different lattice constants (3.895 Å versus 4.025 Å [44]). Previous studies suggest that the H_2 partial pressure required to achieve subsurface saturation is lower than that required to initiate the α/β phase transformation in the interior [45, 46, 47]. Also, the saturation of H in the subsurface layer is achieved much faster than the diffusion of H into the interior of a Pd specimen. Therefore, in our DMD analysis, we simulate these two processes separately in two steps, as described in Algorithm 3.

Specifically, we assume that the Pd particle is subjected to a constant H_2 partial pressure,

Algorithm 3 Solution of the DMD equations in the two-step calculation.

Input: $\{x_i^0 : i \in I_{\mathrm{INT}}\}$ (initial H fractions in the interior), $\mu_{\mathrm{env}} = k_{\mathrm{B}}T\gamma_{\mathrm{env}}$ (environmental chemical potential)
Begin
First step: with $\{x_i^0 : i \in I_{\mathrm{INT}}\}$ fixed
Fixed-Point Iteration: set $\{x_i^0 : i \in I_{\mathrm{SURF}}\}$ (initial guess of H fractions in the subsurface layer)
for $l \leftarrow 0;\ l < l_{\max}$ **do**
    $\{x\}^l \leftarrow \{x_i^l : i \in I_{\mathrm{SURF}}\} \cup \{x_i^0 \in I_{\mathrm{INT}}\}$
    minimize $\mathcal{F}\big(\{\bar{\boldsymbol{q}}\}, \{\sigma\}, \{x\}^l\big) \Rightarrow \{\bar{\boldsymbol{q}}\}^l, \{\sigma\}^l$
    $$x_i^{l+1} \leftarrow \frac{\exp\left(\gamma_{\mathrm{env}} - \frac{3}{2} - \frac{1}{k_{\mathrm{B}}T}\frac{\partial\langle V\rangle_0}{\partial x_i}\Big|^l\right)}{1 + \exp\left(\gamma_{\mathrm{env}} - \frac{3}{2} - \frac{1}{k_{\mathrm{B}}T}\frac{\partial\langle V\rangle_0}{\partial x_i}\Big|^l\right)}, \quad \forall i \in I_{\mathrm{SURF}}$$
    if $\sum_{i \in I_{\mathrm{SURF}}} \left(x_i^{l+1} - x_i^l\right)^2 < \epsilon_1$ **then**
        break
    end if
    $l \leftarrow l + 1$
end for
Output: the final results, i. e., $\{x_i^* : i \in I_{\mathrm{SURF}}\},\ \{\bar{\boldsymbol{q}}\}^*,\ \{\sigma\}^*$

Second step: with $\{x_i^* : i \in I_{\rm SURF}\}$ and $\{\gamma_i \leftarrow \gamma_{\rm env} : i \in I_{\rm SURF}\}$ fixed
$t = 0,\ n = 0$
$\{\bar{\boldsymbol{q}}\}^0 \leftarrow \{\bar{\boldsymbol{q}}\}^*,\ \{\sigma\}^0 \leftarrow \{\sigma\}^*$
while $t < t_{\max}$ **do**
    Temporal Integration: with $\{\bar{\boldsymbol{q}}\}^n$ and $\{\sigma\}^n$ fixed, solve Eq. (4.16) by forward-Euler $\Rightarrow \{x\}^{n+1}$
    Begin
        $$\gamma_i^n \leftarrow \frac{3}{2} + \log\frac{x_i^n}{1-x_i^n} + \frac{1}{k_{\rm B}T}\frac{\partial\langle V\rangle_0}{\partial x_i}\bigg|^n, \quad \forall i \in I_{\rm INT}$$
        $\{\gamma\}^n \leftarrow \{\gamma_i^n : i \in I_{\rm INT}\} \cup \{\gamma_i \leftarrow \gamma_{\rm env} : i \in I_{\rm SURF}\}$
        solve Eq. (4.16) for one time-step, i. e.,
        $$x_i^{n+1} \leftarrow x_i^n - k_{\rm B}B_0\Delta t \sum_{j\in I_{\rm H}, j\neq i} \frac{1}{2}(x_i^n + x_j^n)(\gamma_i^n - \gamma_j^n), \quad \forall i \in I_{\rm INT}$$
        $\{x\}^{n+1} \leftarrow \{x_i^{n+1} : i \in I_{\rm INT}\} \cup \{x_i^* : i \in I_{\rm SURF}\}$
    End
    Optimization: with $\{x\}^{n+1}$ fixed, solve Eq. (4.10) by BFGS $\Rightarrow \{\bar{\boldsymbol{q}}\}^{n+1}, \{\sigma\}^{n+1}$
    Begin
        $\boldsymbol{X} \equiv \big\{\{\bar{\boldsymbol{q}}\}, \{\sigma\}\big\}$
        $\mathcal{F}(\boldsymbol{X}) \equiv \mathcal{F}\big(\{\bar{\boldsymbol{q}}\}, \{\sigma\}, \{x\}^{n+1}\big)$
        for $k \leftarrow 0, \boldsymbol{X}^0 \leftarrow \big\{\{\bar{\boldsymbol{q}}\}^n, \{\sigma\}^n\big\};\ k < k_{\max}$ **do**
            compute approximate Hessian matrix $\mathcal{H}^k$
            $\Delta\boldsymbol{X} \leftarrow -(\mathcal{H}^k)^{-1}\nabla\mathcal{F}(\boldsymbol{X}^k)$
            determine step size τ by line search
            $\boldsymbol{X}^{k+1} \leftarrow \boldsymbol{X}^k + \tau\Delta\boldsymbol{X}$
            if $\big|\mathcal{F}(\boldsymbol{X}^{k+1}) - \mathcal{F}(\boldsymbol{X}^k)\big| < \epsilon_2$ or $\dfrac{\big|\mathcal{F}(\boldsymbol{X}^{k+1}) - \mathcal{F}(\boldsymbol{X}^k)\big|}{\big|\mathcal{F}(\boldsymbol{X}^k)\big|} < \epsilon_3$ **then**
                break
            end if
            $k \leftarrow k + 1$
        end for
    End
    $t \leftarrow t + \Delta t,\ n \leftarrow n + 1$
end while
Output: the results at each time step, i. e., $\{\bar{\boldsymbol{q}}\}^n,\ \{\sigma\}^n,\ \{x\}^n,\ \{\gamma\}^n$
End

and hence a constant external chemical potential μ_{env}. In the first step of the analysis, we determine the distribution of H in the subsurface layer and the resulting lattice deformation of the particle, when this layer has just reached equilibrium with the external H environment. To this end, we set $\gamma_i = \mu_{\text{env}}/(k_{\text{B}}T)$ (i. e., $\mu_i = \mu_{\text{env}}$) for all the interstitial sites within the subsurface layer and $x_i = 0$ for all the interstitial sites in the interior of the particle. Then, we solve Eq. (4.9) using fixed-point iteration, to obtain the equilibrium distribution of x_i within the subsurface layer, and minimize the free entropy in Eq. (4.10) to obtain the values of $\{\bar{\boldsymbol{q}}\}$ and $\{\sigma\}$ in the particle.

Next, we assume that throughout the H absorption process, the subsurface layer remains in equilibrium with the external H environment. Therefore, in the second step, we fix $\gamma_i = \mu_{\text{env}}/(k_{\text{B}}T)$ and x_i (obtained in the first step) in the subsurface layer, and apply the dynamic, deformation-diffusion coupled DMD model to predict the diffusion of H from the subsurface to the interior of the Pd particles.

We employ the embedded atom method (EAM) potential developed by Zhou *et al.* [48], which is capable of capturing the separation of α and β phases [18]. We set temperature $T = 300$ K. The thickness of the subsurface layer, denoted by τ, has been estimated to be of the order of 0.1 nm to 1 nm — for example, 0.3 nm using an equilibrium Monte Carlo method [49] and 1.03 nm using a phase-field model [50]. In this work, we set $\tau = 0.3$ nm. Moreover, the functional relationship between the H_2 partial pressure and the corresponding chemical potential μ_{env} is unclear. We have conducted a parameter study, and found that the α/β phase transformation is achieved when $\mu_{\text{env}} > -2.25$ eV. The results presented in this paper

are obtained with $\mu_{\text{env}} = -2.0$ eV, and in this case we get full coverage, i. e., $x_i = 1$, over the subsurface layer in all the three particles after the first step calculation. Further, we have calibrated the atomic diffusivity coefficient B_0 to reproduce the experimental measurement of the speed of H absorption obtained in a similar setting [16], which yields $B_0 = 500.0$ K/(eV·s). The simulation results in the absorption process, i. e., the second step of DMD analysis, will be discussed in detail in the following sections.

The DMD analyses presented in this paper are performed using the BlueRidge supercomputer (Cray CS-300, with Intel Sandy Bridge CPUs) at Virginia Tech [51]. Each analysis consumes approximately $80,000$ CPU hours. The simulation results are visualized using OVITO [52].

4.4 Propagation of phase boundary

We begin by examining the diffusion of H during the absorption process. Figure 4.2 presents the result for the spherical particle. At 4.5 s, a spherical shell with high H concentration — corresponding to the β phase of Pd-H — has formed under the surface of the particle. By contrast, the interior of the particle still has low H concentration (close to 0), which can be interpreted as the α phase. The α and β phases are separated by a sharp boundary consisting of only a few layers of atomic sites, with a thickness of approximately 0.5 nm. This phase boundary is extracted and visualized at three different time instances. At the beginning (e. g., 4.5 s), it has a spherical shape. As time increases, the phase boundary propagates towards the center of the particle, and gradually deforms into a polyhedron with

8 triangular faces and 6 square faces (i. e., a cuboctahedron). The triangular and square faces have normals in ⟨111⟩- and ⟨100⟩-directions, respectively.

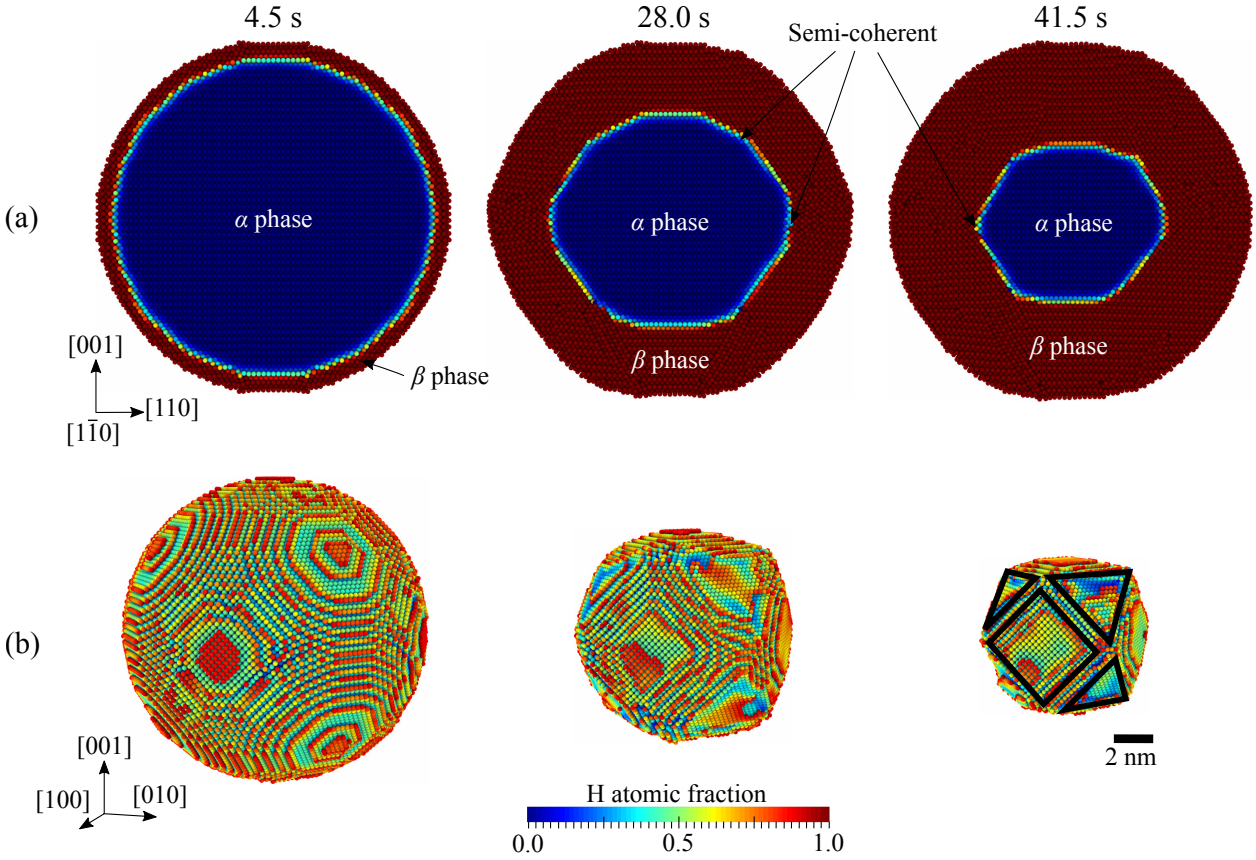

Figure 4.2: Hydride phase boundary in the spherical particle at three different time instances: (a) H fraction on the middle [1$\bar{1}$0] cross-section, and (b) a perspective view of the extracted phase boundary.

The morphological evolution of the phase boundary indicates that H atoms "move" slower along the radial lines that pass through the corners and edges of the polyhedron. Notably, misfit dislocations are also observed near these geometric singularities (the result will be discussed in the next section). Therefore, it is likely that the misfit dislocations have slowed down the propagation of the phase boundary. This can be explained by the fact that a semi-coherent phase boundary leads to less space in the α phase Pd lattice compared to a

coherent one. This mechanism is schematically illustrated in Fig. 4.3.

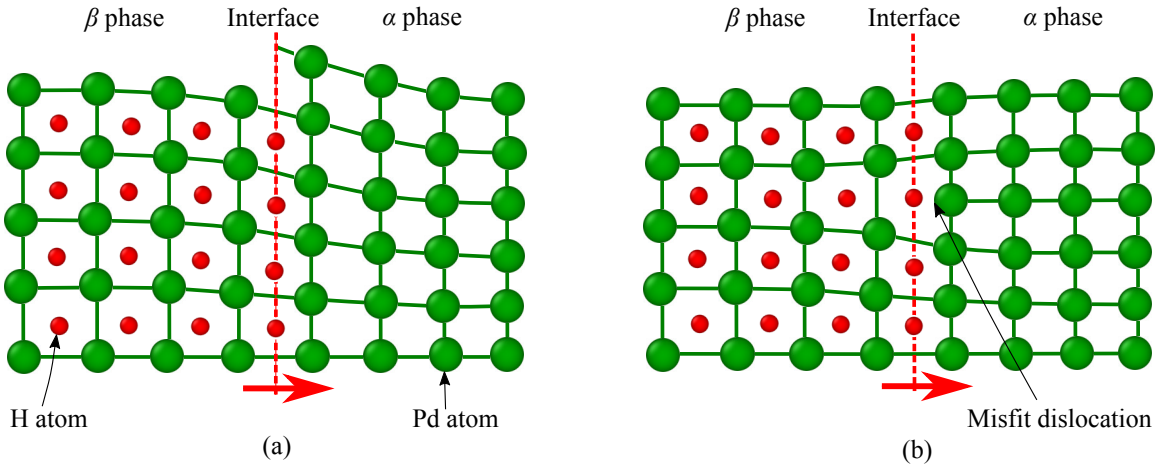

Figure 4.3: Schematic illustration of (a) a coherent and (b) a semi-coherent hydride phase boundary.

Figures 4.4 and 4.5 present the results for the octahedral and cubic particles, respectively. In these two particles, we also observe the formation of an atomistically sharp α/β phase boundary, which advances towards the center of the particle. The shape of the phase boundary changes in time. In the octahedral particle, the phase boundary evolves from a sharp octahedron into a truncated one. The locations of sharp edges retained in the truncated octahedron coincide with the locations of misfit dislocations, which again indicates that misfit dislocations may slow down H diffusion. On the other hand, misfit dislocation is not observed in the cubic particle. In this case, the phase boundary changes gradually from a cube to a sphere. In other words, the sharp corners and edges of the initial phase boundary are gradually smeared. This can be explained as a mechanism to minimize the interfacial energy of the phase boundary.

For all the three different shapes, the DMD analysis indicates that the H absorption process is

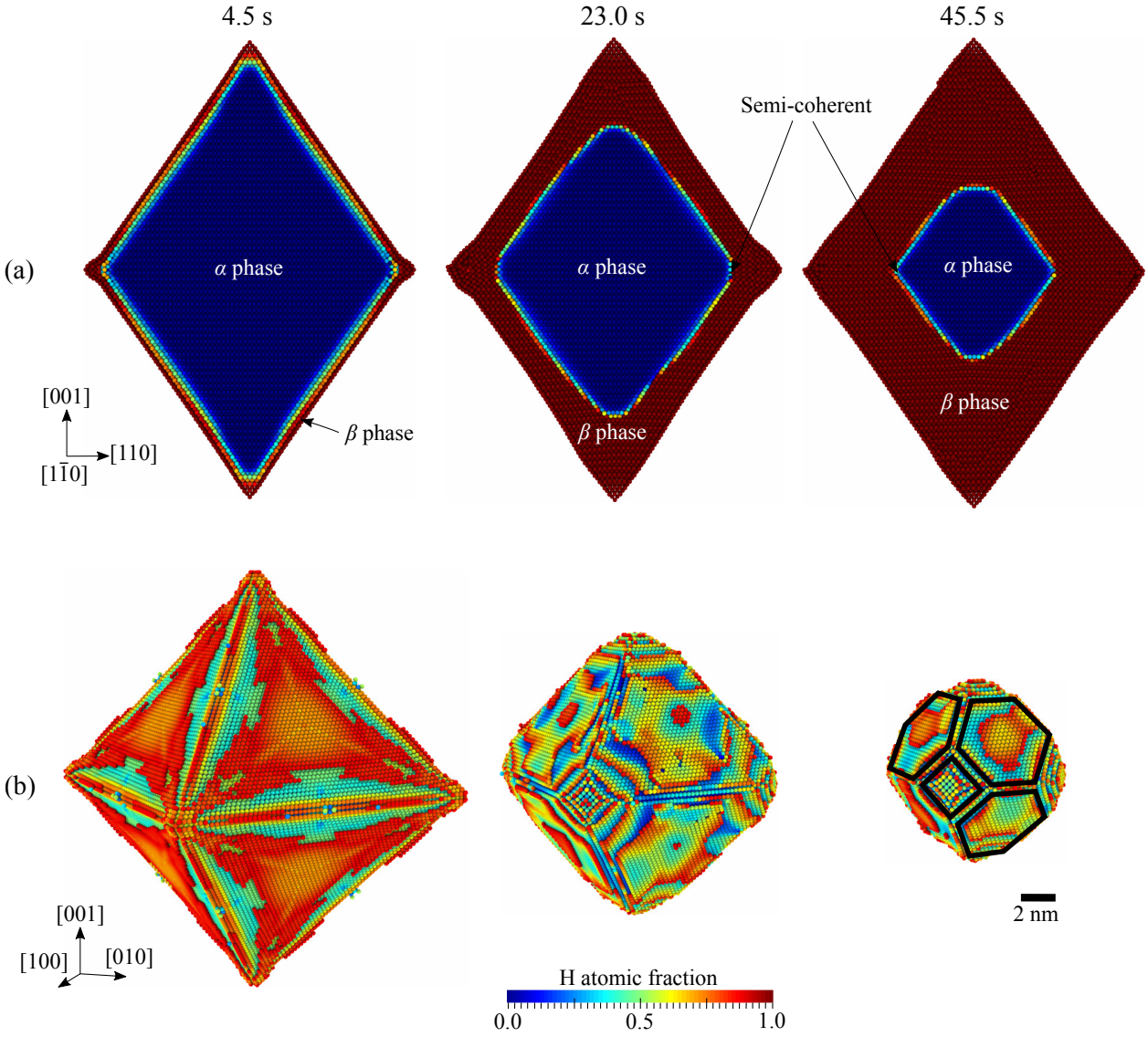

Figure 4.4: Hydride phase boundary in the octahedral particle at three different time instances: (a) H fraction on the middle [1$\bar{1}$0] cross-section, and (b) a perspective view of the extracted phase boundary.

dominated by the formation and propagation of an atomistically sharp α/β phase boundary. This prediction agrees with the findings of a few recent experimental studies on individual Pd particles [16, 14]. Specifically, Narayan *et al.* [16] tested nanocubes with edge length between 20 nm and 40 nm, and observed sharp diffraction contrast in STEM (scanning transmission

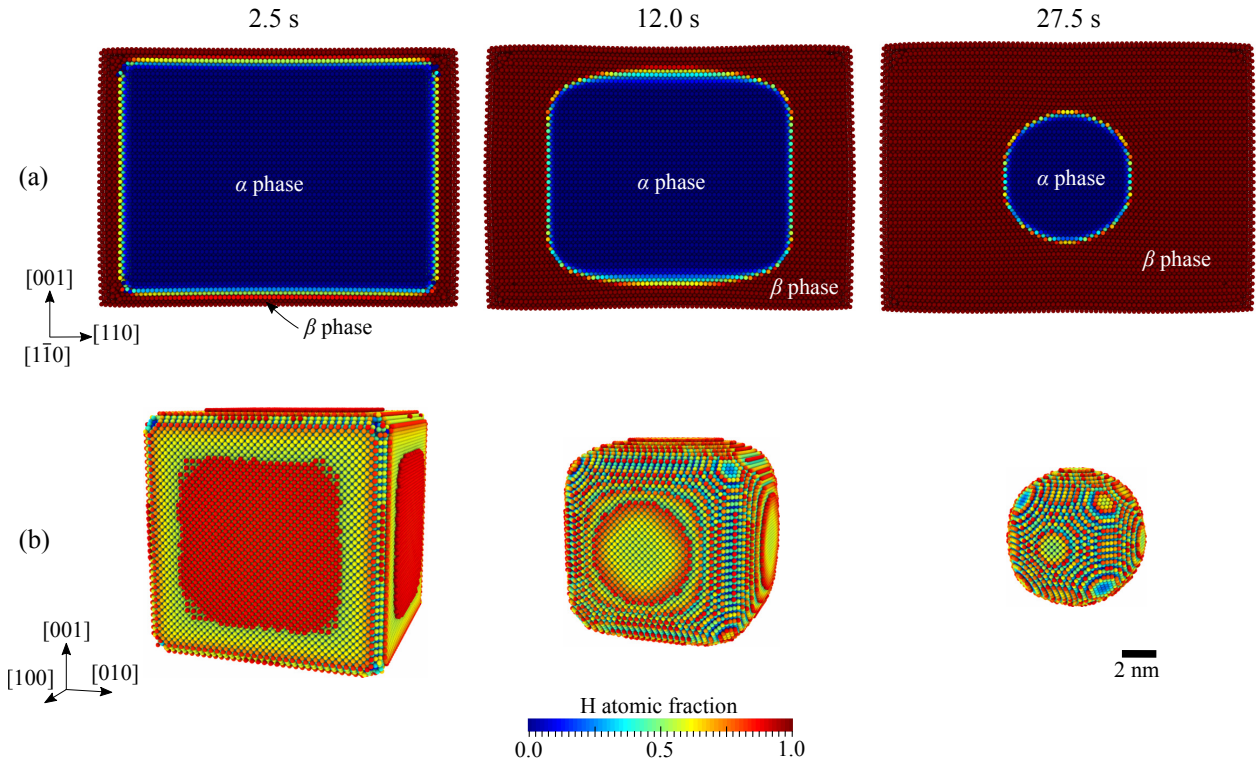

Figure 4.5: Hydride phase boundary in the cubic particle at three different time instances: (a) H fraction on the middle [1$\bar{1}$0] cross-section, and (b) a perspective view of the extracted phase boundary.

electron microscopy) images. Ulvestad *et al.* [14] also tested nanocubs with edge lengths between 60 nm and 100 nm, and observed the disappearance of Bragg electron density in a region from the density field of the Pd nanoparticles.

The separation of α and β phases by a sharp interface can be explained using the equilibrium relation between the chemical potential and the H atomic fraction. Figure 4.6 plots this equilibrium relation, using the EAM potential of Zhou *et al.* [48] and Eq. (4.9). The chemical potential function has two local extrema: one at a low H fraction of 0.25, the other at a high H fraction of 0.81. These two extreme values can be interpreted as the critical concentrations for the α and β phases of Pd-H, predicted by the specific interatomic potential. Since the

H absorption is driven by the difference of chemical potential between different phases, this feature of double extrema likely leads to the formation and propagation of the sharp phase boundary. Further, the chemical potential can also be related to the pressure of H_2 gas. In this regard, the profile of the chemical potential function is consistent with the pressure-composition isotherms obtained for individual single-crystalline Pd nanoparticles [53, 54, 11], which show an abrupt phase transformation from α to β phase.

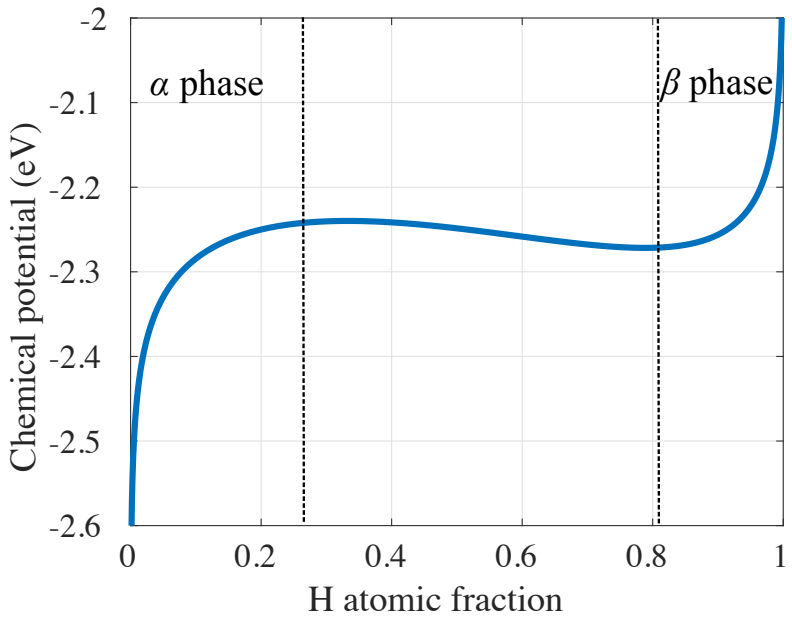

Figure 4.6: Equilibrium relation between chemical potential and H atomic fraction, calculated using the EAM potential of Zhou *et al.* [48] and the DMD model for bulk Pd-H with a uniform H atomic fraction.

4.5 Solute-induced stacking faults

We proceed to examine the Pd lattice deformation induced by the sharp α/β phase boundary. Specifically, we first explain the formation and dynamics of stacking faults in the spherical

particle. Then, we compare with the octahedral and cubic particles to explain the effect of particle shape.

4.5.1 Stacking faults in the spherical nanoparticle

Formation and spatial distribution

Stacking faults start to form on the surface of the particle at approximately 0.5 s, when the thickness of the β phase shell is approximately 0.5 nm. Figure 4.7(a) shows the structure of stacking faults at 4.5 s, obtained using the method of common neighbor analysis [55]. Most of the stacking faults appear in two sets of crystallographically equivalent regions. The first set, referred to as the $\langle 100 \rangle$-centered regions, are spherical sectors with axes in $\langle 100 \rangle$ directions and an apex angle of about 40°. The second group, referred to as the $\langle 110 \rangle$-centered regions, are spherical sectors with axes in $\langle 110 \rangle$ directions and an apex angle of about 50°. In each $\langle 100 \rangle$-centered region, four stacking faults are emitted along four different $\{111\}$ slip planes at 109.5° angle. In each $\langle 110 \rangle$-centered region, around twelve stacking faults are emitted along two sets of parallel $\{111\}$ planes.

To explain the observed distribution pattern, we consider an elastic core-shell model, consisting of a spherical core with radius r_0, elastically matched to a concentric spherical shell whose inner surface has a radius R_0 that is greater than r_0. We set $R_0/r_0 = 1.059$, basing on the lattice expansion of Pd-H from α to β phase. Therefore, the core and the shell are comparable, respectively, with the α phase core and the β phase shell observed in the DMD

simulation. The model equations and the solution process are presented in 4.A. In particular, after obtaining the equilibrium state, we calculate the resolved shear stress (RSS) on the 12 slip systems of FCC crystals.

Figure 4.7(b) shows the maximum RSS among all the 12 slip systems, calculated on the core-shell interface using Eq. (4.36). The distribution of maximum RSS is clearly nonuniform. The global maximum value is 3.92 GPa, higher than the critical resolved shear stress (CRSS) of Pd-H[1]. Comparing with the result of the DMD simulation (Fig. 4.7(a)), we find that the regions where large values of maximum RSS appear coincide with the regions where stacking faults are observed. Moreover, within these regions, the slip system with highest RSS also matches the fault plane of the stacking faults observed in the DMD simulation.

For a clearer comparison, Fig. 4.8 shows the results of both DMD and the core-shell model on the middle $[1\bar{1}0]$ cross-section, i. e., the highlighted plane in Fig. 4.7(a). From the result of DMD, we find that the stacking faults are emitted on the (111) and $(\bar{1}\bar{1}1)$ slip planes, referred to as slip planes B and C, respectively. All the stacking faults cut through the β phase shell, but do not penetrate the α/β phase boundary. In comparison, Fig. 4.8(b) shows the maximum RSS among the 3 slip systems associated with these two planes (shown in Table 4.1), predicted by the core-shell model. It is clear that the locations of (111) stacking faults coincide with the locations of high RSS associated with (111) plane; and the same agreement holds for the $(\bar{1}\bar{1}1)$ plane. Also, along any radial direction, the maximum RSS associated with both (111) and $(\bar{1}\bar{1}1)$ reaches the highest value at the core-shell interface,

[1]The CRSS of Pd-H is estimated to be between 0.41 GPa and 3.27 GPa, using the embedded atom method (EAM) potential of Zhou *et al.* [48].

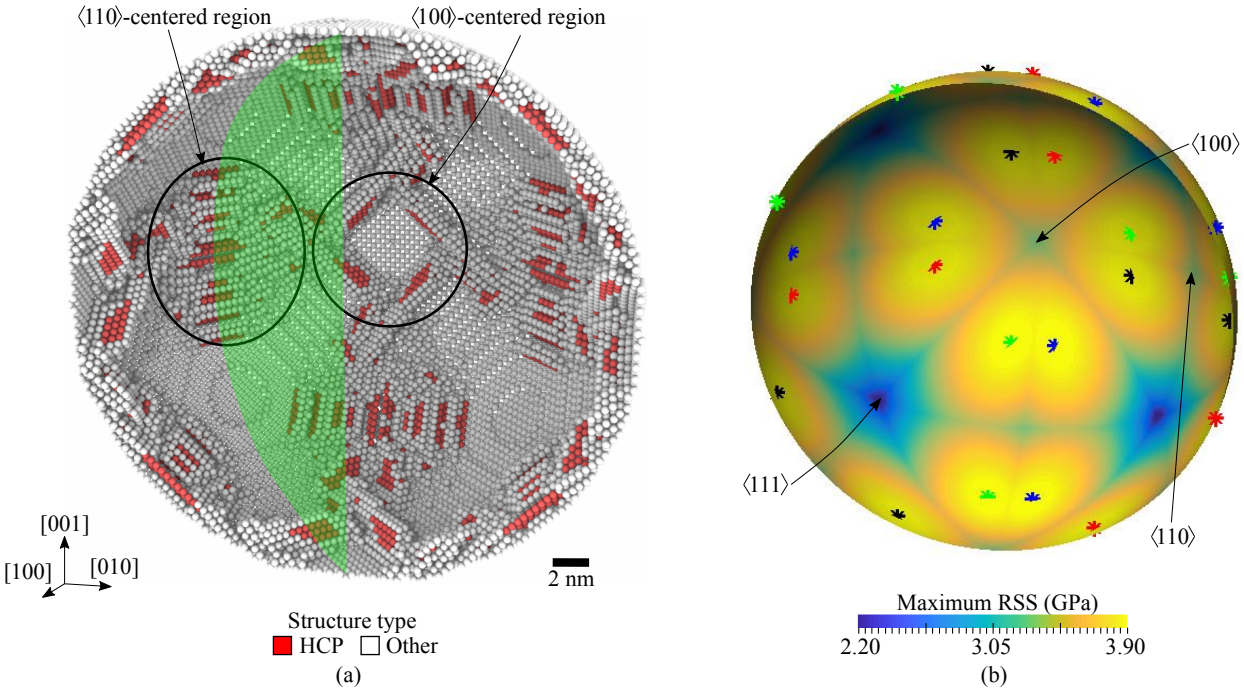

Figure 4.7: (a) Distribution of stacking faults predicted by the DMD simulation at 4.5 s. (b) Maximum resolved shear stress (RSS) obtained from the core-shell model. In Subfigure (a), the green plane denotes the middle $[1\bar{1}0]$ cross-section. In Subfigure (b), the locations of the global maximum values are marked with asterisks.

then drops immediately to zero inside the α phase.

In summary, the formation of stacking faults in the spherical nanoparticle and the distribution pattern they adopt can be explained as a mechanism for relaxing the residual stress induced by the atomistically sharp α/β phase boundary. The elastic core-shell model is found to be a convenient tool to explain the DMD result. In the next section, we will continue using it, to explain the dynamics (e. g., growth, branching, and disappearance) of the stacking faults caused by the propagation of the α/β phase boundary.

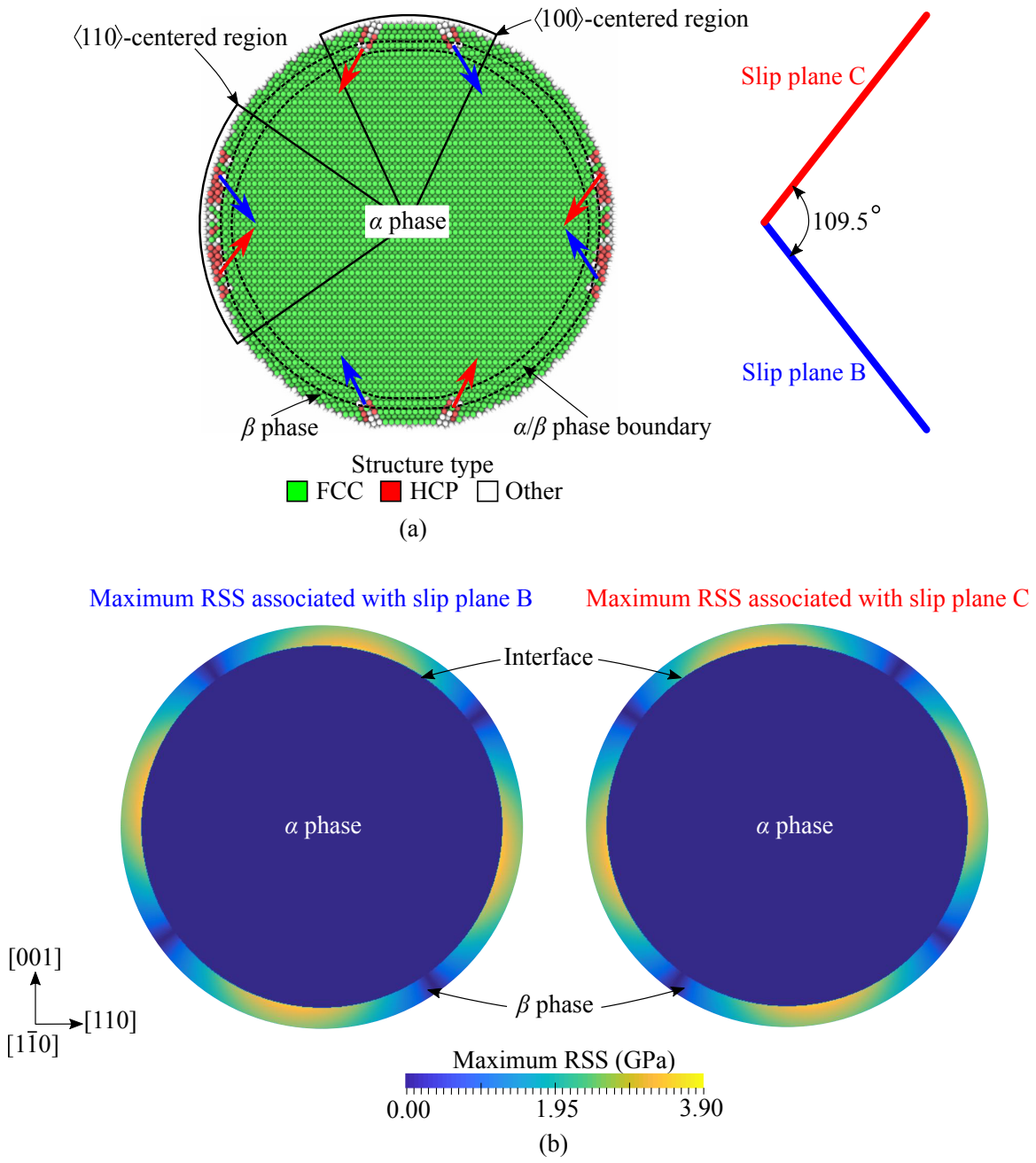

Figure 4.8: Results of (a) the DMD simulation at 4.5 s and (b) the elastic core-shell model on the middle [1$\bar{1}$0] plane.

Dynamics of stacking faults

We examine the evolution of the stacking faults identified in the previous section. Figure 4.9 visualizes the evolution of stacking faults in a ⟨100⟩-centered region. Specifically, the images

taken at 4.5 s show that as a thin layer of β phase Pd-H develops, four extrinsic stacking faults are emitted from the surface of the particle. Each of them is created by two Shockley partial dislocations on adjacent {111} planes, within the α/β phase boundary. The formation of stacking faults through double Shockley partials has been observed previously in MD simulations of other materials during mechanical deformations (e. g., copper, with relatively low stacking fault energy [56], and aluminum, with relatively high stacking fault energy [57]). Nonetheless, in the present study, the deformation is driven by the transport of solute atoms.

Moreover, Fig. 4.9 shows that the four stacking faults on different {111} planes form a tunnel-like structure with a 109.5° angle between neighboring walls. A Lomer-Cottrell lock along ⟨110⟩ direction forms at the intersection of each pair of stacking faults. The reaction is

$$1/6[211] + 1/6[\bar{2}1\bar{1}] \rightarrow 1/3[010]. \tag{4.17}$$

As the α/β phase boundary propagates inwards, the double Shockley partials glide on their {111} slip planes. Because of the sessile Lomer-Cottrell locks, the tunnel-like structure retains its shape, while the four stacking faults extend inwards. At approximately 7.5 s, a new Shockley partial is emitted from the surface of the particle, near each stacking fault. This Shockley partial transforms the extrinsic stacking fault into a three-layer twin.

It is notable that after approximately 17.5 s, the stacking faults stop growing. This can be explained by the fact that the angle between the fault plane of each stacking fault and the propagation direction of the phase boundary — measured at the tip of the stacking fault and

indicated with red and yellow arrows in Fig. 4.9(b) — gradually increases. At approximately 17.5 s, this angle reaches 90°. After this point, any further extension of the stacking faults would not "catch" the phase boundary and resolve the associated high stress. As a result, the stacking faults stop growing. Later, as the phase boundary moves away from the stacking faults, the tunnel-like stacking fault structure gradually dissolves in the FCC lattice, starting at the surface of the particle.

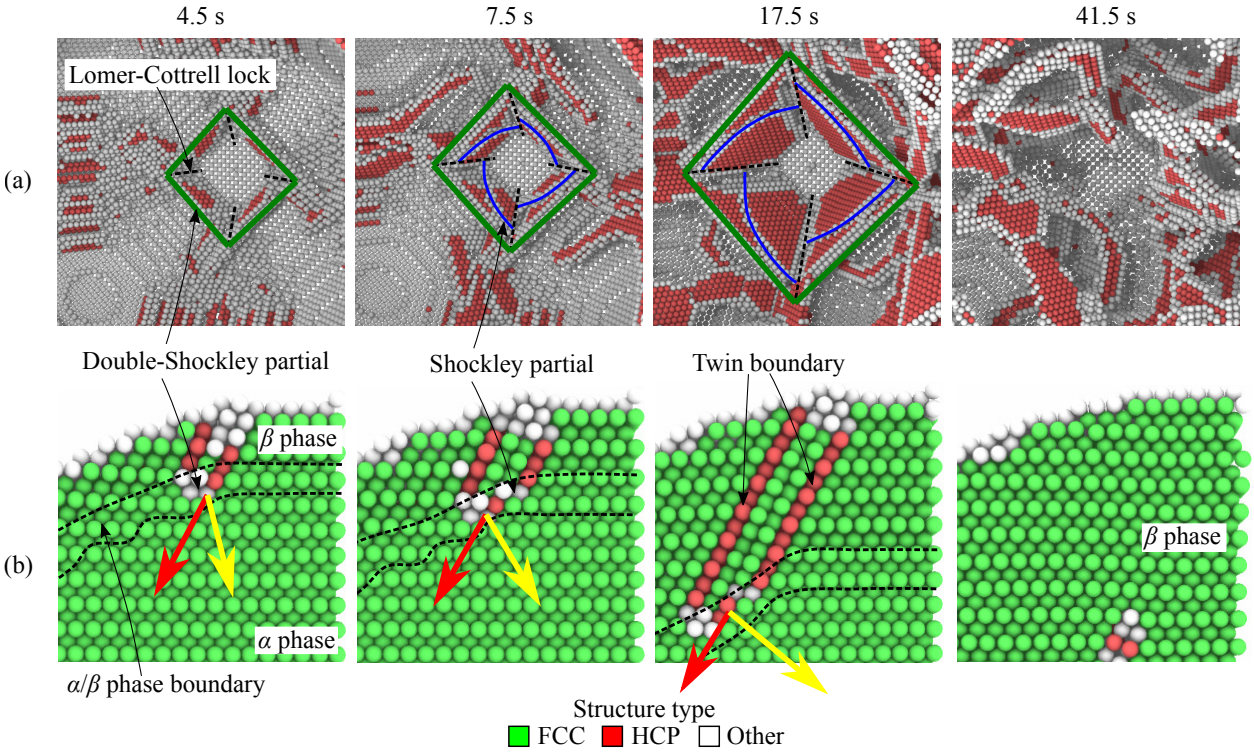

Figure 4.9: Evolution of stacking faults in a ⟨100⟩-centered region. Subfigure (a) shows a perspective view of the stacking faults. Subfigure (b) shows a middle ⟨110⟩ cross-section of one stacking fault in the tunnel-like structure. The red and yellow arrows indicate the gliding direction of the stacking fault and the propagation direction of the phase boundary, respectively.

Figure 4.10 visualizes the evolution of stacking faults within a ⟨110⟩-centered region. At around 7.5 s, a stacking fault is emitted from the surface of the particle, gliding on a {111}

plane (specifically, slip plane C). This stacking fault is denoted by SF-A for the ease of reference. SF-A is generated by the successive emission of three Shockley partial dislocations from the surface of the particle. The stacking sequences around SF-A are

$$(1) \cdots \text{ABCABCABCABC} \cdots,$$

$$(2) \cdots \text{CABC}\underline{\text{AC}}\text{ABCABC} \cdots,$$

$$(3) \cdots \text{BCAB}\underline{\text{C}}\text{B}\underline{\text{A}}\text{BCABC} \cdots,$$

$$(4) \cdots \text{ABCA}\underline{\text{B}}\text{AC}\underline{\text{B}}\text{CABC} \cdots,$$

in which the locations of the four stacking sequences are marked in Fig. 4.10(a). The A-B-C nomenclature denotes the three possible positions of {111} layers in the projection onto a {110} plane. The underlined letters indicate the planes in a local hexagonal close-packed (HCP) stacking sequence. Therefore, the four regions have the features of: (1) a perfect FCC lattice, (2) an intrinsic stacking fault, (3) an extrinsic stacking fault, and (4) a three-layer twin, respectively. This type of stacking fault structure has been observed previously in MD simulations of mechanical twinning (e. g., in aluminum [57] and steel [58]). Nonetheless, our results reveal that, this twinning process can also be driven by the high residual stress due to phase transformation in chemical reactions (specifically, hydrogenation of Pd).

As the α/β phase boundary propagates towards the center of the particle, the Shockley partials glide along their slip planes, which drives SF-A to extend. SF-A keeps in connection with both the surface of the particle and the phase boundary, until approximately 17.5 s, when the fault plane becomes tangent to the phase boundary. Similar to the $\langle 100 \rangle$-centered

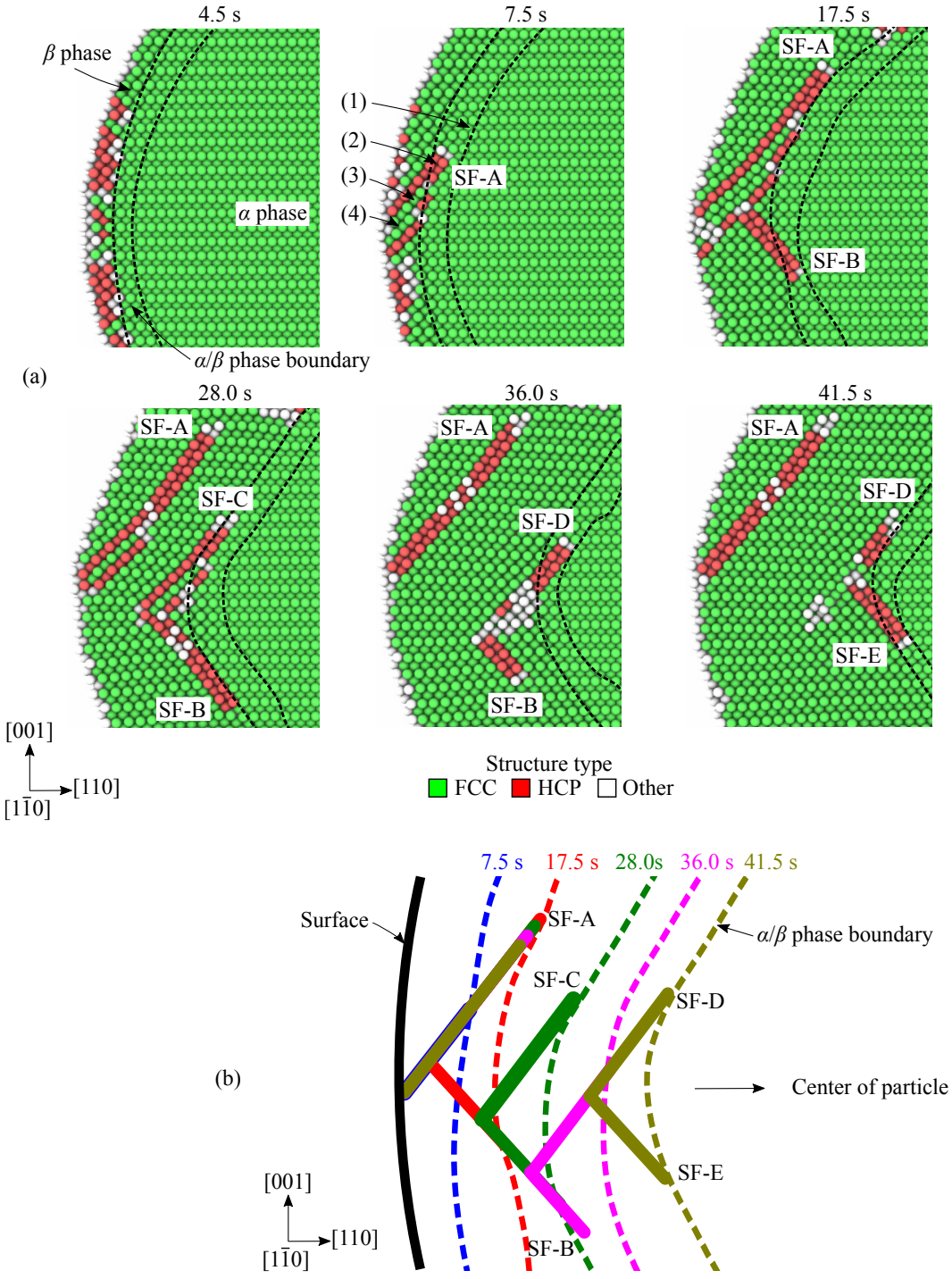

Figure 4.10: Time evolution of stacking faults in a ⟨110⟩-centered region. (a) Solution snapshots at six time instances. (The middle [1$\bar{1}$0] cross-section is shown.) (b) Superposition of the stacking faults at the six time instances.

region, after this point of time, SF-A stops growing. However, it is notable that a new intrinsic stacking fault is emitted from SF-A on slip plane B. This new stacking fault is denoted by SF-B in Fig. 4.10(a). The tip of SF-B is within the phase boundary. Also, a Lomer-Cottrell lock forms at the intersection of SF-A and SF-B.

We employ the core-shell model to understand the emission of SF-B from SF-A. Figure 4.11 shows that at 17.5 s, the tip of SF-A has just passed a region of high RSS associated with slip plane B. It is likely that this region of high RSS caused the emission of SF-B. Figure 4.11 also shows that the RSS associated with slip plane B near the stacking fault on a different slip plane is smaller in the ⟨100⟩-centered regions than in the ⟨110⟩-centered regions. This explains why the same phenomenon does not occur in the ⟨100⟩-centered regions.

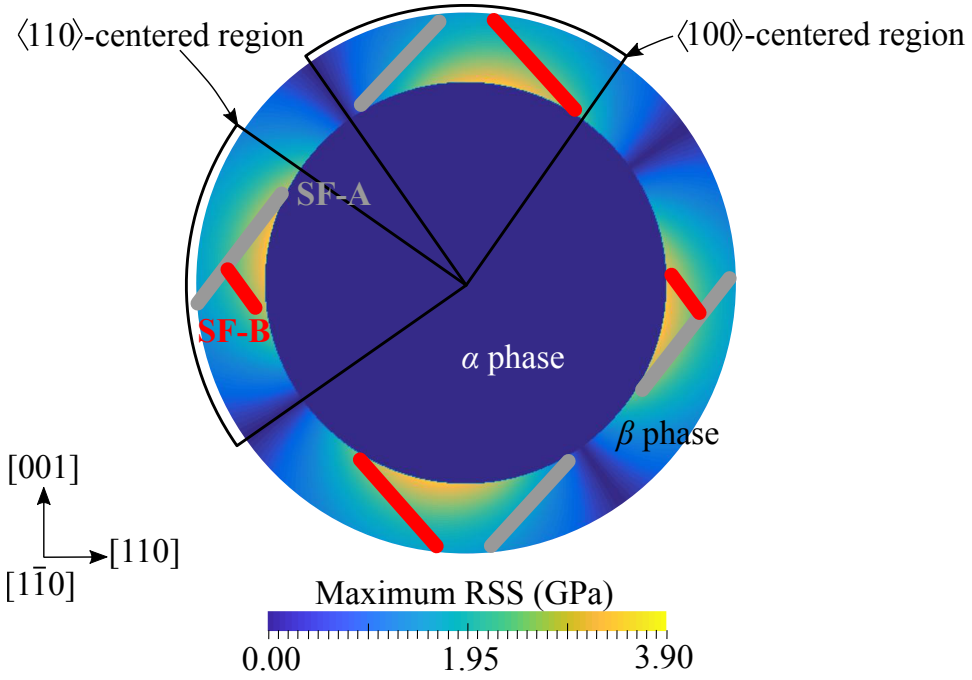

Figure 4.11: Superposition of the field of maximum RSS associated with slip plane B, predicted by the core-shell model, with stacking faults observed at 17.5 s. Stacking faults on slip plane B are colored in red.

As the phase boundary propagates inwards, the Shockley partial associated with SF-B glides on its slip plane (see Fig. 4.10(a)). At approximately 28.0 s, it is disconnected from SF-A. At the same time, a detwinning process takes place in SF-A, by the gliding of Shockley partials away from the phase boundary. Also, a new stacking fault, denoted by SF-C, has been emitted from SF-B with a Lomer-Cottrell lock at their intersection. The same phenomenon occurs repeatedly until approximately 53.0 s, when the surface area of the phase boundary is considerably small and the elastic lattice deformation alone is enough to release the residual stress on the interface. Overall, the dynamics of stacking faults in the $\langle 110 \rangle$-centered regions is dominated by the emission of new stacking faults from existing ones, the gliding of stacking faults towards the phase boundary, and the annihilation of stacking faults as the phase boundary moves away. This mechanism is schematically illustrated in Fig. 4.10(b).

In summary, the stacking faults observed during the H absorption process are on $\{111\}$ planes, which is typical for FCC crystals. After a thin layer of β phase Pd-H has formed under the surface of the particle, stacking faults start to appear within the β phase, mostly in $\langle 100 \rangle$- and $\langle 110 \rangle$-centered regions, where the RSS on $\{111\}$ planes is high. The $\{111\}$ fault planes of these stacking faults do not pass through the center of the particle. As a result, after some time, they become tangent to the phase boundary. When this happens, the stacking faults stop growing, as the RSS at the tips significantly decreases. In the $\langle 110 \rangle$-centered regions, we observe the emission of new stacking faults from old ones, as a mechanism to "catch" the movement of the phase boundary. This phenomenon does not appear in the $\langle 100 \rangle$-centered regions. The reason is that in the $\langle 100 \rangle$-centered regions, the

maximum RSS near existing stacking faults associated with different slip planes is relatively small and cannot drive the emission of new stacking faults.

4.5.2 Effect of particle shape

Next, we examine the octahedral particle which, in contrast to the sphere, has planar faces and sharp edges and corners. Figure 4.12 shows the initial distribution of stacking faults at 4.5 s. The distribution pattern is different from that in the spherical particle. Specifically, stacking faults are formed near the edges of the particle, forming 12 separate, fusiform branches. In each branch, two stacking faults are emitted along two different {111} slip planes. This distribution pattern is due to the fact that after the formation of a thin β phase layer, the edges of the particle have relatively large displacements parallel to {111} planes.

Figure 4.13 visualizes the evolution of the stacking faults by showing the structure type on the middle $[1\bar{1}0]$ cross-section (i. e., the highlighted plane in Fig. 4.12). At 4.5 s, the zoom-in view shows that the three outermost {111} layers in the β phase undergo a shear displacement, due to the lattice expansion from α to β phase. The stacking faults keep in connection with the surface of the particle. They separate a small region from the FCC matrix, in which the Pd lattice is largely distorted. Moreover, the edges of the octahedron stretch outwards, forming a star-like shape. The stretching is caused by the interaction of expanded neighboring faces. This star-shaped deformation has also been observed experimentally in Pd nanocubes with edge length of approximately 60 nm [14]. As the phase boundary propagates, the stacking

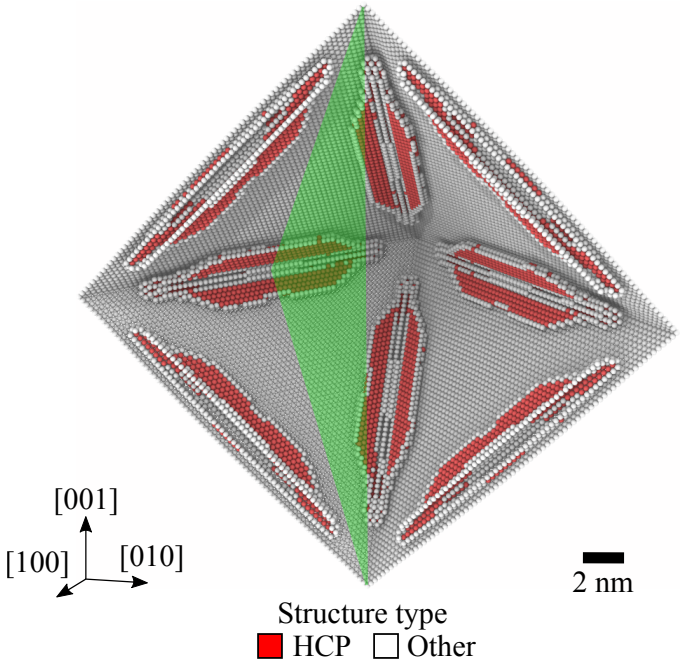

Figure 4.12: Distribution of stacking faults predicted by the DMD simulation at 4.5 s. The green plane denotes the middle $[1\bar{1}0]$ cross-section.

faults move towards the center of the particle. At 23.0 s, an intersection of twins takes place outside the octahedral edges of the phase boundary, separating a rhomboid FCC block from the FCC matrix. As the phase boundary approaches the center of the particle, the size of the stacking faults reduces, and they become disconnected from the surface of the particle.

Next, we examine in detail the dynamics of the observed stacking faults. We focus on the stacking faults near one edge of the particle, and the result is shown in Fig. 4.14. At 4.5 s, two Shockley partials are emitted from the distorted region, leaving behind two intrinsic stacking faults. We focus on one of the two stacking faults, and the associated partial dislocation is denoted by PD-A for the ease of reference. At 7.0 s, a new Shockley partial, denoted by PD-B, has been emitted within the phase boundary, adjacent to the previously formed stacking

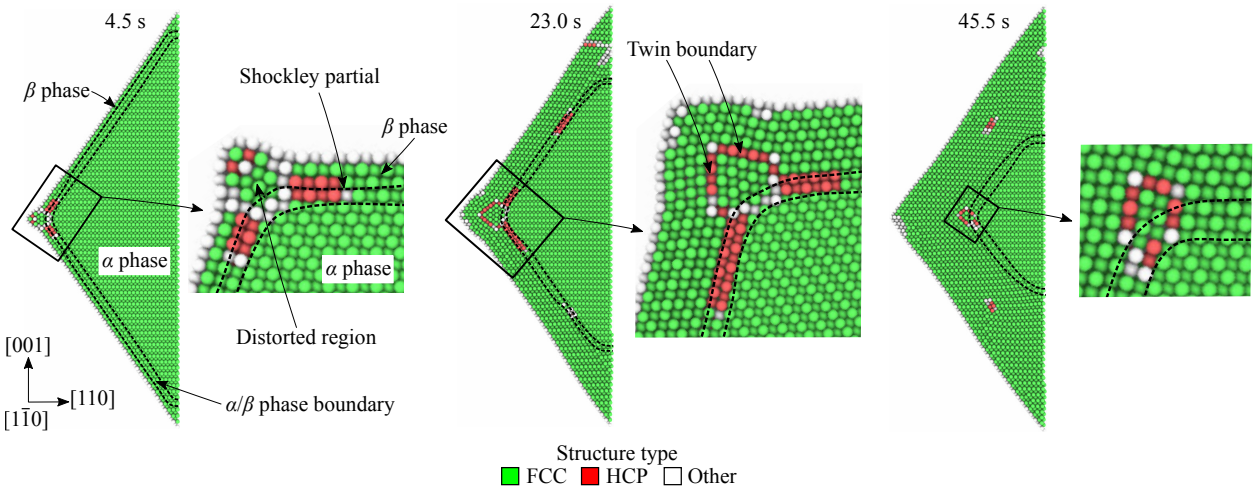

Figure 4.13: Evolution of stacking faults in the octahedral particle.

fault. PD-B glides away from the distorted region, transforming the intrinsic stacking fault to an extrinsic one. By contrast, PD-A glides in the opposite direction, because it is away from the phase boundary. As the phase boundary propagates inwards, PD-B keeps growing, and PD-A gradually disappears. As a result, the stacking fault moves over one atomic layer in the direction perpendicular to its fault plane. The same layer-by-layer process is repeated until approximately 56.5 s, when the surface area of the phase boundary is considerably small.

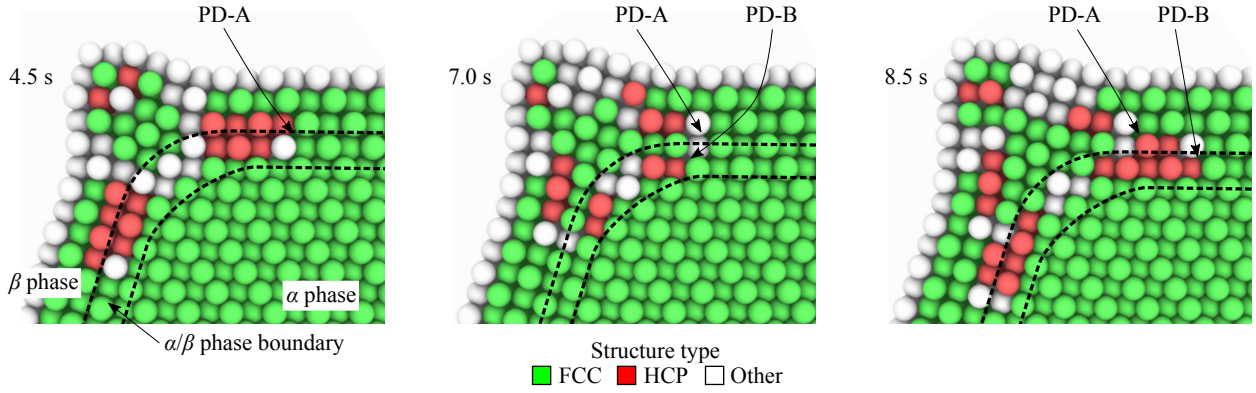

Figure 4.14: Details of the dynamics of the stacking faults in the octahedral particle.

Notably, in the octahedral particle, the dynamics of the stacking faults is dominated by the movement of partial dislocations on consecutive fault planes. This mechanism, clearly different from that in the spherical particle, is dominated by the morphology of the phase boundary. In the octahedral particle, the phase boundary retains planar {111} faces during the H absorption process, and stacking faults start to appear near the edges of the phase boundary. Therefore, as the phase boundary moves, the stacking faults quickly become tangent to it. When this happens, the stacking faults stop gliding, and new partial dislocations have been emitted from the edges of the phase boundary. These dislocations are adjacent to the existing stacking faults, driving them to "catch" the phase boundary.

Moreover, our DMD results show that in both the spherical and octahedral Pd particles, the propagation of the atomistically sharp phase boundary results in the formation, and then the *removal* of crystallographic imperfections (specifically, stacking faults). The ability of nanostructured Pd to "self-heal" defects during H loading and unloading processes has been discovered in a few recent experimental studies [16, 59]. To this end, our simulations have provided additional, atomic-level details on the dynamics of stacking faults during the H absorption process.

By contrast, in the cubic particle, no stacking faults appear during the H absorption process. In order to explain this difference, we examine the area on one {111} plane that is mismatched with another parallel {111} plane. In this regard, Fig. 4.15 schematically compares the three particles in different shape. Two parallel {111} atomic layers are sketched: one in the β phase and the other cutting the phase boundary. The misfit area is colored in blue. Compared to

the sphere and the octahedron, the cubic particle has a much smaller misfit area. Since the {111} family of planes is the major operative slip plane in the FCC crystal, the large misfit area in the spherical and octahedral particles leads to large lateral movement between two {111} layers and hence the emergence of stacking faults. On the other hand, the smaller misfit area in the cubic particle explains the absence of stacking fault.

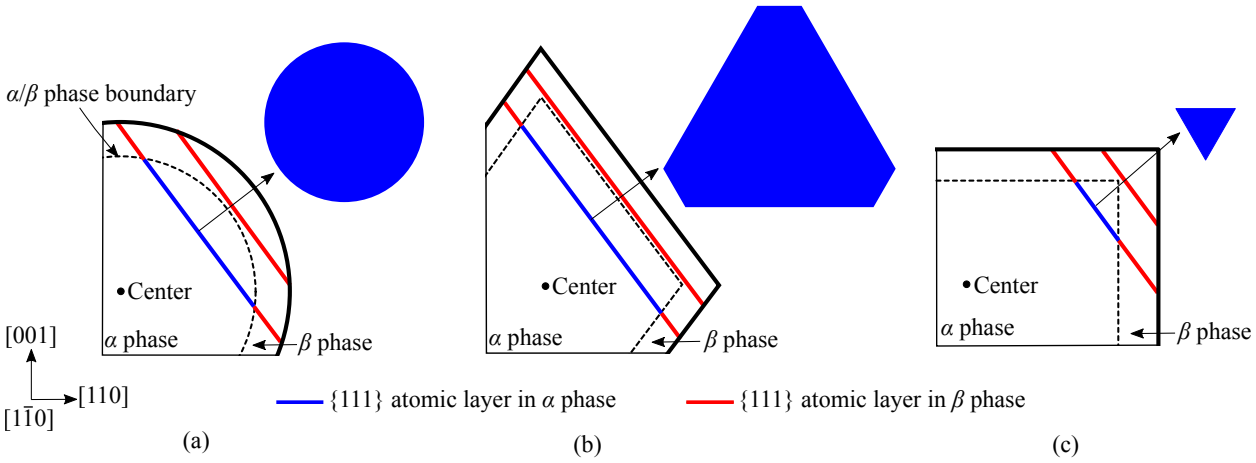

Figure 4.15: Schematic illustration of the effect of particle shape on the lattice deformation: (a) spherical, (b) octahedral, and (c) cubic particles.

4.6 Rate of hydrogen absorption

We proceed to examine the effect of particle shape on the overall H absorption process. Figure 4.16 shows the time-history of H concentration in each particle and its time derivative. Notably, the cubic particle absorbs H faster than the other two. This can be explained by two factors. First, the three particles are designed to have approximately the same volume. Under this condition, the cubic particle has the highest surface-area-to-volume ratio. Therefore, during the early stage when a thin layer of β phase is formed, the phase boundary in the

cubic particle provides largest surface area for H diffusion into the α phase core. Second, the phase boundary in the cubic particle remains coherent, which may facilitate the absorption of H as explained in Section 4.4.

Moreover, Fig. 4.16(b) shows that from approximately 4.5 s to 16.5 s, the rate of H absorption in the octahedral particle is clearly lower than that in the spherical one. This difference cannot be explained through the comparison of surface-area-to-volume ratio. In fact, for the same volume, the surface-area-to-volume ratio of an octahedron is higher than that of a sphere. Instead, the difference may be related to the volume fraction of solute-induced stacking faults. Figure 4.17 shows that during the aforementioned time period, the octahedral particle has a higher volume fraction of stacking faults than the spherical one. In other words, the phase boundary in the octahedral particle has a larger semi-coherent area. Therefore, in this stage, misfit dislocations become an important factor that controls the rate of H absorption, overriding the effect of surface-area-to-volume ratio.

4.7 Conclusions

We have analyzed the absorption of hydrogen (H) by three palladium (Pd) nanoparticles of different morphologies (i. e., spherical, octahedral and cubic) using Diffusive Molecular Dynamics (DMD). The chief advantage of DMD which renders it ideally suited for this application is its ability to simulate long-term behavior of atomic systems without the time constraints inherent to Molecular Dynamics (MD). Indeed, atomic resolution is required

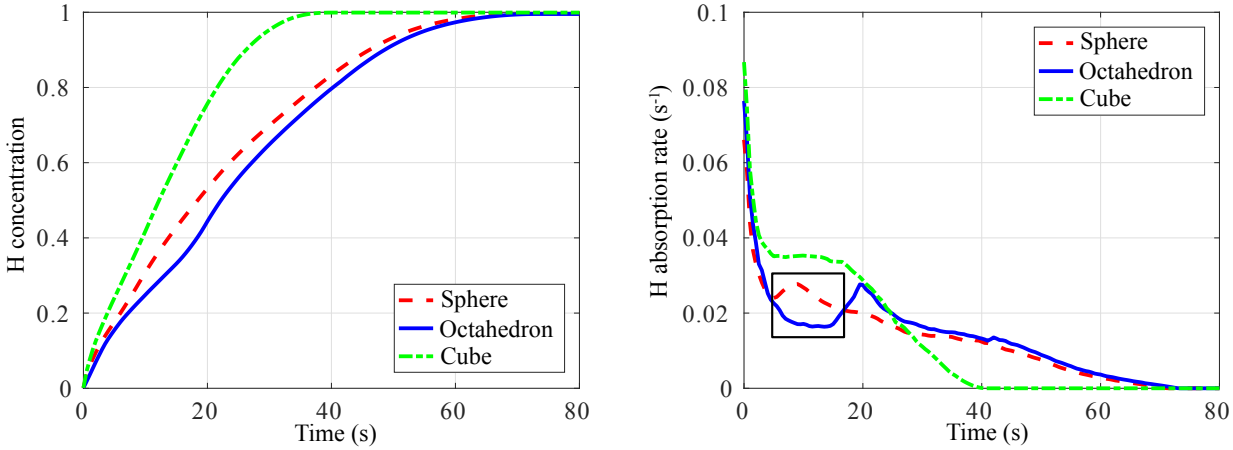

(a) (b)

Figure 4.16: Time-history of H absorption: (a) H concentration and (b) rate of H absorption.

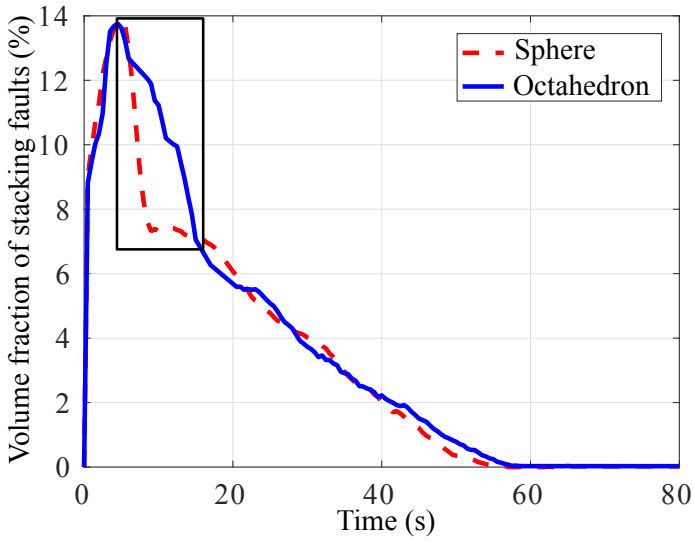

Figure 4.17: Time-history of volume fraction of stacking faults.

in order to ascertain the complex mechanisms set in motion by H absorption into the Pd nanoparticles. These mechanisms, as identified in calculations, include phase transformation, phase boundary motion, misfit dislocations, stacking faults and their evolution. The motion of the α/β phase boundary is the net result of a complex interplay between these mechanisms.

Several main findings afforded by the calculations are noteworthy. Firstly, the hydride phase transformation in Pd nanoparticles is dominated by the propagation of an atomistically sharp α/β phase boundary. The phase boundary in the cubic particle remains coherent during the H absorption process, whereas stacking faults are observed in the spherical and octahedral particles. These stacking faults move together with the propagating sharp phase boundary in order to release the elastic stress induced at the phase boundary by the misfit between the α and β lattices. Specifically, in the spherical particle, the movement of stacking faults is dominated by the emission of a new stacking fault from an existing one, the gliding of stacking faults together with the phase boundary and the annihilation of stacking faults behind from the phase boundary. In the octahedral particle, the dynamics of stacking faults is dominated by the movement of partial dislocations on consecutive fault planes. Moreover, the particle shape has an effect on the diffusion of H. Specifically, the cubic particle exhibits the ability to absorb H atoms faster than the other two shapes. Our DMD model also predicts that the formation and movement of stacking faults may slow down the propagation of the hydride phase boundary, and hence reduce the speed of H absorption. In this regard, the two-way interaction between H absorption and lattice deformation is remarkable.

These predictions also indicate that for the particle size and shapes under consideration, the cubic particle aligned with {100} planes may be optimal for H storage applications. The suppression of stacking fault formation in the cubic nanoparticles and the persistent coherence of the phase boundary may also be expected to enhance the repeatability of the storage cycle and, therefore, the useful life of the nanoparticles. However, the mechanisms of

phase boundary motion and the H storage characteristics identified in this study are likely to be size dependent. In particular, the coherence of the phase boundary may be lost for cubic nanoparticles exceeding a critical size. Larger nanoparticle sizes also promote decomposition into grains separated by grain boundaries. Under those conditions, grain boundaries are known to mediate hydrogenation and to influence the storage characteristics of individual nanoparticles [60]. These and other trade-offs suggest themselves as worthwhile directions for further study.

Acknowledgments

The authors gratefully acknowledge the support of the U. S. Office of Naval Research (ONR) under grant number N00014-17-1-2831, the Ministerio de Economía y Competitividad of Spain under grant number DPI2015-66534-R, and the U. S. Army Research Laboratory (ARL) through the Materials in Extreme Dynamic Environments (MEDE) Collaborative Research Alliance (CRA) under Award Number W911NF-11-R-0001.

Appendix

4.A An elastic core-shell model

The elastic field of a spherical core in an elastically matched, concentric spherical shell can be obtained by elementary methods of linear elasticity. For completeness, here we present a short derivation for the case of isotropic elasticity with Lamé constants $\lambda^{(s)}$ and $\mu^{(s)}$ for the shell and $\lambda^{(c)}$ and $\mu^{(c)}$ for the core. The shell undergoes a volumetric expansion $\kappa = \Delta V/V$, i. e., its volume V would increase by $\Delta V = \kappa V$ if the core were released from the shell. We employ spherically symmetric displacements in the spherical coordinate system (r, θ, ϕ)

$$u_r = u_r(r), \tag{4.18}$$

where r refers to the radial distance. The corresponding strains are

$$\epsilon_{rr} = \frac{du_r}{dr}, \qquad \epsilon_{tt} = \frac{u_r}{r}, \tag{4.19}$$

where t refers to any coordinate (i. e., polar angle θ or azimuthal angle ϕ) that has transverse direction perpendicular to the radial direction. From Hooke's law, the stresses follow as

$$\sigma_{rr} = \lambda(\epsilon_{rr} + 2\epsilon_{tt}) + 2\mu\epsilon_{rr}, \tag{4.20a}$$

$$\sigma_{tt} = \lambda(\epsilon_{rr} + 2\epsilon_{tt}) + 2\mu\epsilon_{tt}. \tag{4.20b}$$

The radial equilibrium equation is

$$\frac{d\sigma_{rr}}{dr} + 2\frac{\sigma_{rr} - \sigma_{tt}}{r} = 0, \tag{4.21}$$

or, in terms of displacements,

$$\frac{d^2u_r}{dr^2} + \frac{2}{r}\frac{du_r}{dr} - \frac{2u_r}{r^2} = 0. \tag{4.22}$$

The corresponding general solution is

$$u_r = Ar + \frac{B}{r^2}, \tag{4.23}$$

with stresses

$$\sigma_{rr} = 3\lambda A + 2\mu\left(A - \frac{2B}{r^3}\right), \tag{4.24a}$$

$$\sigma_{tt} = 3\lambda A + 2\mu\left(A + \frac{B}{r^3}\right). \tag{4.24b}$$

If the core were released from the shell, the change of volume in the shell would induce a displacement at its inner boundary such that

$$4\pi {R^{(c)}}^2 u_0 = \kappa\frac{4\pi {R^{(c)}}^3}{3}, \tag{4.25}$$

or

$$u_0 = \frac{\kappa}{3} R^{(c)}, \tag{4.26}$$

where $R^{(c)}$ is the radius of the core. The core-shell system then undergoes displacements

$$u_r^{(c)} = A^{(c)} r + \frac{B^{(c)}}{r^2}, \quad r < R^{(c)}, \tag{4.27a}$$

$$u_r^{(s)} = A^{(s)} r + \frac{B^{(s)}}{r^2}, \quad r > R^{(c)}, \tag{4.27b}$$

in order to restore compatibility. The corresponding boundary conditions are

$$u_r^{(c)}(0) < +\infty, \tag{4.28a}$$

$$u_r^{(c)}(R^{(c)}) = u_0 + u_r^{(s)}(R^{(c)}), \tag{4.28b}$$

$$\sigma_{rr}^{(c)}(R^{(c)}) = \sigma_{rr}^{(s)}(R^{(c)}), \tag{4.28c}$$

$$\sigma_{rr}^{(s)}(R^{(s)}) = 0, \tag{4.28d}$$

where $R^{(s)}$ is the radius of the outer surface of the shell. Solving for the constants, we find $B^{(c)} = 0$ and

$$A^{(c)} = \frac{4\mu^{(s)}\kappa(3\lambda^{(s)} + 2\mu^{(s)}) \left({R^{(c)}}^3 - {R^{(s)}}^3 \right)}{D}, \tag{4.29a}$$

$$A^{(s)} = \frac{4\mu^{(s)} {R^{(c)}}^3 \kappa(3\lambda^{(c)} + 2\mu^{(c)})}{D}, \tag{4.29b}$$

$$B^{(s)} = \frac{{R^{(c)}}^3 {R^{(s)}}^3 \kappa(3\lambda^{(c)} + 2\mu^{(c)})(3\lambda^{(s)} + 2\mu^{(s)})}{D}, \tag{4.29c}$$

with

$$\begin{aligned} D = &-12\mu^{(s)}{R^{(c)}}^3(3\lambda^{(c)} - 3\lambda^{(s)} + 2\mu^{(c)} - 2\mu^{(s)}) \\ &- 3{R^{(s)}}^3(3\lambda^{(s)} + 2\mu^{(s)})(3\lambda^{(c)} + 2\mu^{(c)} + 4\mu^{(s)}). \end{aligned} \tag{4.30}$$

By spherical symmetry, the stress tensor has the representation

$$\boldsymbol{\sigma} = \sigma_{rr}\boldsymbol{e}_r \otimes \boldsymbol{e}_r + \sigma_{tt}(\boldsymbol{I} - \boldsymbol{e}_r \otimes \boldsymbol{e}_r), \tag{4.31}$$

where $\boldsymbol{e}_r$ is radial unit vector, $\otimes$ is the dyadic product and $\boldsymbol{I}$ is the identity matrix. In an FCC crystal, the slip systems based on Schmid and Boas' nomenclature are summarized in Table 4.1. The corresponding resolved shear stress (RSS) in a slip system n of slip plane $\boldsymbol{m}$ and slip direction $\boldsymbol{s}$ is

$$\tau(r, \theta, \phi; n) = \boldsymbol{s}^T\boldsymbol{\sigma}\boldsymbol{m} = (\boldsymbol{e}_r \cdot \boldsymbol{s})(\boldsymbol{e}_r \cdot \boldsymbol{m})(\sigma_{rr} - \sigma_{tt}) \equiv s_r m_r T(r), \tag{4.32}$$

where $s_r m_r$ is the Schmidt factor. On the interface $r = R^{(c)}$ in the shell, from the elastic stress field we compute

$$T(R^{(c)}) \equiv \sigma_{rr} - \sigma_{tt} = -\frac{6\mu^{(s)}{R^{(s)}}^3\kappa(3\lambda^{(c)} + 2\mu^{(c)})(3\lambda^{(s)} + 2\mu^{(s)})}{D}. \tag{4.33}$$

A straightforward calculation shows that the corresponding global maximum value of τ on

the interface $r = R^{(c)}$ is

$$\tau_{\max} = \max_{\theta,\phi} \ |\tau(R^{(c)}, \theta, \phi; n)| = \frac{1}{2}|T(R^{(c)})|, \tag{4.34}$$

which is the same for all the slip systems. The maximum RSS is attained at the interfacial points corresponding to

$$\boldsymbol{e}_r = \frac{\sqrt{2}}{2}(\boldsymbol{m} \pm \boldsymbol{s}), \tag{4.35a}$$

$$\boldsymbol{e}_r = -\frac{\sqrt{2}}{2}(\boldsymbol{m} \pm \boldsymbol{s}). \tag{4.35b}$$

The maximum value of RSS at the position (r, θ, ϕ) among a group of selected slip systems is

$$\bar{\tau}(r, \theta, \phi) = \max_{n} \ |\tau(r, \theta, \phi; n)|. \tag{4.36}$$

Slip system n	A2	A3	A6	B2	B4	B5
$\sqrt{2}\boldsymbol{s}$	$[01\bar{1}]$	$[101]$	$[\bar{1}\bar{1}0]$	$[0\bar{1}1]$	$[10\bar{1}]$	$[\bar{1}10]$
$\sqrt{3}\boldsymbol{m}$	$(\bar{1}11)$	$(\bar{1}11)$	$(\bar{1}11)$	(111)	(111)	(111)
Slip system n	C1	C3	C5	D1	D4	D6
$\sqrt{2}\boldsymbol{s}$	$[011]$	$[\bar{1}0\bar{1}]$	$[1\bar{1}0]$	$[0\bar{1}\bar{1}]$	$[\bar{1}01]$	$[110]$
$\sqrt{3}\boldsymbol{m}$	$(\bar{1}\bar{1}1)$	$(\bar{1}\bar{1}1)$	$(\bar{1}\bar{1}1)$	$(1\bar{1}1)$	$(1\bar{1}1)$	$(1\bar{1}1)$

Table 4.1: Slip-system sets in Schmid and Boas' nomenclature for the FCC crystal class. The vector $\boldsymbol{m}$ is the unit normal to the slip plane, and $\boldsymbol{s}$ is the unit vector in the direction of the Burgers vector. All vectors are expressed in the cartesian coordinate system.

In comparison with the DMD simulations for the Pd-H system, we consider the volumetric expansion of the shell induced by the α/β hydride phase transformation. Therefore, the

volumetric expansion ratio is

$$\kappa = 3\frac{a_\beta - a_\alpha}{a_\alpha} \tag{4.37}$$

where a_α and a_β denote the lattice constants of α and β phase, respectively. The structural and elastic properties used in the core-shell model are summarized in Table 4.2.

	Core (α phase)	Shell (β phase)	Source
Lattice constant a (Å)	3.885	4.115	From the DMD simulations
Elastic constant C_{11} (GPa)	245.8	241.7	From Pd and PdH_1 in Ref. [48], respectively
Elastic constant C_{12} (GPa)	199.8	190.3	

Table 4.2: Compilation of material constants for α and β phase Pd-H.

Bibliography

[1] D. A. Cogswell, M. Z. Bazant, Theory of coherent nucleation in phase-separating nanoparticles, Nano Letters 13 (7) (2013) 3036–3041.

[2] X. Zhang, M. van Hulzen, D. P. Singh, A. Brownrigg, J. P. Wright, N. H. van Dijk, M. Wagemaker, Rate-induced solubility and suppression of the first-order phase transition in olivine lifepo4, Nano Letters 14 (5) (2014) 2279–2285.

[3] B. Sakintuna, F. Lamari-Darkrim, M. Hirscher, Metal hydride materials for solid hydrogen storage: a review, International Journal of Hydrogen Energy 32 (9) (2007) 1121–1140.

[4] D. Mori, K. Hirose, Recent challenges of hydrogen storage technologies for fuel cell vehicles, International Journal of Hydrogen Energy 34 (10) (2009) 4569–4574.

[5] D. Chartouni, N. Kuriyama, T. Kiyobayashi, J. Chen, Metal hydride fuel cell with intrinsic capacity, International Journal of Hydrogen Energy 27 (9) (2002) 945–952.

[6] A. Pundt, Hydrogen in nano-sized metals, Advanced Engineering Materials 6 (1-2) (2004) 11–21.

[7] M. Yamauchi, R. Ikeda, H. Kitagawa, M. Takata, Nanosize effects on hydrogen storage in palladium, The Journal of Physical Chemistry C 112 (9) (2008) 3294–3299.

[8] R. Griessen, N. Strohfeldt, H. Giessen, Thermodynamics of the hybrid interaction of hydrogen with palladium nanoparticles, Nature Materials 15 (3) (2016) 311.

[9] B. D. Adams, A. Chen, The role of palladium in a hydrogen economy, Materials Today 14 (6) (2011) 282–289.

[10] R. Bardhan, L. O. Hedges, C. L. Pint, A. Javey, S. Whitelam, J. J. Urban, Uncovering the intrinsic size dependence of hydriding phase transformations in nanocrystals, Nature Materials 12 (10) (2013) 905–912.

[11] A. Baldi, T. C. Narayan, A. L. Koh, J. A. Dionne, In situ detection of hydrogen-induced phase transitions in individual palladium nanocrystals, Nature Materials 13 (12) (2014) 1143–1148.

[12] G. Li, H. Kobayashi, S. Dekura, R. Ikeda, Y. Kubota, K. Kato, M. Takata, T. Yamamoto, S. Matsumura, H. Kitagawa, Shape-dependent hydrogen-storage properties in pd nanocrystals: which does hydrogen prefer, octahedron (111) or cube (100)?, Journal of the American Chemical Society 136 (29) (2014) 10222–10225.

[13] G. Li, H. Kobayashi, J. M. Taylor, R. Ikeda, Y. Kubota, K. Kato, M. Takata, T. Yamamoto, S. Toh, S. Matsumura, et al., Hydrogen storage in pd nanocrystals covered with a metal–organic framework, Nature Materials 13 (8) (2014) 802–806.

[14] A. Ulvestad, M. Welland, S. Collins, R. Harder, E. Maxey, J. Wingert, A. Singer, S. Hy, P. Mulvaney, P. Zapol, et al., Avalanching strain dynamics during the hydriding phase transformation in individual palladium nanoparticles, Nature Communications 6 (2015) 1–8.

[15] B. Amin-Ahmadi, D. Connétable, M. Fivel, D. Tanguy, R. Delmelle, S. Turner, L. Malet, S. Godet, T. Pardoen, J. Proost, et al., Dislocation/hydrogen interaction mechanisms in hydrided nanocrystalline palladium films, Acta Materialia 111 (2016) 253–261.

[16] T. C. Narayan, F. Hayee, A. Baldi, A. L. Koh, R. Sinclair, J. A. Dionne, Direct visualization of hydrogen absorption dynamics in individual palladium nanoparticles, Nature Communications 8 (2017) 14020.

[17] A. Ulvestad, M. Welland, W. Cha, Y. Liu, J. Kim, R. Harder, E. Maxey, J. Clark, M. Highland, H. You, et al., Three-dimensional imaging of dislocation dynamics during the hydriding phase transformation, Nature materials 16 (5) (2017) 565–571.

[18] K. Wang, M. Ortiz, M. P. Ariza, Long-term atomistic simulation of hydrogen diffusion in metals, International Journal of Hydrogen Energy 40 (15) (2015) 5353–5358.

[19] Y. Kulkarni, J. Knap, M. Ortiz, A variational approach to coarse graining of equilibrium and non-equilibrium atomistic description at finite temperature, Journal of the Mechanics and Physics of Solids 56 (4) (2008) 1417–1449.

[20] M. P. Ariza, I. Romero, M. Ponga, M. Ortiz, Hotqc simulation of nanovoid growth under tension in copper, International Journal of Fracture 174 (1) (2012) 75–85.

[21] G. Venturini, K. Wang, I. Romero, M. P. Ariza, M. Ortiz, Atomistic long-term simulation of heat and mass transport, Journal of the Mechanics and Physics of Solids 73 (2014) 242–268.

[22] M. Ponga, M. Ortiz, M. P. Ariza, Finite-temperature non-equilibrium quasi-continuum analysis of nanovoid growth in copper at low and high strain rates, Mechanics of Materials 90 (2015) 253–267.

[23] J. Li, S. Sarkar, W. T. Cox, T. J. Lenosky, E. Bitzek, Y. Wang, Diffusive molecular dynamics and its application to nanoindentation and sintering, Physical Review B 84 (5) (2011) 054103.

[24] S. Sarkar, J. Li, W. T. Cox, E. Bitzek, T. J. Lenosky, Y. Wang, Finding activation pathway of coupled displacive-diffusional defect processes in atomistics: Dislocation climb in fcc copper, Physical Review B 86 (1) (2012) 014115.

[25] G. Simpson, M. Luskin, D. J. Srolovitz, A theoretical examination of diffusive molecular dynamics, SIAM Journal on Applied Mathematics 76 (6) (2016) 2175–2195.

[26] X. Sun, M. P. Ariza, K. Wang, Deformation-diffusion coupled analysis of long-term hydrogen diffusion in nanofilms, in: Proceedings of VII European Congress on Computational Methods in Applied Sciences and Engineering, Vol. 1, ECCOMAS, 2016, pp. 197–208.

[27] M. Ponga, M. Ortiz, M. P. Ariza, A comparative study of nanovoid growth in FCC metals, Philosophical Magazine 97 (32, A) (2017) 2985–3007.

[28] J. P. Mendez, M. Ponga, M. Ortiz, Diffusive molecular dynamics simulations of lithiation of silicon nanopillars, Journal of the Mechanics and Physics of Solids 15 (2018) 123–141.

[29] R. A. Miron, K. A. Fichthorn, Accelerated molecular dynamics with the bond-boost method, The Journal of Chemical Physics 119 (12) (2003) 6210–6216.

[30] A. F. Voter, Introduction to the kinetic monte carlo method, in: Radiation Effects in Solids, Springer, 2007, pp. 1–23.

[31] C. S. Martin, M. P. Ariza, M. Ortiz, Modeling thermal conductivity in silicon nanowires, GAMMMitteilungen 38 (2015) 201–212.

[32] E. Dontsova, J. Rottler, C. Sinclair, Solute-defect interactions in al-mg alloys from diffusive variational gaussian calculations, Physical Review B 90 (17) (2014) 174102.

[33] X. Sun, M. P. Ariza, M. Ortiz, K. G. Wang, Long-term atomistic simulation of hydrogen absorption in palladium nanocubes using a diffusive molecular dynamics method, International Journal of Hydrogen Energy 43 (11) (2018) 5657–5667.

[34] E. T. Jaynes, Information theory and statistical mechanics i, Physical Review 106 (4) (1957) 620–630.

[35] E. T. Jaynes, Information theory and statistical mechanics ii, Physical Review 108 (2) (1957) 171–190.

[36] S. R. De Groot, P. Mazur, Non-equilibrium thermodynamics, Courier Corporation, 2013.

[37] X. Sun, M. P. Ariza, M. Ortiz, K. Wang, Acceleration of diffusive molecular dynamics simulations through mean field approximation and subcycling time integration, Journal of Computational Physics 350 (2017) 470–492.

[38] B. Gonzalez-Ferreiro, I. Romero, M. Ortiz, A numerical method for the time coarsening of transport processes at the atomistic scale, Modelling and Simulation in Materials Science and Engineering 24 (4) (2016) 045011.

[39] B. Farmer, M. Luskin, P. Plecháč, G. Simpson, Spin-diffusions and diffusive molecular dynamics, Modelling and Simulation in Materials Science and Engineering 25 (8) (2017) 084003.

[40] J. D. Head, M. C. Zerner, A broyden-fletcher-goldfarb-shanno optimization procedure for molecular geometries, Chemical Physics Letters 122 (3) (1985) 264 – 270.

[41] S. Balay, S. Abhyankar, M. F. Adams, J. Brown, P. Brune, K. Buschelman, L. Dalcin, V. Eijkhout, W. D. Gropp, D. Kaushik, M. G. Knepley, L. C. McInnes, K. Rupp, B. F. Smith, S. Zampini, H. Zhang, H. Zhang, PETSc users manual, Tech. Rep. ANL-95/11 - Revision 3.7, Argonne National Laboratory (2016).
URL `http://www.mcs.anl.gov/petsc`

[42] H. Okuyama, W. Siga, N. Takagi, M. Nishijima, T. Aruga, Path and mechanism of hydrogen absorption at pd (100), Surface Science 401 (3) (1998) 344–354.

[43] A. Zalineeva, S. Baranton, C. Coutanceau, G. Jerkiewicz, Octahedral palladium nanoparticles as excellent hosts for electrochemically adsorbed and absorbed hydrogen, Science Advances 3 (2) (2017) e1600542.

[44] Y. Sakamoto, K. Yuwasa, K. Hirayama, X-ray investigation of the absorption of hydrogen by several palladium and nickel solid solution alloys, Journal of the Less Common Metals 88 (1) (1982) 115–124.

[45] C. Sachs, A. Pundt, R. Kirchheim, M. Winter, M. Reetz, D. Fritsch, Solubility of hydrogen in single-sized palladium clusters, Physical Review B 64 (7) (2001) 075408.

[46] C. Lebouin, Y. Soldo, S. Grigoriev, M. Guymont, P. Millet, Kinetics of hydrogen sorption by palladium nanoparticles, International Journal of Hydrogen Energy 38 (2) (2013) 966–972.

[47] A. L. Bugaev, A. A. Guda, K. A. Lomachenko, V. V. Shapovalov, A. Lazzarini, J. G. Vitillo, L. A. Bugaev, E. Groppo, R. Pellegrini, A. V. Soldatov, et al., Core–shell structure of palladium hydride nanoparticles revealed by combined x-ray absorption spectroscopy and x-ray diffraction, The Journal of Physical Chemistry C 121 (33) (2017) 18202–18213.

[48] X. Zhou, J. A. Zimmerman, B. M. Wong, J. J. Hoyt, An embedded-atom method interatomic potential for pd–h alloys, Journal of Materials Research 23 (03) (2008) 704–718.

[49] M. Ruda, E. Crespo, S. R. de Debiaggi, Atomistic modeling of h absorption in pd nanoparticles, Journal of Alloys and Compounds 495 (2) (2010) 471–475.

[50] C. Lemier, J. Weissmüller, Grain boundary segregation, stress and stretch: effects on hydrogen absorption in nanocrystalline palladium, Acta Materialia 55 (4) (2007) 1241–1254.

[51] Webpage for BlueRidge (Sandy Bridge), `https://secure.hosting.vt.edu/www.arc.vt.edu/computing/blueridge-sandy-bridge/`.

[52] A. Stukowski, Visualization and analysis of atomistic simulation data with ovito–the open visualization tool, Modelling and Simulation in Materials Science and Engineering 18 (1) (2010) 015012.

[53] T. C. Narayan, A. Baldi, A. L. Koh, R. Sinclair, J. A. Dionne, Reconstructing solute-

induced phase transformations within individual nanocrystals, Nature Materials 15 (7) (2016) 768–774.

[54] S. Syrenova, C. Wadell, F. A. Nugroho, T. A. Gschneidtner, Y. A. D. Fernandez, G. Nalin, D. Świtlik, F. Westerlund, T. J. Antosiewicz, V. P. Zhdanov, et al., Hydride formation thermodynamics and hysteresis in individual pd nanocrystals with different size and shape, Nature Materials 14 (12) (2015) 1236.

[55] A. Stukowski, Structure identification methods for atomistic simulations of crystalline materials, Modelling and Simulation in Materials Science and Engineering 20 (4) (2012) 045021.

[56] J. Schiøtz, T. Vegge, F. Di Tolla, K. W. Jacobsen, Atomic-scale simulations of the mechanical deformation of nanocrystalline metals, Physical Review B 60 (17) (1999) 11971.

[57] V. Yamakov, D. Wolf, S. R. Phillpot, A. K. Mukherjee, H. Gleiter, Dislocation processes in the deformation of nanocrystalline aluminium by molecular-dynamics simulation, Nature Materials 1 (1) (2002) 45.

[58] P. Wang, S. Xu, J. Liu, X. Li, Y. Wei, H. Wang, H. Gao, W. Yang, Atomistic simulation for deforming complex alloys with application toward twip steel and associated physical insights, Journal of the Mechanics and Physics of Solids 98 (2017) 290–308.

[59] A. Ulvestad, A. Yau, The self-healing of defects induced by the hydriding phase transformation in palladium nanoparticles, Nature Communications 8 (1) (2017) 1376.

[60] S. Alekseeva, A. B. S. Fanta, B. Iandolo, T. J. Antosiewicz, F. A. A. Nugroho, J. B. Wagner, A. Burrows, V. P. Zhdanov, C. Langhammer, Grain boundary mediated hydriding phase transformations in individual polycrystalline metal nanoparticles, Nature Communications 8.

Chapter 5

Conclusions and Future Work

5.1 Conclusions

This dissertation presents the development, assessment and application of a computational framework, referred to as Diffusive Molecular Dynamics (DMD). This framework aims at solving long-term, three-dimensional, deformation-diffusion coupled problems of interstitial solute mass transport in crystalline solids. The main conclusions can be summarized as follows:

- A DMD computational framework has been developed. This work consists mainly of three parts.

  (1) A DMD model has been developed for the interstitial diffusion of solute atoms, which accounts for three-dimensional, deformation-diffusion coupled analysis. In

this model, a nonlinear optimization problem has been derived to capture three-dimensional deformation of the system, based on a new trial Hamiltonian that considers interstitial solutes. Meanwhile, a first-order, nonlinear ordinary differential equation has been developed to drive the long-term evolution of the system.

(2) Two numerical methods have been employed for accelerating DMD simulations while maintaining a high solution accuracy. In the first method, both first-order (i.e., the point estimate) and second-order mean field approximations have been explored to reduce the computational cost of evaluating the mean of the potential function. The second method, i.e., subcycling time integration, has been designed to regularly skip the computationally expensive optimization problem. Both constant and linear extrapolations have been studied to estimate the solution of the optimization problem when it is skipped.

(3) A high-performance computational solver has been developed. This solver includes a robust nonlinear optimizer that is equipped with a quasi-Newton Broyden-Fletcher-Goldfarb-Shanno (BFGS) method, and an efficient explicit time integrator. The solver has been parallelized with Message Passing Interface (MPI), using the PETSc/TAO library for large-scale simulations on computer clusters with distributed memory.

- The capability of the computational framework has been demonstrated, and its performance has been assessed. The framework has been applied to the solution of two problems pertaining to hydrogen (H) mass transport in palladium (Pd): (1) the dy-

namics of a single H atom on Pd lattice; and (2) the absorption of H by a Pd nanocube. In the first problem, the DMD framework has been validated against a classical lattice random walk model. In the second one, the DMD simulation confirms that the H absorption in Pd nanoparticles is dominated by the propagation of an atomically sharp, α/β phase boundary. Specifically, in the Pd nanocube with an edge length of 16 nm, the absorption time is longer than 30 s. In addition, several computational developments afforded by the framework are noteworthy. Firstly, in both problems, the first- and second-order mean field approximations reduce the computational cost by three orders of magnitude compared to the Monte Carlo method. Secondly, again in both problems, subcycling accelerates DMD simulations by a factor of four or more. Thirdly, the one-step error of the first-order approximation is small in the first problem, specifically, less than 0.05%, but it can exceed 9% in the second problem. In this case, the second-order extension reduces the maximum error by a factor of two, and the average error by a factor of ten.

- The computational framework has been applied to investigate the atomic behaviors and mechanisms of H absorption into Pd nanoparticles. This work consists mainly of two parts.

  (1) The framework has been employed to simulate H absorption into Pd nanocubes with edge lengths ranging from 4 nm to 16 nm. The following findings are noteworthy. During the absorption process of all the samples, the phase boundary propagates towards the center of the cube, and its shape evolves from a sharp

cube to a rounded one, then gradually morphs into a sphere. The propagation of the phase boundary induces local transient lattice expansion and distortion, especially in the β phase. It is also found that at the final equilibrium state H atoms have an affinity for the boundary and stay preferentially on and near the surface of the samples at the expense of the interior. A concave-convex inversion of form and shear strain is observed between the initial and final states of the samples. Moreover, the examination of size effect shows that as the size of the sample increases, the maximum absorption speed decreases, whereas the maximum volume fraction of distorted lattices increases.

(2) The framework has been employed to characterize H absorption into Pd nanoparticles of spherical, octahedral and cubic shapes with the same volume of approximately $3,800$ nm^3. Several main findings afforded by the calculations are noteworthy. The propagation of an atomistically sharp α/β phase boundary is observed during the hydride phase transformation in the three Pd nanoparticles. The phase boundary in the cubic particle remains coherent during the H absorption process, whereas stacking faults are observed in the spherical and octahedral particles. These stacking faults move together with the propagating sharp phase boundary in order to release the elastic stress induced at the phase boundary by the misfit between the α and β lattices. Specifically, in the spherical particle, the movement of stacking faults is dominated by the emission of a new stacking fault from an existing one, the gliding of stacking faults together with the phase

boundary and the annihilation of stacking faults behind from the phase boundary. In the octahedral particle, the dynamics of stacking faults is dominated by the movement of partial dislocations on consecutive fault planes. Moreover, the particle shape has an effect on the diffusion of H. The cubic particle exhibits the ability to absorb H atoms faster than the other two shapes. More specifically, our DMD model predicts that the formation and movement of stacking faults may slow down the propagation of the hydride phase boundary, and hence reduce the speed of H absorption. In this regard, the two-way interaction between H absorption and lattice deformation is remarkable.

5.2 Future work

In this dissertation, the developed DMD computational framework is only applied to simulate H mass transport in single-crystal Pd nanoparticles. Therefore, many new applications can be explored by the framework. For example, the arrangement of atoms in most crystalline solids is not perfect. It is highly desirable to extend the framework to investigation of the interaction between interstitial solute atoms and preexisting crystallographic defects, e.g., nanovoids, stacking faults and grain boundaries, during the long-term diffusion process.

The length scale of the simulation domain in DMD methods is typically on the order of nanometers. However, some phenomena of interest take place at macroscopic scale, such as solute-induced cracks, while the atomic resolution of some specific regions becomes signif-

icant, such as the tip of a crack. In other words, relatively small parts of the simulation domain require full atomic description, while the rest can be modeled using continuum mechanics. In this regard, one of the future work is to combine the DMD framework with a continuum model to form a quasicontinuum method for large-scale deformation-diffusion coupled problems.